Commissioning of New Trigger Readout System of Liquid Argon Calorimeter towards the LHC-ATLAS Run3 Experiment

(LHC-ATLAS Run3 実験に向けた液体アルゴンカロリメータの新型トリガー読み出しシステムのコミッショニング)

藏　嘉琦

Jiaqi Zang

Department of Physics
Graduate School of Science
The University of Tokyo

This dissertation is submitted for the degree of
Master of Science
January 2022

Acknowledgements

First and foremost, I would like to express my great gratitude to my advisor Prof. Junichi Tanaka, who provided me with such a chance to participate in the ATLAS experiment. Tanaka-sensei has helped me a lot since I came to Japan, teaching me many things about experiments, data analysis, and programming. He also supported me a lot in my research life and gave me much advice for writing the thesis. I am also grateful to Assistant Prof. Yuji Enari. He taught me a lot about the LAr calorimeter, especially about the new digit trigger readout electronics and the online software development. When I encountered difficulties in my research, he would actively provide me with constructive ideas and suggestions. He also gave me much valuable advice for this master's thesis.

Thanks to the experts in the LAr group at CERN. Project leader George Aad supervised and helped me with the qualification task. He also gave me many constructive suggestions on the connectivity scan and BCID calibration. Postdoctoral researcher Ellis Kay from the University of Victoria helped me develop the automation script for the SSW scan analysis. Postdoctoral researcher Konie Al Khoury from Columbia University helped with the validation of LTDBs.

In addition, I would like to acknowledge the senior students and my friends in Tanaka Lab: Gen Tateno, Reiyo Oishi, Tingyu Zhang, Ryunosuke Okubo, and Marin Furukawa. Tateno provided me with a lot of technical advice on programming. In addition, the video tutorials he made about the LAr calorimeter helped me deepen my understanding of the experiments to a great extent. Oishi taught me a lot about LATOME firmware development. Tingyu provided a lot of help and advice for my data analysis. Okubo has given me many interesting thoughts about his research on quantum computers. Furukawa added a lot of color to my daily life during this COVID-19 pandemic. Her positive attitude towards life and research is an inspiration to me.

I am also grateful to the other contemporary students for the discussions and presentations during the various seminars. I have benefited a lot from these experiences. And thanks to the University of Tokyo and ICEPP for providing such a profound academic atmosphere.

Thanks to my other friends who study at the University of Tokyo for their help and mental support in my daily life. Despite the coronavirus outbreak all over the world, I still have faith in an open and hopeful future.

At last, I would like to express my heartfelt gratitude to my family, who supported my research life in Japan.

Abstract

The world's highest energy proton-proton colliding accelerator, the Large Hadron Collider (LHC) experiment at CERN, was proposed and started in 2008 to extend the frontiers of particle physics. The ATLAS experiment at LHC is designed to record the particle collisions at the LHC and search for Higgs bosons and physics beyond the Standard Model. Due to the need to record a large amount of collision data, the trigger system is applied. The trigger system uses the information provided by the readout system for object recognition, such as position and energy. So that only the events that pass a set of criteria are selected. During the Run-2 period (the year 2015-2018), the LHC collided beams at center-of-mass energy $\sqrt{s} = 13$ TeV, and ATLAS recorded about 139 fb^{-1} of proton-proton collision data. Since Run-2 ended in 2018, the LHC has been upgraded and will start Run-3 in April 2022. In order to accommodate the update, the ATLAS trigger system requires higher efficiency and better resolution. Hence the phase-I upgrade for the ALTAS trigger system is performed.

The ATLAS Liquid Argon Calorimeter phase-I upgrade provides the new trigger system to obtain better energy resolution and efficiency for selecting electrons, photons, τ leptons, jets, and missing transverse energy. The new readout system applies over 34000 supercells with 10 times higher granularity than the old readout cells and uses optical fibers to transmit the digitized data from the front-end to the back-end. The supercells with multi-layer structure cover the region of $|\eta| < 4.9$. The signals read out from the supercells are digitized by the LTDB at the front-end and transmitted to the back-end via optical fibers, where they are calculated by the LATOME board equipped with a high-speed FPGA for energy and timing reconstruction. The computation result is then sent to FEX for object recognition through optical fibers.

In this thesis, several commissioning works to validate the new trigger system are presented. The first work is connectivity check. It's performed to check whether the supercells are connected correctly from the detector to the back-end. The SSW scan is used to check the mapping of all the 34048 supercells, and the corresponding analysis framework for the SSW scan is developed in this research. Also, by utilizing such an analysis tool, some other channel issues like bad links or bad ADC configuration are also investigated.

Besides checking the connectivity of supercells, the system latency of the new trigger system is also calibrated in the study. The system latency is required to be well-tuned and fixed for a stable system. The energy and timing computation values cannot be obtained correctly without the calibrated system latency. In the ATLAS experiment, the bunch crossing identification (BCID) is used for adjusting the system latency. Such work of adjusting the BCID of over 4000 fibers on the LATOME board is done by aligning the BCID of the new trigger system to the BCID of the reference main readout system. And the result of BCID calibration is given at last.

The research also utilizes the pilot run data taken in October 2021 to perform a full-powered new readout system test with real particles. In the pilot run, the detector managed to take both beam splash and collision data. With these data, the comparison of BCID and the reconstructed E_{T} between the two readouts is made, where E_{T} is computed by the optimal filtering algorithm with the calibrated optimal filtering coefficient. And through this comparison, the thesis gives the evaluation of the commissioning works and the conclusion on whether the new trigger system can achieve the expected performance.

Table of contents

List of figures

List of tables

Nomenclature

Acronyms / Abbreviations

ADC Analog-to-Digital Converter

AMC Advanced Mezzanine Card

ATCA Advanced Telecommunications Computing Architecture

ATLAS A Toroidal LHC Apparatus

BCID Bunch Crossing Identification

BSM Beyond Standard Model

c.m. center-of-mass

CERN European Organization for Nuclear Research

CST Cathode Strip Chamber

CTP Central Trigger Processor

EMB Electromagnetic Barrel

EMEC Electromagnetic Endcap

EM Electromagnetic

$E_{\mathrm{T}}^{\mathrm{miss}}$ Missing Transverse Momentum

FCal the Forward Calorimeter

FEB Front-End Board

FEC Front-End Crate

FEX Feature Extractor

HEC Hadronic End-cap Calorimeter

HFEC Half Front-End Crate

HLT High Level Trigger

ID Inner Detector

IP Interaction Point

IPMC Intelligent platform management controller

L1Calo Level-1 Calorimeter Trigger System

LArC LAr carrier

LAr Liquid Argon

LATOME LAr Trigger Processing Mezzanine

LB Luminosity Block

LDPB LAr Digital Processing Blade

LDPS LAr Digital Processing System

LHC Large Hadron Collider

LS2 the second LHC long Shutdown

LSB Layer Sum Board

LTDB LAr Trigger Digitizer Boards

MDT Monitored Drift Tube

MS Muon spectrometer

ROC Readout Crate

ROD Readout Driver

RPC Resistive Plate Chamber

RTM Rear Transition Module

SC Super Cell

SCT Semiconductor Tracker

SM Standard Model

SPAC Serial Protocol for Atlas Calorimeter

SSW Shaper Switch

SUSY Supersymmetry

TBB Tower Builder Boards

TBM Trigger Busy Module

TDAQ Trigger and Data Acquisition

TGC Thin Gap Chamber

TRT Transition Radiation Tracker

TTC Timing Trigger and Control

VME Versa Module Eurocard

Chapter 1

Introduction

1.1 Theoretical Background

1.1.1 The Standard Model

The Standard Model (SM) of elementary particles describes the fundamental constituents of matter and their interactions. As shown in Figure 1.1, there are six types of quarks and six different leptons which are classified into three generations. These particles are spin 1/2 fermions, and all have their own anti-particles. On the other hand, the four-vector bosons on the right side: photon, W/Z, gluon, are the propagator of interactions. And last, a special scalar Boson, Higgs Boson, which was discovered in 2012 by the ATLAS and CMS at LHC [1], makes the other particles massive. Generally, the Standard Model is based on the following symmetry group:

$$SU(3)_C \times SU(2)_L \times U(1)_Y. \tag{1.1}$$

Interactions can be derived from this. $SU(3)_C$ describes the strong interaction with charge *color* (C) and corresponds to the local symmetry whose gauging gives rise to quantum chromodynamics (QCD). The gauge symmetry $SU(2)_L \times U(1)_Y$ describes the electroweak interaction with the *weak isospin* (L represents for "left-handed") and the *hypercharge* (Y) as conserved current. The electroweak interaction is unified from the weak interaction (QCD) via the spontaneous symmetry breaking.

1.1.2 Beyond the Standard Model

Although the SM theory can successfully explain most of the phenomenon from many different experiments and describe the elementary particles with the Higgs mechanism, it's

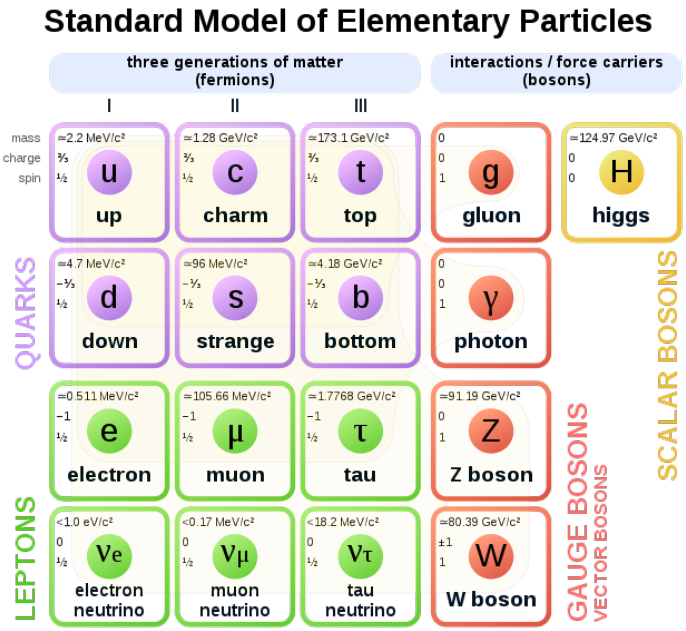

Fig. 1.1 Elementary Particles in SM. Fermions build the matter and Bosons propagate the interactions [2]

still not the ultimate theory for nature. For example, it cannot include the gravitational interaction with the other three fundamental interactions. Also, objects that cannot be observed directly through the SM interactions in our universe are much more than the ordinary objects, which can be described in the SM. This is called Dark Matter (DM). One of the observational evidence for DM is the Galaxy rotation curves. The relation between the rotation velocity and the distance from the center of the galaxy is different from what is expected from Kepler's Second Law with ordinary matters. Another important question is the hierarchy problem. SM cannot stabilize the hierarchy between the energy scale that characterizes the electroweak symmetry breaking, $M_{EW} \sim 100$ GeV, and the Planck scale (1.22×10^{19} GeV) against large radiative corrections without an unnatural fine-tuning of the parameters of the fundamental theory at the Planck scale.

Hence, Supersymmetry (SUSY) theory is raised as a candidate to explain these unsolved problems. It's a generalization of the space-time symmetry that transforms fermions into bosons and vice versa [3, 4]. The Large Hadron Collider (LHC) at CERN in Switzerland is then making efforts to find those SUSY particles.

1.2 Research Purpose

The LHC is built to extend the frontier of particle physics and explore the new physics beyond the SM. In which, the ATLAS (A Toroidal LHC Apparatus) experiment is the largest particle detector experiment to probe *p*-*p* and *A*-*A* collisions. The LHC complex will be upgraded by 2022. The second long shutdown after the 3-years-operation of Run-2 in 2018 and the upgrade for Run-3 is performed. The center-of-mass energy will also raise from $\sqrt{s} \simeq 13$ TeV to 13.6 TeV. In order to adapt to this upgrade, the so-called phase-I upgrade project for the ATLAS Liquid Argon (LAr) Calorimeter is performed, and a new trigger readout system is installed. The research focuses on the commissioning works on the new digital trigger readout, such as the front-end electronics validation, correction of mapping of the new readout path, and calibration works. With the calibrated new readout system, despite the increased beam energy, the trigger performance is more reliable than before and has better sensitivity for searching the interesting events. One important improvement for the system is the readout cell. The new readout cells with better granularity provide better energy resolution and shower shape information to the trigger system and therefore increase the S/N for the physical analysis.

1.3 Thesis Constitutes

This thesis introduces the LHC-ATLAS experiment in Chapter 2. Chapter 3 discusses LAr phase-I upgrade project through the introduction of legacy and new electronics. Chapter 4 presents the connectivity check of the new readout path and the validation of LTDBs (LAr Trigger Digitizer Boards), which are the on-detector electronics for the new trigger system. Chapter 4 also discusses the timing alignment between the digital trigger readout and the main readout in ATLAS. Chapter 5 shows calibration runs and the analysis for the recent LHC Pilot run in October 2021. And the last Chapter 6 concludes this thesis and gives an outlook for the near future, including fixing the remaining firmware problem and the adjustment for the digital trigger system.

Chapter 2

LHC-ATLAS Experiment

2.1 Large Hadron Collider

The LHC at the European Organization for Nuclear Research (CERN) is the largest particle collider with the highest energy in the world. It has a huge ring with a 27 km circumference that is about 100 meters underground. The view of the LHC is shown in Figure 2.1. The depth protects the detector from background noise such as cosmic rays. And the long length allows the proton to be accelerated to nearly the speed of light under the 8.3 Tesla magnetic field. The two proton beams are contained in separate pipes throughout most of the circumference and are brought together into a single pipe at the interaction points (IP). A large number of protons in a bunch leads to about 30 or more head-on collisions every 25 ns.

When the two bunches which containing n_1 and n_2 particles collide head-on with the average collision frequency f_{coll}, the instantaneous luminosity $\mathcal{L}$ is calculated by the following formula [5, 6]:

$$\mathcal{L} = f_{coll} \frac{n_1 n_2}{4\pi \sigma_x^* \sigma_y^*} \mathcal{F}, \tag{2.1}$$

where σ_x^* and σ_y^* characterize the RMS transverse beam sizes in the horizontal and vertical directions at the IP, and $\mathcal{F}$ is a factor of order one that is affected by the geometric effects. The f_{coll} value equals the number of bunches per beam times the revolution frequency for the circular collider. Thus, the number of events N_{exp} for an interesting process is the product of the cross-section of the interest σ_{exp} and the time integral over the instantaneous luminosity:

$$N_{exp} = \sigma_{exp} \times \int \mathcal{L}(t) dt. \tag{2.2}$$

The primary goal of the LHC is to search for the Higgs boson (done in 2012) and new physics beyond the SM. The energy collision at 7 TeV was achieved in March 2010, and the first collision at 8 TeV was achieved in April 2012. After the first shut down, the LHC is upgraded, and the energy is raised to 13 TeV. And then, it started the second run (Run-2) from 2015 to 2018 with the much higher c.m. energy. After Run-2 is finished, the LS2 is performed and started the three-year upgrade. This upgrade equips the LHC with better-protected magnets, more sensitive detectors, and other improvements. For the schedule, the machine will start running experiments again in April 2022.

In Run-2 [7], the LHC successfully collected the collision data with a total integrated luminosity of 139 fb^{-1} for physics analysis. After the 3-years LS2 upgrade, the peak instantaneous luminosity is expected to be the value of 3×10^{34} $\text{cm}^{-2}\text{s}^{-1}$, and the c.m. energy will be raised from $\sqrt{s} = 13$ TeV to 13.6 TeV. Under such a high luminosity environment, several proton-proton interactions per bunch crossing occur. About 23 interactions are typically expected in case of the luminosity of 10^{34} $\text{cm}^{-2}\text{s}^{-1}$. It's rare for more than one of these interactions to be a "hard scatter" for the target physics, for example, Higgs boson production. Most of the other interactions are so-called multi-jet productions with low p_{T} (e.g., gluon gluon $\rightarrow$ gluon gluon). This is referred to as "pile-up".

2.2 ATLAS Experiment

"**A** **T**oroidal **L**HC **A**pparatus**S**" (ALTAS) is one of the detector for the LHC at CERN. It investigates a wide range of physics, from the search for new physics beyond the SM to the precision measurements of SM parameters, including the Higgs boson. The ATLAS detector has a forward-backward symmetry around the interaction point with a diameter of 25 m, a length of 44 m, and a weight of 7000 tons. It consists of an inner detector (ID), an electromagnetic and a hadronic calorimeter, and a muon spectrometer (MS). The schematic view of the ATLAS detector is shown in Figure 2.2. The nominal interaction point defines the origin of the coordinate system. The beam direction defines the z-axis, the positive x-axis goes from the interaction point to the center of the LHC, and the positive y-axis points towards the surface. Therefore the x-y plane is transverse to the beam direction. Additionally, on this plane, the coordinates (r, ϕ) are used, where r is the radial distance from the interaction point and ϕ is the azimuthal angle around the beam axis. Figure 2.3 shows the illustration of the coordinate system. Generally, the positive direction of the z-axis is A-side, and the negative direction is called C-side.

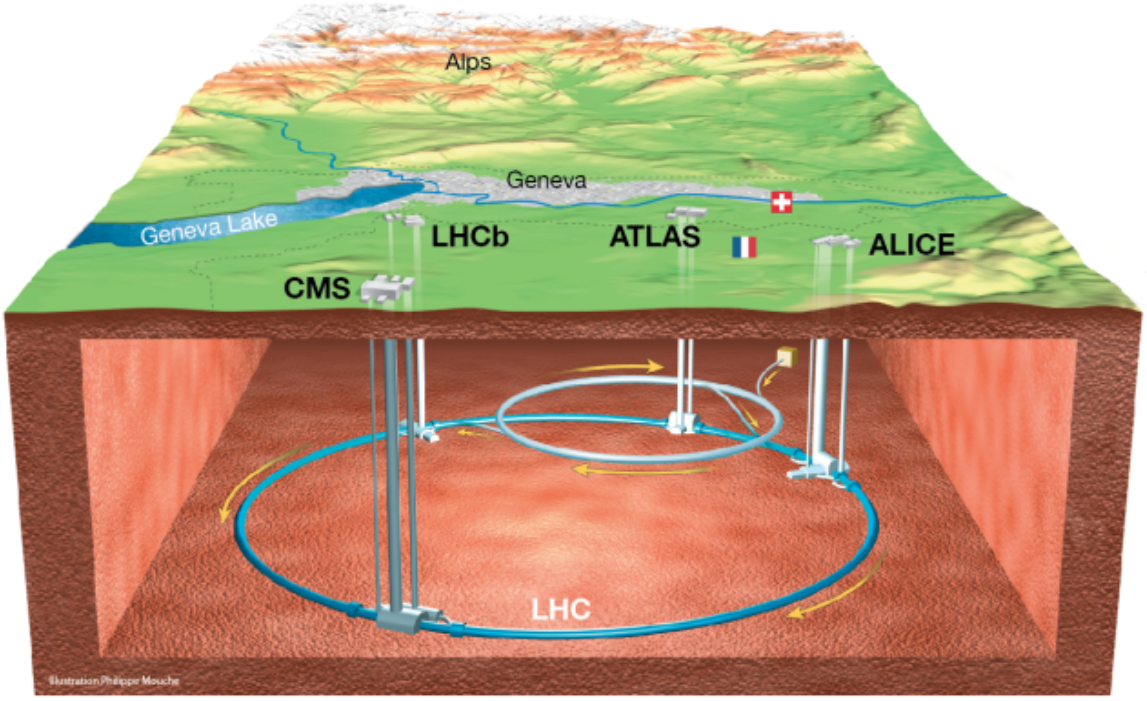

Fig. 2.1 Overall view of the LHC. There are four main detectors: ATLAS, CMS, ALICE and LHCb [6].

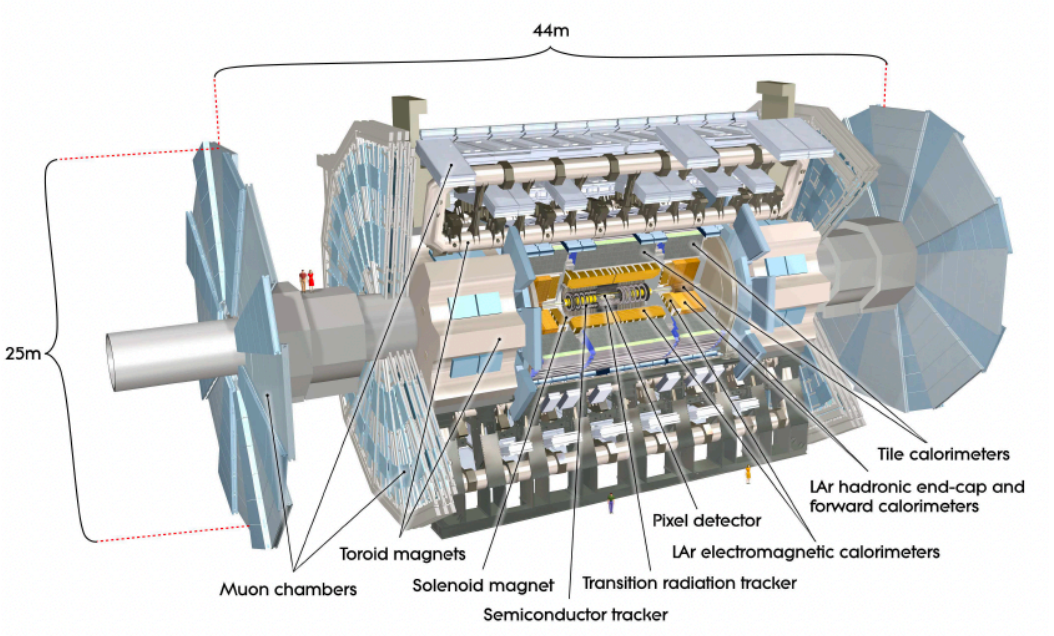

Fig. 2.2 Schematic view of the ATLAS experiment and its main components [8]

The pseudorapidity η for particles coming from the primary vertex is defined as:

$$\eta = -\ln(\tan(\frac{\theta}{2})). \tag{2.3}$$

where θ is the polar angle. Therefore η is 0 for the x-y plane vertex and infinite for the beam direction. Figure 2.4 shows how it is changed by θ. And this is the approximation of the rapidity y in the limit of ultrarelativistic particles (which set the invariant mass to 0):

$$y = \frac{1}{2}\ln(\frac{E+p_z}{E-p_z}), \tag{2.4}$$

where p_z is the projection of the particle momentum along the z-axis. Differences in rapidity are invariant under Lorentz transformations and the density of emitted particles $\frac{dN}{dy}$ as a function of the rapidity is almost constant.

To help the reconstruction of the collision events, quantities such as transverse momentum $p_T = p\sin\theta$ and transverse energy $E_T = E\sin\theta$ is defined. Also, to measure the angular distance of two objects, a quantity ΔR is defined in the transverse plane:

$$\Delta R = \sqrt{(\Delta\eta)^2 + (\Delta\phi)^2}. \tag{2.5}$$

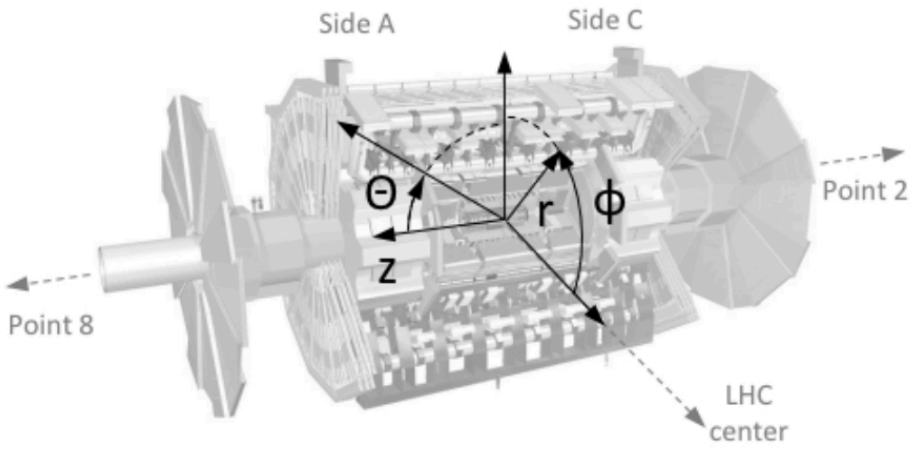

Fig. 2.3 The ATLAS coordinate system [9].

2.2.1 Inner Detector

The Inner Detector is designed for tracking the primary and secondary vertex, which is above a given p_T threshold within the pseudorapidity $|\eta| < 2.5$. Also it provides the electron identification over $|\eta| < 2.0$. Thus the high luminosity demands the ID to have fine granularity. To meet such requirement, materials used for ID is quite limited because of the issue of multiple scattering.

The ID is immersed in a 2 T magnetic field generated by the central solenoid and contained in the cylindrical envelope of length 3.5 m and diameter 1.15 m. Three sub-detectors are utilized to meet the physics requirement. Figure 2.5 shows the alignment of those sub-detectors. The innermost component is the Pixel Detector, followed by the SemiConductor Tracker (SCT) and the Transition Radiation Tracker (TRT). The Pixel and SCT cover the region $|\eta| < 2.5$, while the TRT takes the responsibility of the track reconstruction up to $|\eta| = 2.0$.

Pixel detector The pixel detector provides the charged particle track recognition within the range of $|\eta|$ <2.5. It is not only responsible for the track reconstruction and vertices identification but also measures the track impact parameter, which is defined as the minimum distance between the track and the primary vertex.

SemiConductor Tracker Four layers of silicon microstrip detectors are placed in concentric cylinders around the beam axis. The end-cap modules are arranged onto nine wheels, each of which has up to three rings of modules.

Transition Radiation Tracker The TRT system is a straw tracker which provides useful information for electron identification by means of measuring the transition radiation [11]. Each straw tube has a diameter of 4 mm and was filled with a gas mixture of 70% Ar, 27%

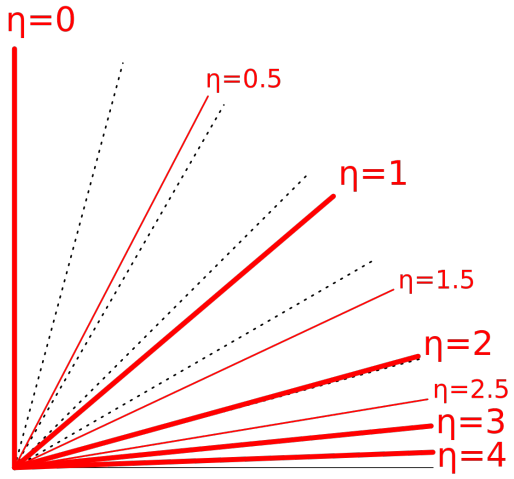

Fig. 2.4 Pseudorapidity η

CO_2 and 3% O_2 in Run-2 [12]. The passing charged particles will give rise to the ionization inside the straws, and the resulting free electrons migrate towards a gold-tungsten wire of 31 μm in diameter placed at the center of the tube at the voltage of -1.5 kV.

2.2.2 Calorimeter

The sampling calorimeters are adopted with full ϕ-symmetry at the ALTAS experiment. Figure 2.6 shows the overview of the calorimeters. The electromagnetic (EM) is mainly for electron and photon detection, and the hadronic calorimeter is for hardon detection. These calorimeters cover the range $|\eta| < 4.9$. The fine granularity of these calorimeters satisfies the physics requirements for jet reconstruction and $E_{\mathrm{T}}^{\mathrm{miss}}$ measurements.

LAr electromagnetic calorimeter

The EM calorimeter is designed to trigger on and provide precise measurement of electrons, photons, jets, and missing transverse energy $E_{\mathrm{T}}^{\mathrm{miss}}$. It uses liquid argon as active material and 1.8 mm lead plates as the absorber. The liquid argon has been chosen for its intrinsic linear behavior, its response stability, and radiation resistance. The lead absorber induces the EM shower when an electron or a photon goes through the detector. The shower and the ionized particles are therefore measured and used for calculating the energy of the incident particle.

The calorimeter consists of a barrel and two end-caps components, each housed in its own cryostat. The barrel region cover the range of $0 < |\eta| < 1.475$, and the end-cap region covers

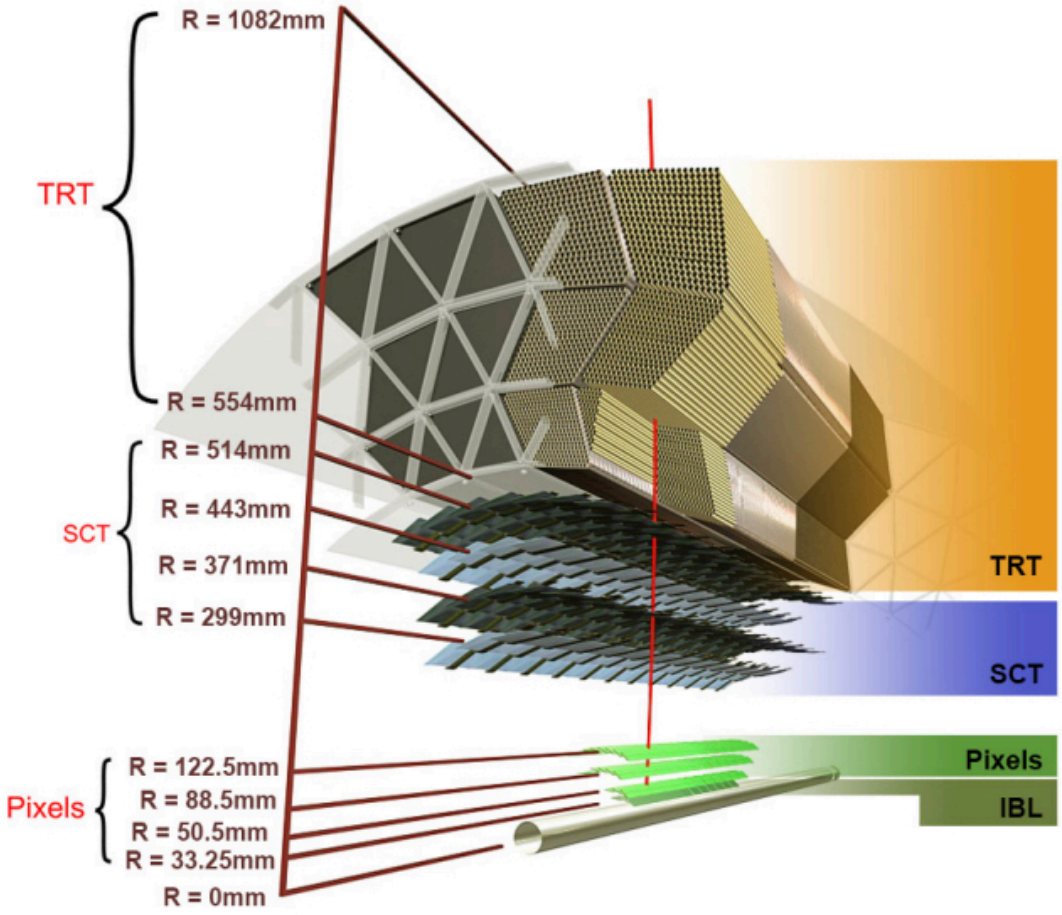

Fig. 2.5 3D vision of the barrel of the Inner Detector [10].

the range of $1.375 < |\eta| < 3.2$. The LAr calorimeter has a four-layer structure (called layer 0, 1, 2, 3), and an accordion geometry is chosen for the absorbers and the electrodes of the calorimeter. Figure 2.7 shows the three-layer structure (only layer 1, 2, 3) and the accordion structure with the example of the trigger tower. The front layer (layer 1) is finely segmented in η to measure the start point of the shower. The middle layer (layer 2) collects the largest fraction of the shower energy, and the back layer (layer 3) estimates the amount of energy leaking beyond the middle layer. Additionally, the presampler (layer 0) is implemented in the range of $0 < |\eta| < 1.8$ to provide a measurement of the energy lost in front of the EM calorimeters. The resolution of the EM calorimeter can be parameterized with the following expression [14]:

$$\frac{\sigma(E)}{E} = \frac{a}{\sqrt{E(GeV)}} \oplus \frac{b}{E(GeV)} \oplus c \tag{2.6}$$

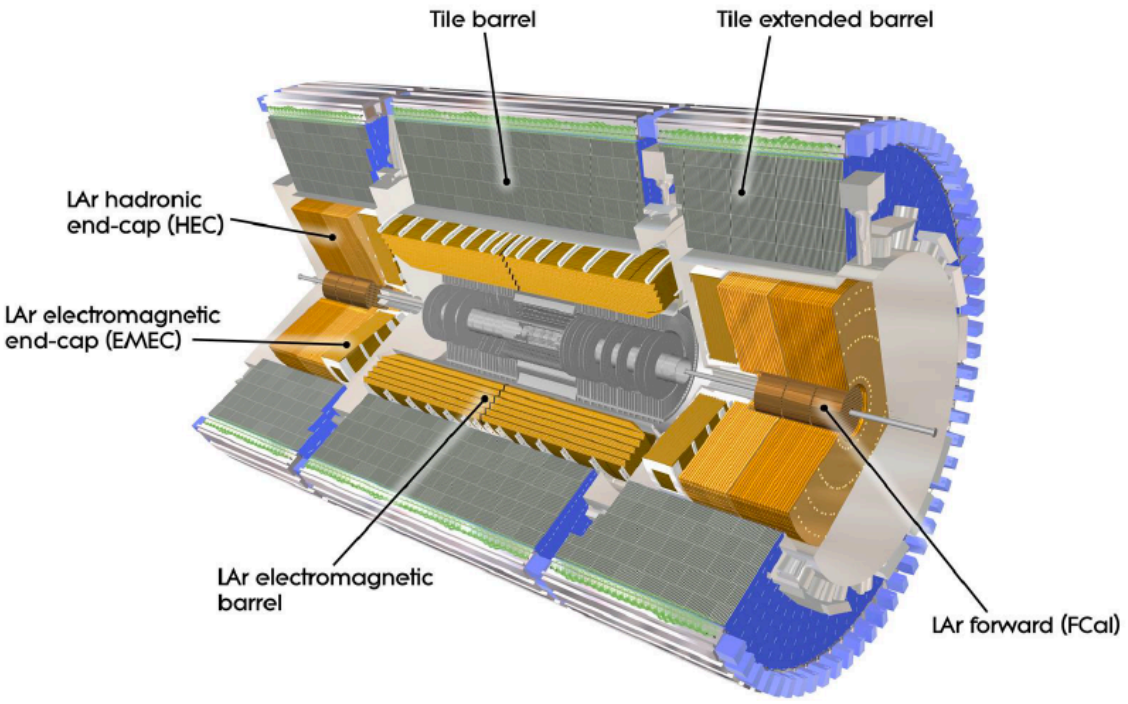

Fig. 2.6 Cut-away view of the calorimeter [13].

where a takes account the stochastic behaviour of the shower development, b accounts for the electronic and pile-up noise, and c is a constant that quantifies the non-uniform response of the calorimeter, the aging, and the radiation damage. The pile-up noise means energy deposits by the pile-up events (low p_{T} multi-jet productions).The intrinsic sampling term a is typically 10-11% $\sqrt{\mathrm{GeV}}$, the noise term b is expected to be 30 MeV-3 GeV in Run-3 pile-up conditions, and the constant term c is 1-2%.

Hadronic Calorimeter

The hadronic calorimeter consists of the tile calorimeter, the LAr hadronic end-cap calorimeter (HEC), and the LAr forward calorimeter (FCal) [8].

Tile Calorimeter The Tile calorimeter is responsible for the energy reconstruction of the jets and measurement of $E_{\mathrm{T}}^{\mathrm{miss}}$. It covers the range of $|\eta| < 1.7$. The central barrel locates in the region of $0 < |\eta| < 1.0$, and the two extended barrels are in the region of $1 < |\eta| < 1.7$. Special modules made of steel scintillator sandwiches fill the transition region. Figure 2.8 shows the schematic of the module. Each barrel consists of 64 such modules. The steel grid forms the 1.5mm module to module gap at inner radius and provides the volume for readout electronic, as well as the flux return for the solenoid field.

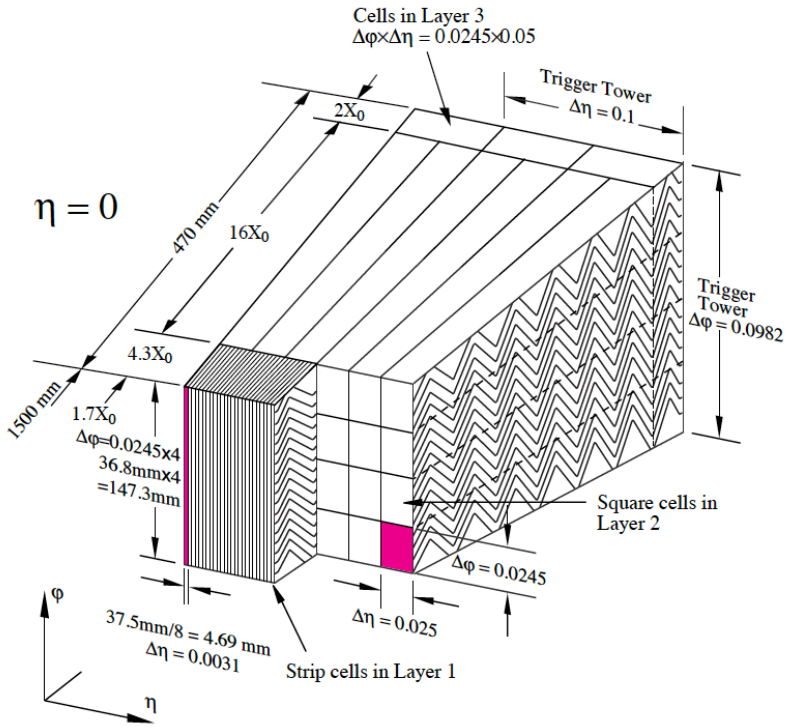

Fig. 2.7 Accordion structure of the calorimeters. Figure also shows the granularity of different types of layer.

Hadronic End-cap Calorimeter HEC is a LAr sampling calorimeter with flat-plate designed copper as the absorber, integrated with the end-cap cryostat and covering the range of $1.5 < |\eta| < 3.2$. It consists of a front wheel (HEC1) and a rear wheel (HEC2), and each wheel is constructed of 32 identical wedge-shaped modules. Figure 2.9 shows the schematic view of an HEC module. The front wheel consists of 24 copper plates, and meanwhile, the rear wheel has 16 copper plates.

Forward Calorimeter FCal is also integrated into the end-cap cryostat and cover the region $3.2 < |\eta| < 4.9$. Therefore, the FCal is exposed to high fluxes. It is designed with LAr gaps to avoid ion build-up problems and provide the highest possible density. FCal provides a good measurement of the forward jet and helps in reducing the background level in the muon spectrometer. Three modules are performed in FCal. One EM module (FCal1) with copper absorber to optimize the resolution and the heat removal, and the other two hadronic modules (FCal2, FCal3) with tungsten absorber to provide containment and minimize the spread of hadronic showers. Figure 2.10 shows the location of the modules.

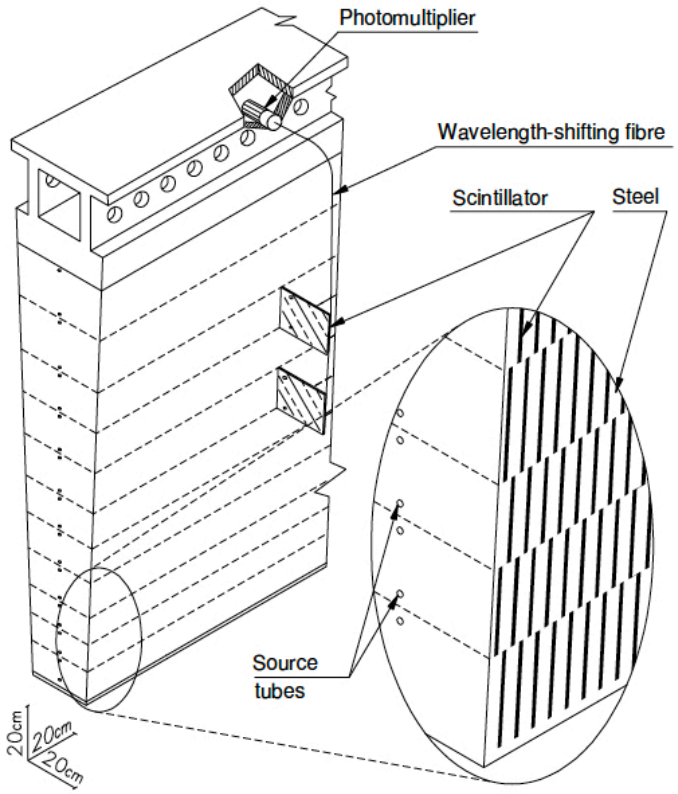

Fig. 2.8 Geometry of the tile calorimeter module [8].

2.2.3 Muon Spectrometer

The Muon Spectrometer (MS) is designed to provide standalone precise measurements of muons up to 3 TeV and in the range of $|\eta| < 2.7$ [15]. It forms the outer part of the ATLAS detector. The capability of reconstructing high-p_T up without ID provides the fast muon triggering in the region $|\eta| < 2.4$.

The layout of the spectrometer, as shown in Figure 2.11, is based on the magnetic deflection of muon tracks inside the detector. Monitored Drift Tube chambers (MDT) and Cathode-Strip Chamber (CSC) provide the precise measurement of the momentum of muon track. The trigger system consists of Resistive Plate Chambers (RPC) and Thin Gap Chambers (TGC) and covers the range $|\eta| < 2.4$. The trigger system serves to provide bunch-crossing identification (BCID) with efficiency larger than 99%, well-defined p_{T} thresholds, and measurement of the unbending direction of the track.

Monitored Drift Tube The barrel MDTs cover the region $|\eta| < 1.05$, as well as end-cap MDTs cover the range of $1.05 < |\eta| < 2.7$. Their size increases with the distance from the

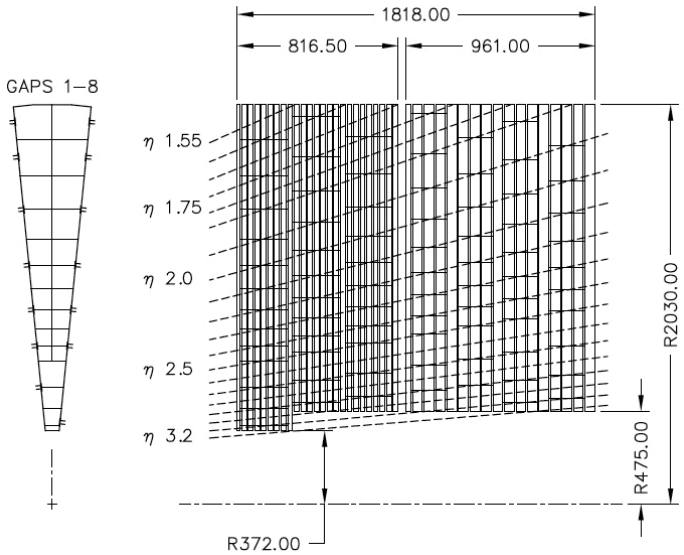

Fig. 2.9 Schematic $R-\phi$ (left) and $R-z$ (right) views of HEC. Dimensions are in mm [8].

interaction point. They are made of 3 to 8 layers of drift tube filled with a mixture of 93% Ar and 7% CO_2. The average resolution for a single tube is 80 μm and for a chamber is 35 μm.

Cathode Strip Chamber The CSC is responsible for the region $2.0 < |\eta| < 2.7$ to improve the resolution under the high hit rate near the interaction point. Similar to end-cap MDT, CSC consists of 8 large sectors and 8 small sectors. Trigger time for CSC is less than 30 ns, and resolution is about 60 μm.

Resistive Plate Chamber The RPCs are the trigger chamber which covers the barrel ($|\eta| < 1.05$) region. They are made of parallel resistive plates and a gas-filled gap of 2 μm. The time resolution for RPC is about 1.5 ns, and position resolution is about 10mm.

Thin Gap Chamber The TGCs are responsible for the end-cap region ($1.05 < |\eta| < 2.4$). Time resolution for TGC is about 4 ns, and position resolution is 2-6 mm.

2.2.4 Data Acquisition and Trigger System

The ATLAS system provides 1.7 billion pp collisions per second for a combined data volume of 60 million MB per second. Bunches of protons cross 40 million per second (40 MHz), and each bunch contains 10^{11} protons. At a design beam luminosity of 10^{34} cm^{-2} s^{-1}, there is about 20 collisions per bunch crossing. Therefore only interesting events will be selected by a complex trigger system. The system consists of the Level-1 (L1) trigger and the High Level Trigger (HLT) to reduce the data flow from 40 MHz to about 1 kHz. When the bunches

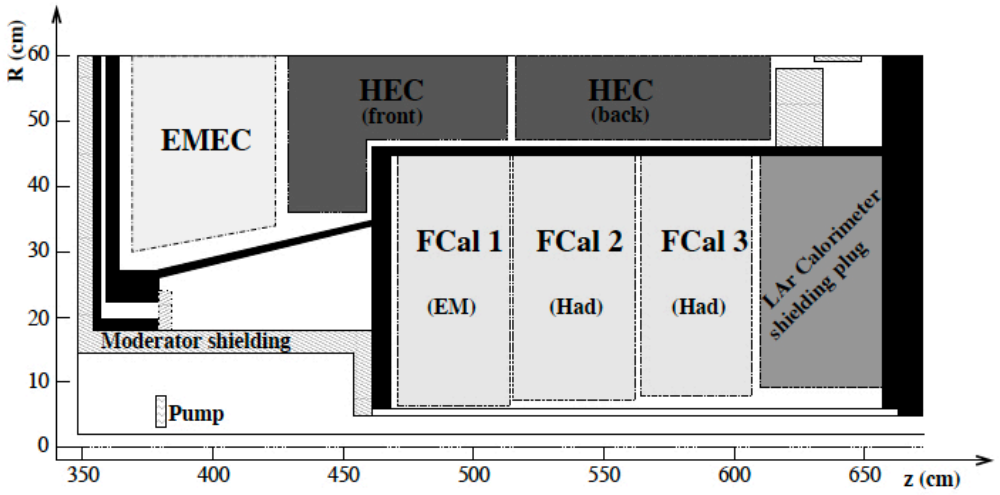

Fig. 2.10 The figure show the three FCal modules location in the end-cap cryostat [8].

collide, such a collision produces an "event", and the raw data recorded per event after the HLT is 1.6 MB, while the physics data is recorded with the 0.1 MB per event [16].

Level-1 trigger

The L1 trigger uses reduced-granularity information from MS and the calorimeters. It can accept a maximum incoming event rate of 40 MHz and uses hardware processors to unambiguously identify the bunch crossing of interesting events in 2.5 μs since the collision occurs. The geometrical location of the trigger objects will then be sent to the next level trigger with the form of Regions-of-Interest (ROI) at the event rate of 100 kHz. Figure 2.12 shows the workflow of the L1Calo system in Run-3.

High Level Trigger

The HLT is performed by the event filter. It mainly depends on the commercially available computers and networking hardware. It can handle a maximum rate of 75 to 100 kHz using the full granularity of the ROI provided by the L1 trigger.

2.3 The LHC Upgrade Project

The phase-I upgrade project, which started after Run 2 ended in 2018, aims to cope with the increase of luminosity in Run 3 and high-luminosity LHC. The new small wheel (NSW)

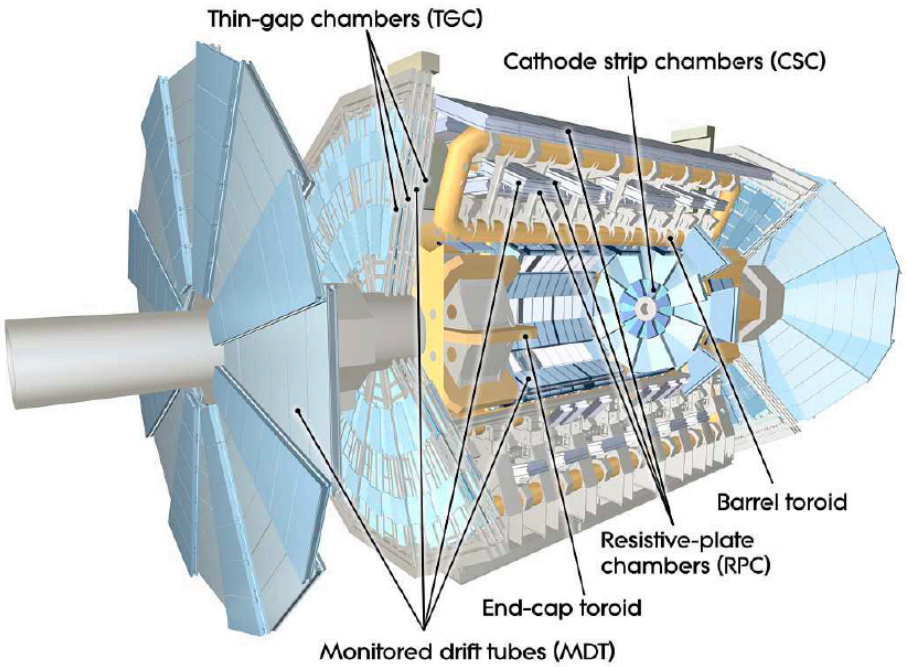

Fig. 2.11 Cut-away view of Muon Spectrometer [8].

is installed to provide much more stringent selection criteria for muons and to handle high background and pile-up rates. Meanwhile, for the trigger, the calorimeter introduces the new readout system to increase the granularity of the readout cells and increase the sensitivity to increase the ratio of S/N. Therefore, the performance of the L1 trigger system is significantly improved after the phase-I upgrade. However, due to the coronavirus pandemic starting at the end of 2019, the phase-I upgrade spent one more year than expected. After the upgrade from 2019 to 2021, Run-3 will operate for three years and then start the phase-II upgrade project. During the phase-II upgrade, the LHC will upgrade to the so-called High-Luminosity LHC, and the luminosity will be increased up to 5×10^{34} cm^{-2}s^{-1}. Many systems in the ALTAS detector will be modified to meet the challenge of the upgrade. For example, the inner detector will be rebuilt, and the muon detector will be modified. Both muon trigger and electron trigger at the L1 trigger will have fast-tracking information matching tracks to regions of interest.

The new data acquisition system after the phase-I upgrade is shown in Figure 2.13. The data from the ATLAS detector are first buffered in the Readout Drivers (ROD) and waiting for judgment from the L1 trigger. The event rate is therefore reduced from 40 MHz to 100 kHz. The events accepted by the L1 trigger are then buffered in the Readout System (ROS) and waiting for the signal from HLT. With the acceptance of the HLT, the data will be stored

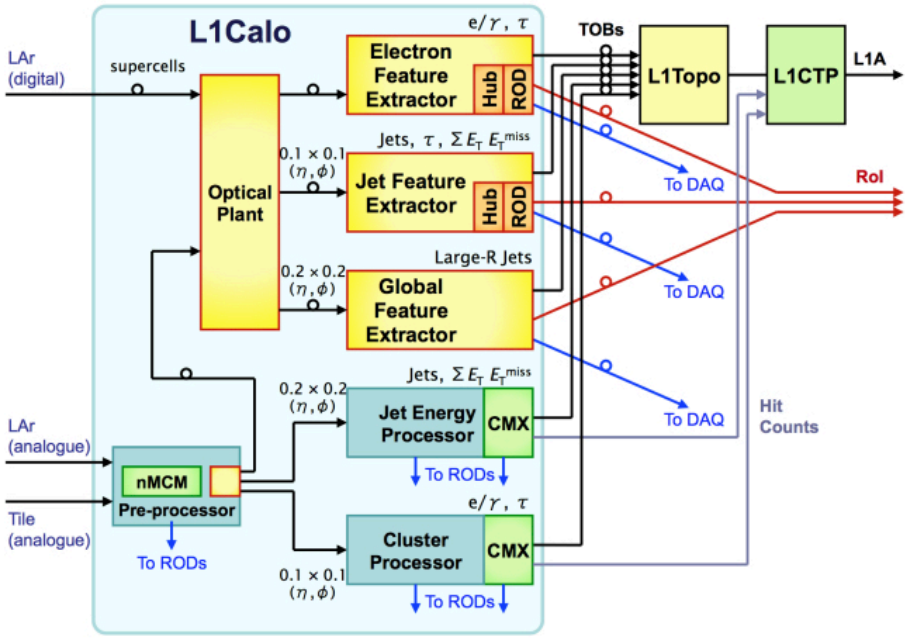

Fig. 2.12 Workflow of the L1Calo system in Run-3. Different colors of paths indicate the different data output [17].

in the permanent storage disk for the physics analysis and exported to the Tier-0 facility at CERN's computing center. At last, the schedule of the LHC upgrade and run plan is shown in Figure 2.14.

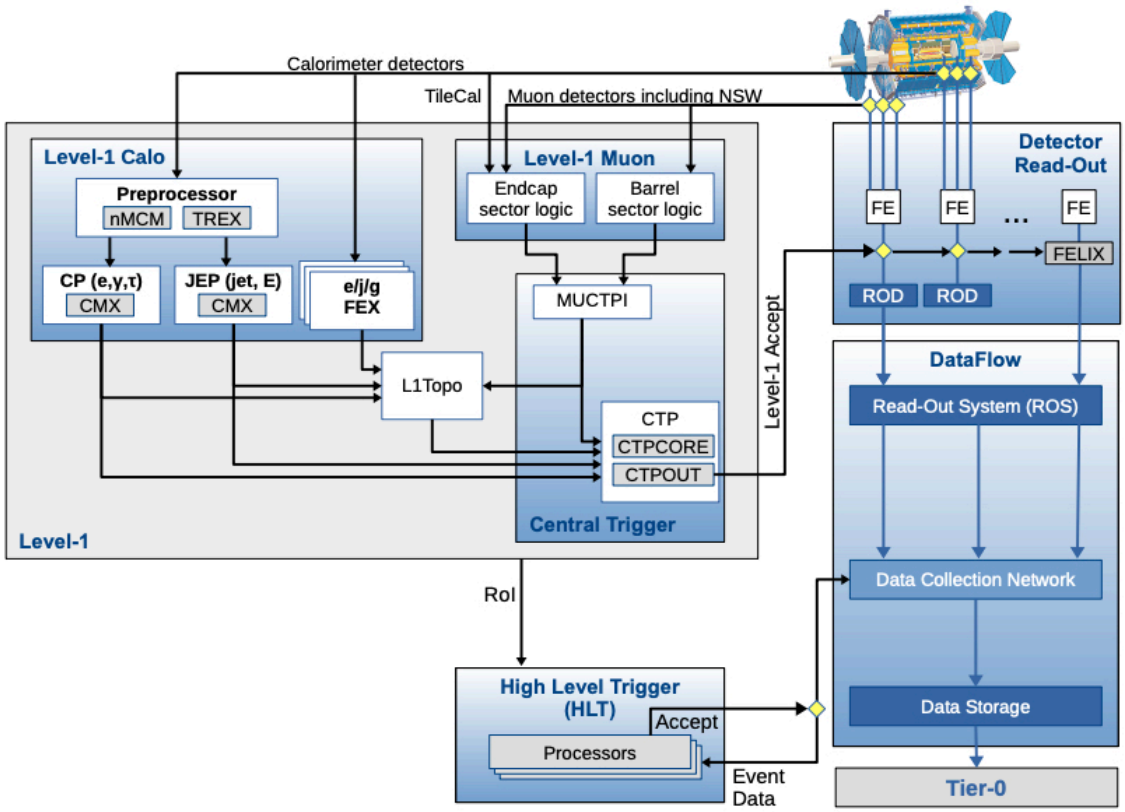

Fig. 2.13 Work flow of the ALTAS DAQ and trigger system after the phase-I upgrade [18]

Fig. 2.14 Schedule for the LHC upgrade plan [19].

Chapter 3

LAr Phase-I Upgrade Project

The Liquid Argon (LAr) phase-I upgrade project is to install the new trigger readout electronics during the LS2 of the LHC from 2018 to 2021. The new readout and trigger system aims to provide better energy resolution and shower shape information to the Level-1 trigger system, which is introduced in Section 2.2.4. The better trigger performance will enhance the discrimination against background events, for example, high p_{T} multi-jet productions where jets are misidentified as electrons or photons. As a result, this kind of improvement will increase the S/N ratio and help the analysis for the newly discovered Higgs boson and the discovery of new particles, which indicate the physics beyond the Standard Model.

3.1 Signal Detection

The EM calorimeters consist of the accordion-shaped copper-kapton electrodes positioned between lead absorber plates and kept in position by honeycomb spacers while the system is immersed in LAr. Figure 3.1 gives an example of EMB (EM barrel). The accordion geometry is to provide the full coverage of the absorbers and active the material in the path of particles. As long as the energy of the coming photons and electrons meet the threshold, the particles will be absorbed by the lead layer and give rise to the Bremsstrahlung radiation and the pair production. This process is repeated until the energy is not enough to do so. Figure 3.2 gives a view of the tracks from the interaction point to the outward Muon Spectrometer, where electrons and photons are stopped at the EM calorimeters. The electrons and positrons produced by the EM shower ionize the LAr, and the electrons will be attracted to the readout electrodes by the electric field provided by about 2 kV HV.

The drift time of the electrons depends on the LAr gap width and the drift velocity, and the number of electrons determines the amplitude of the signal. Therefore, the drifted electrons form the triangular pulse, which is shown in Figure 3.3. After that, the signals are

then converted to the bipolar-shaped pulse obtained by the CR-$(RC)^2$ circuit and sampled at the LHC bunch crossing frequency of 40 MHz. The integration of the bipolar pulse is 0, and the amplitude is proportional to the triangular one. With these properties, the energy of the particle can be therefore calculated with the optimal filtering algorithm (see Chapter 5), and due to the properties of the waveform, noise can be canceled to some extent.

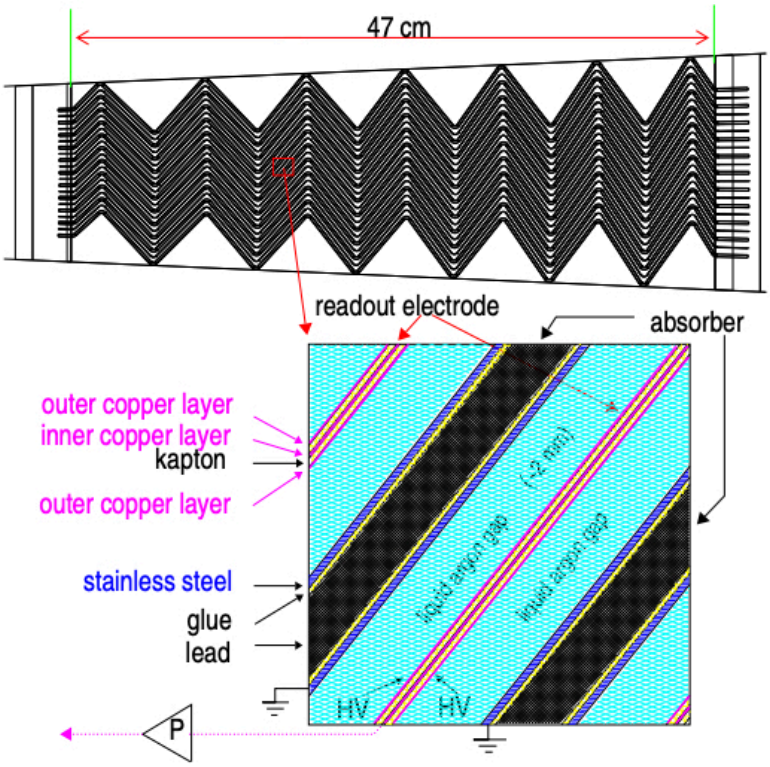

Fig. 3.1 Accordion structure of the barrel region [20]. The top figure shows the transverse view of the LHC beams. Particles are from left to right.

3.2 New Readout and Trigger System

The LAr readout system consists of front-end electronics (on-detector) and back-end electronics (off-detector). Front-end electronics are mounted directly on the LAr cryostats, and back-end electronics are wired in the USA-15 counting room.

3.2.1 Super Cell

Over 182000 calorimeter cells are equipped as the readout electronics to record energies in a range from 50 MeV to 3 TeV with the energy resolution expressed in Eq. 2.6. These

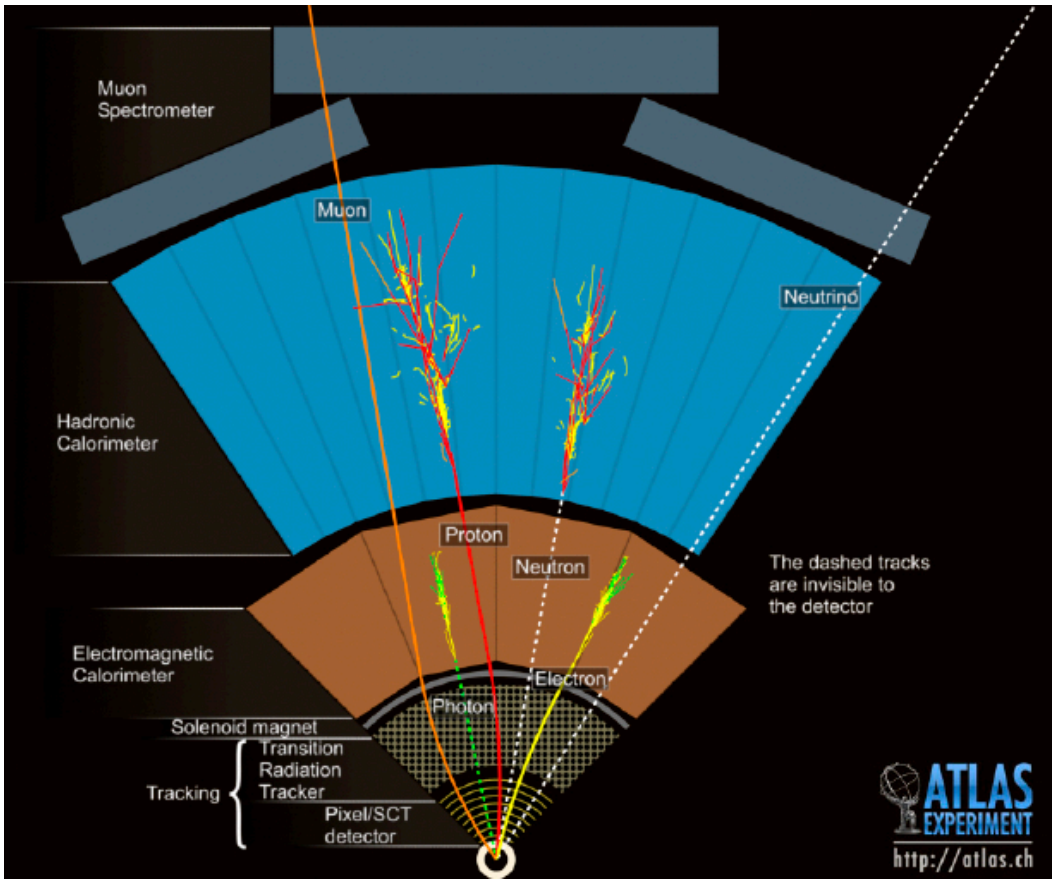

Fig. 3.2 Schematic diagram of the tracks from the splashing particles in ATLAS [21].

elementary cells are also called LAr cells. In Run-1 and Run-2, the energy deposited in the LAr cells is summed in an area of $\Delta\eta \times \Delta\phi = 0.1 \times 0.1$ as the calorimeter trigger information, which is called "Trigger Tower." In order to improve the energy resolution, a new scheme called "Super Cell (SC)" with 10 times finer granularity is introduced in the phase-I upgrade. Figure 3.4 compares the energy deposit of an electron in the legacy "Trigger Tower" and the new readout system with "Supercell", and their granularity in the EMB calorimeter are summarized in Table 3.1.

3.2.2 Front-End Electronics

The readout electronics are shown in Figure 3.5. The front-end system consists of 58 front-end crates (FECs), each hosting two baseplanes that house the following boards.

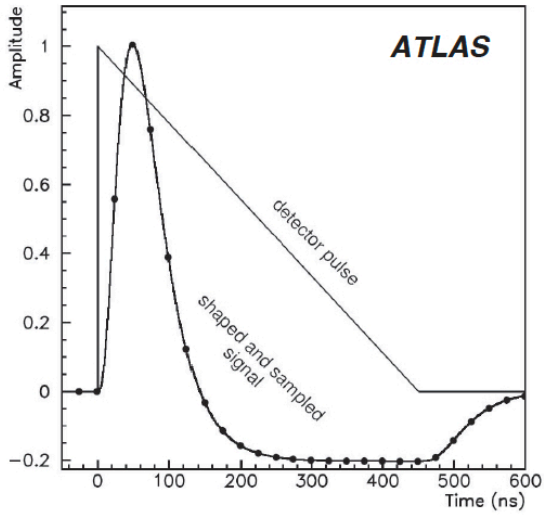

Fig. 3.3 The triangular pulse from the LAr calorimeter, overlaid with the bipolar-shaped and sampled pulse [22].

Table 3.1 Granularity of the trigger tower and super cell in the EMB calorimeter. n_η and n_ϕ indicate the number of grouped LAr cells in η and ϕ direction, respectively [22].

	layer	Elementary Cell	trigger tower		Super Cell	
		$\Delta\eta \times \Delta\phi$	$n_\eta \times n_\phi$	$\Delta\eta \times \Delta\phi$	$n_\eta \times n_\phi$	$\Delta\eta \times \Delta\phi$
0	presampler	0.025×0.1	4×1	0.1×0.1	4×1	0.1×0.1
1	front	0.003125×0.1	32×1		8×1	0.025×0.1
2	middle	0.025×0.025	4×4		1×4	0.025×0.1
3	back	0.05×0.025	2×4		2×4	0.1×0.1

Legacy electronics

Front-End Boards (FEB) Each FEB is a large 10-layer printed PCB that processes the signals from 128 channels in a specific layer of the calorimeter. They amplify, shape, sample, and digitize the ionization signals and transmit them to the back-end processors. The digitization is done by the Analog-to-Digital Converters (ADC) hosted on the FEB. The linear mixers and the Layer Sum Boards (LSB) generate the analog sum signals, which are utilized by the L1 trigger system.

Tower Builder Boards (TBB) TBBs form the legacy trigger tower signals from the summed analog signal provided by the LSBs. The trigger tower signals are then transmitted to the L1 trigger system via analog cables. In the HEC and FCal, Tower Driver Boards are used instead of the TBBs.

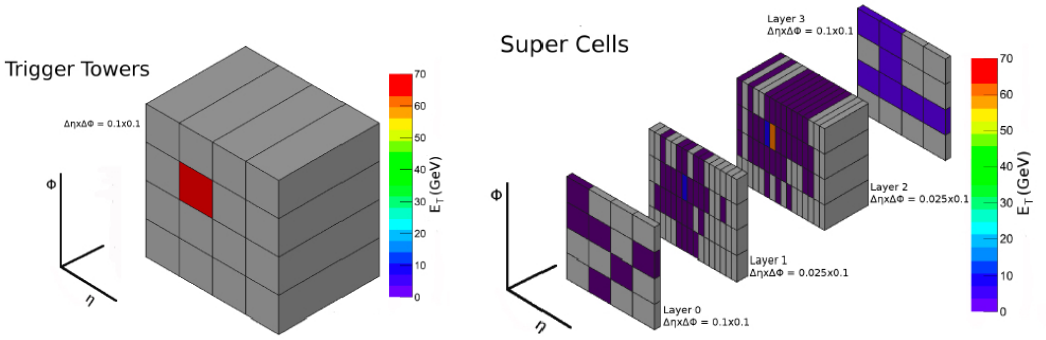

(a) Trigger Towers (b) Super Cell

Fig. 3.4 Schematic view of legacy and new readout cells in case an electron with 70 GeV E_{T} is injected. Figures show how the electron is seen by the 16 trigger towers (a) and by the 160 super cells (b) [22].

Calibration Boards The calibration boards are an essential part of the commissioning work during LS2. They control the injecting calibration pulse, which is generated by the onboard circuit. The calibration pulse is fine-tuned to be close to the bipolar pulse generated by the LAr ionization signal. However, the calibration pulse is still slightly different from the physical pulse. Therefore it's critical to treat the energy calculation carefully with the two different kinds of signals.

Controller Boards The controller boards receive the configuration and monitoring commands from the SPAC (Serial Protocol for Atlas Calorimeter) masters and the TTC (Timing, Triggering and Control: timing and control for all the ATLAS detectors) system and distribute the commands to all the other legacy boards in the FEC.

New electronics

Baseplanes Each FEC is divided into two halves with a baseplane installed in each half, which is shown in Figure 3.6. The new EMB baseplane has the same slots as the original baseplane. Space for the new LTDBs comes from the unallocated slot at one end of the FEC. The EMEC crates house two kinds of baseplane. The EMEC standard crate is similar to the EMB, and the EMEC special crate has one baseplane for EMEC and another for the HEC to free the tight slots of the HEC baseplane. The FCal baseplane has two LTDBs for each. In total, 124 LTDBs are installed on the 114 new baseplane.

Layer Sum Boards The LSB is a plug-in card for the FEB that performs the second level of summing of the analog signals, while the first level is done by the linear mixer. The new LSBs change their outputs and provide the signals for supercells in the front and middle layers and the legacy trigger tower.

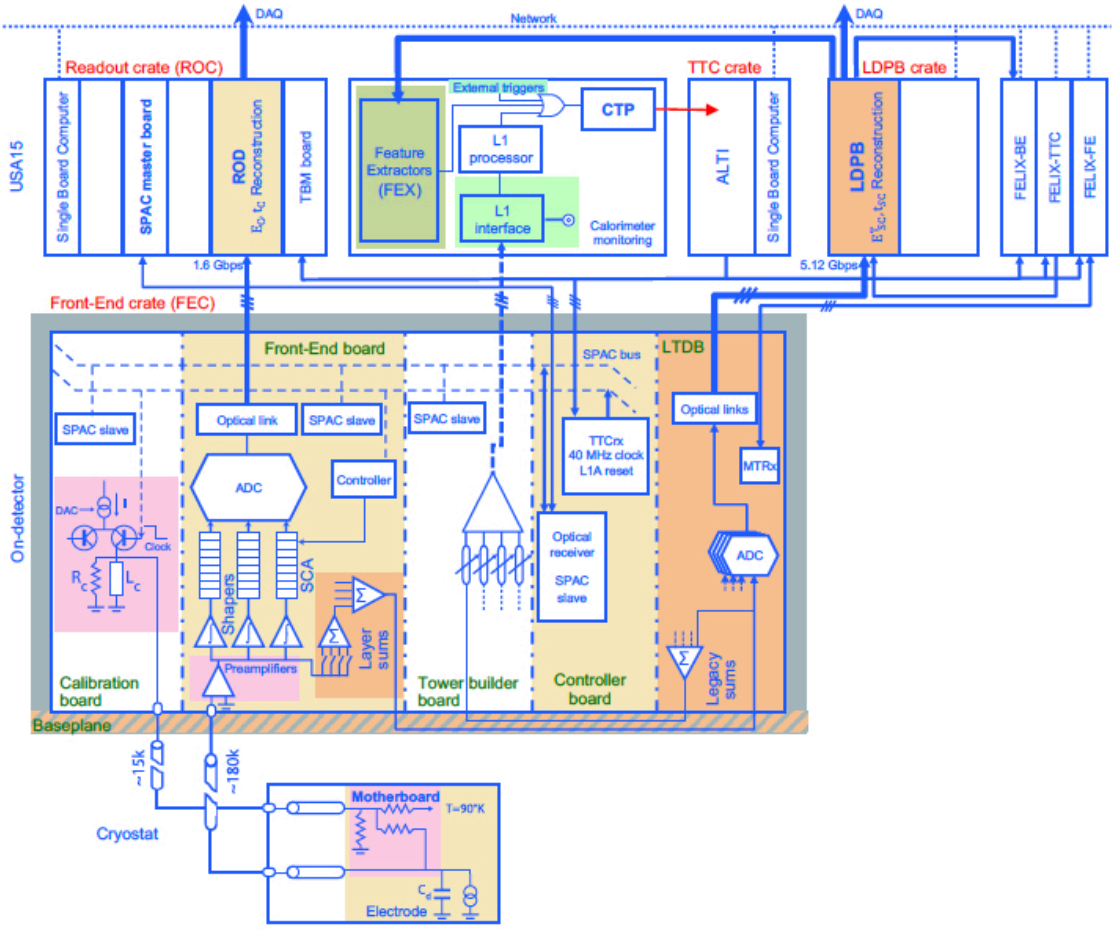

Fig. 3.5 Schematic diagram of the LAr EM calorimeter electronic architecture in LHC Run-3 [14]. The LTDB boards are newly installed during LS2. HEC and FCal electronics are sightly different.

LAr Trigger Digitizer Boards To provide the high-granularity and high-quality information to the upgraded trigger processors FEXs (Feature EXtractors), a new kind of on-detector electronics called LAr Trigger Digitizer Board (LTDB) is installed in the spare slots of the FECs. Figure 3.7 shows the detail of the LTDB boards. An LTDB board is connected to at most 320 supercell signals ("channels") and transmits the 12-bit flash ADC signals to the back-end electronics by optical fibers. The total data transfer speed is 21 Tbps. The 124 LTDBs are equipped with about 12k ADC chips (80 chips used per LTDB, the rest are spared). Meanwhile, the LTDBs also send the summed analog legacy signal to the TBBs, which are used for building the trigger tower. This feature is required to maintain the legacy trigger system as fully operational to accomplish the transition to the new trigger system in Run-3. There is one LTDB per baseplane in each EMB, HEC, and EMEC standard crate, but two for the EMEC special and FCal crates. Therefore the number of LTDBs is different

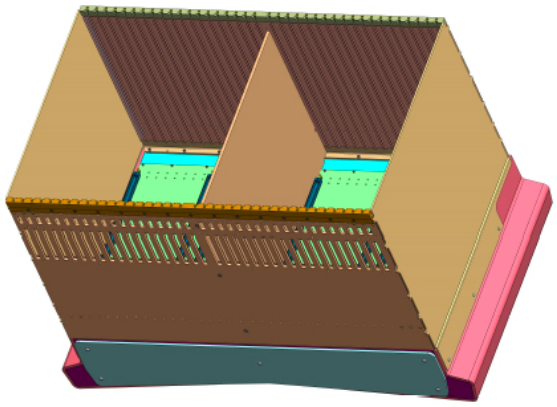

Fig. 3.6 Perspective drawing of a FEC [14]. It is divided into two HFECs (Half FECs) with baseplanes mounted on the pedestal inside the crate.

for each region. Also, LTDBs are named to be "a single character" + "two-digit numbers" + "one or two characters" with the following rules [23]:

- EMB: This type of LTDBs is used for the EMB readout. LTDBs' names starting with I are for the EMBA (EMB on the A-side) and H for the EMBC (EMB on the C-side), and the ones ending with L are for left HFECs and R for right HFECs. Examples: I01L, H02R.
- EMEC Std: This type of LTDBs is used for the EMEC readout. LTDBs' names starting with A are for EMECA and C for EMECC, and the ones ending with L are for left HFECs and the R for right HFECs. Examples: A01L, C02R.
- EMEC Spec 0: The EMEC region that overlaps with the EMB ($1.4 < |\eta| < 1.6$) is read by this type of LTDB. LTDBs' names starting with A are for EMECA and C for EMECC, and the ones ending with S0 are for right HFECs and the S1 for left HFECs. Examples: A02S0, C06S1.
- EMEC Spec 1: The EMEC inner wheel and the last trigger tower of the outer wheel ($2.4 < |\eta| < 3.2$) are read by this type of LTDB. LTDBs' names starting with A are for EMECA and C for EMECC, and the ones ending with S0 are for right HFECs and the S1 for left HFECs.
- HEC: This type of LTDBs is used for the HEC readout. The names starting with A are for HECA and C for HECC, and they are all ending with H. Examples: A02H, C06H.

- FCAL 0: This type of LTDBs reads out the electromagnetic FCAL. The names starting with A are for FCALA and C for FCALC, and the ones ending with F0 are for the right HFEC and the F1 for the left HFEC. Examples: A04F0, C04F0.
- FCAL 1: This type of LTDBs reads out the hadronic FCAL. The names starting with A are for FCALA and C for FCALC, and the ones ending with F0 are for the right HFEC and the F1 for the left HFEC. Examples: A04F1, C04F1.

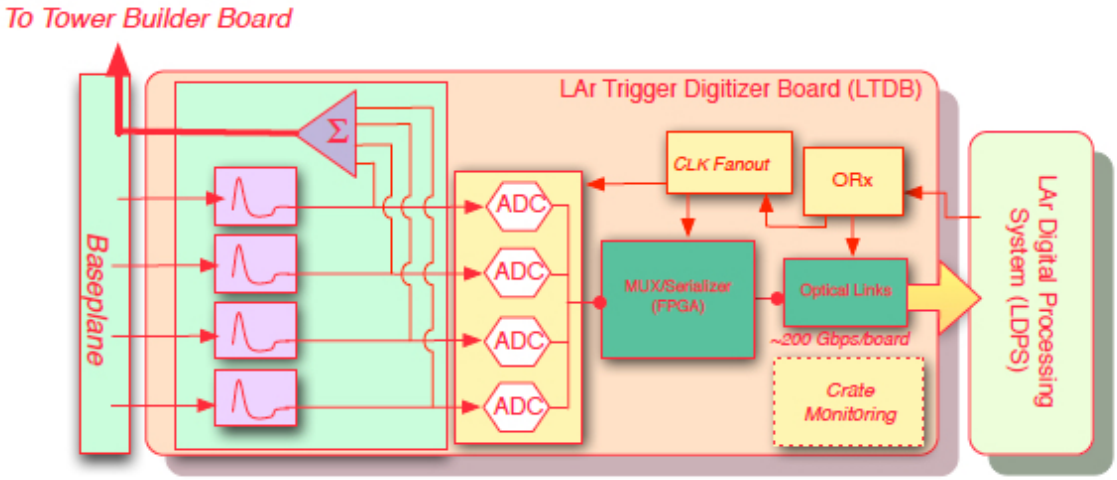

Fig. 3.7 Schematic figure of the LTDB board.

Table 3.2 shows LTDBs set with different types and the detail of connected channels for each type.

Table 3.2 The numbers of channels in the different region of LTDBs and the number of LTDBs for each LTDB type.

LTDB Type	Channels	LTDB per region
EMB	290	64
EMEC Std	312	32
EMEC Spec 0	240	8
EMEC Spec 1	160	8
HEC	192	8
FCal 0	192	2
FCal 1	192	2
Total	34048	124

Optical transmitters Each LTDB is set up with 40 fibers for the data links and 10 for the control links. 5848 fibers in total are equipped by the 124 LTDBs. Figure 3.8 shows the data

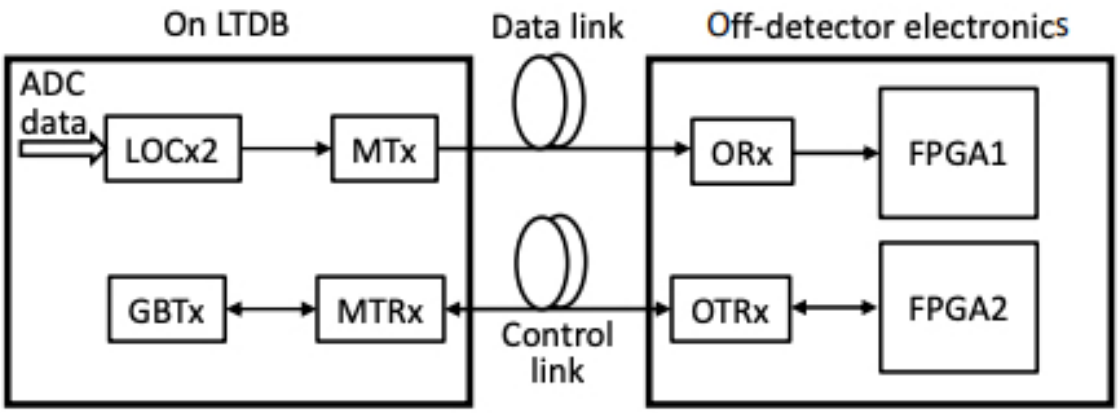

Fig. 3.8 Schematic figure of LTDB optical links [14].

and control links of the LTDB. The new Link-on-Chip (LOC) serializer ASIC named LOCx2 on the LTDB board is used to transmit the high-speed serial data, which are the digital signals from up to 320 ADC channels per LTDB in the format of serial bitstreams [24]. Each LOCx2 can process the data from four ADC chips and transmit them to the back-end via two 5.12 Gbps optical links. The GBT serializer-deserializer ASIC GBTx is used for the configuration, control, and monitoring through five bi-directional control links. The Miniature Transmitter (MTx) and Miniature Transceiver (MTRx) are the optical transmitter and transceiver to fit between the LTDB PCB and the cooling plate [25].

The ATLAS L1 trigger system requires the transmission latency to be fixed and meet the time budge of the ATLAS trigger system. Thus LOCx2 are demanded with a maximum latency of 75 ns [22]. In the commissioning works, the LOCx2 scan is performed to lock the fiber latency and make the data acquisition valid in the digital trigger readout. Otherwise, the ADC values in the monitoring data outputted by LATOME will be set to -1 for the fibers with a bad link.

As a result, the above optical transmitters demand the connectivity check by the test that involves the entire chain of the LAr trigger and the data acquisition electronics on both back-end and the front-end, and the detail of such a test will be discussed in Chapter 4.

3.2.3 Back-End Electronics

Legacy electronics

Readout Crates (ROC) ROCs house the readout driver boards that read the ADC signals from the FEBs and compute energy and time for each cell signal at the L1 trigger rate. SPAC

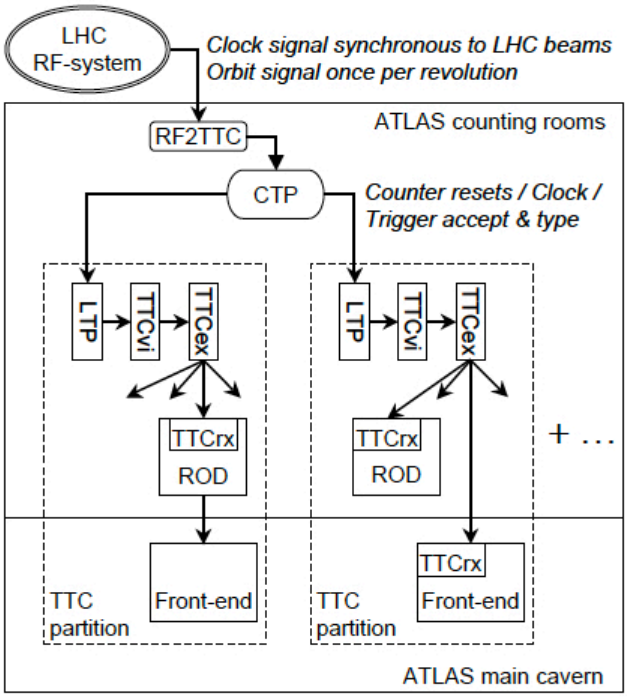

Fig. 3.9 Schematic of the CTP and TTC system. The system distributes the timing signals to all the other system in ATLAS [22]

master boards and the Trigger Busy Modules (TBM) are also housed by the ROC. TBM distributes the TTC signals and receives the busy signals from the RODs.

TTC crates The ATLAS Timing, Trigger, and Control system (TTC) are used to control the subsystem like the new LTDBs and the LDPBs. The VME crates receive the TTC commands from the ATLAS Central Trigger Processor (CTP) system or generate these commands and transmit them to the other boards. Figure 3.9 shows the working flow of the timing control system in ATLAS.

New electronics

LAr Digital Processing System

The new LAr Digital Processing System (LDPS), as shown in Figure 3.10 is installed on the back-end during the phase-I upgrade project. The LDPS is designed to receive the digital signals from the LTDBs on the front-end, calculate the transverse energy for each supercell and send the results to the L1 calorimeter trigger system (L1Calo) with the LHC clock frequency of 40 MHz. The whole system consists of LDPB, FELIX, TTC partition,

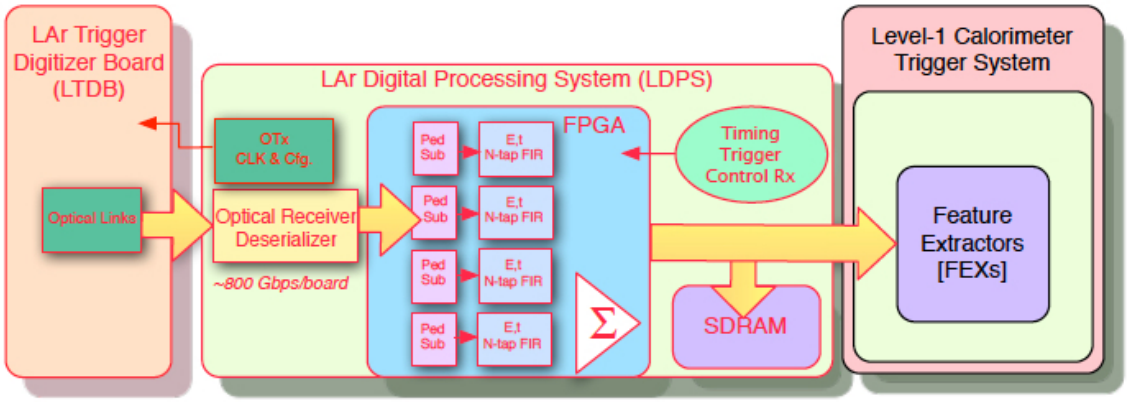

Fig. 3.10 Schematic diagram of the LDPS [22].

Partition Master, PC farm, and Shelf Manager. The detail of the system will be discussed in Section 4.1.

The new LAr Trigger Digitizer Boards (LDPB) is the most important part of all the physical elements. The ADC signals of all the 34k supercells are sent from LTDBs to LDPBs and processed there. The LDPBs compute the supercells' E_T and transmit them to the L1Calo, which consists of a set of Feature Extractors (FEX). Three Advanced Telecommunications Computing Architecture (ATCA) shelves are utilized to house the LDPBs and their following subsystems. Each shelf houses 12 LDPBs and two switchblades.

LAr carrier The LAr carrier (LArC) is an ATCA standard cut-out blade with a Rear Transition Module (RTM) to host LATOME boards and transmit data with the ATLAS Trigger and Data Acquisition (TDAQ) system. The LArC utilizes the ALTAS standard IPMC to provide all board power and sensor management functions. The RTM is used to connect 5 TDAQ channels via SFP+ modules, and all TDAQ connections are routed through the Xilinx Virtex-7 FPGA. In total, 30 LArCs corresponding to 30 LDPBs are installed to support 116 LATOMEs, where 28 LArCs host 4 LATOME boards, and two are installed with 4 LATOMEs that are used for receiving signals from FCal.

LAr trigger processing mezzanine The LAr Trigger prOcessing MEzzaine (LATOME) boards read data from 48 optical fibers, processes the data, and send the results to L1Calo with the 48 output optical fibers. The board fulfills the Advanced Mezzanine Card (AMC) to provide connectivity. Each LATOME board is connected to input fibers coming from up to 3 different LTDBs. On the board, the Intel Arria 10 FPGA is equipped to support the high-speed computation of energy. Figure 3.11 shows an example of the LATOME. The black front connector gathers the 48 output fibers together to transmit new FEX system data at 11.2 Gbps, and the green ones receive data from LTDBs at 5.12 Gbps with 48 input fibers.

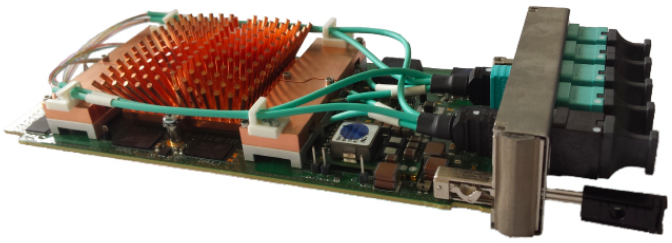

Fig. 3.11 LATOME board equipped with optical fibers.

Thus, 5568 input fibers are equipped on the LATOMEs to read out data from the LTDBs. Firmware on the LATOME boards performs the following four main functions.

- handles the input data from the LTDBs with high-speed links.
- performs the OF (optimal filtering, see later) algorithm to reconstruct $E_{\mathrm{T}}^{\mathrm{supercell}}$ every 25 ns and identifies its Bunch Crossing, which corresponds to the timing when its energy is injected. The latter is called "bunch crossing identification" (BCID).
- outputs results to the L1Calo with high-speed links.
- processes and buffers data to be delivered to the TDAQ readout chain and the monitoring.

LATOME firmware To accomplish the above requirements, several FPGA firmware modules, as shown in Figure 3.12, have been developed. *Input stage* (Istage) block aligns all 48 input fibers together. *Configureable remapping* (Remap) block reorders input data according to detector topology. *User Code* block reconstructs $E_{\mathrm{T}}^{\mathrm{supercell}}$ and provides some quality bits to the *output summing* (OSUM) block. OSUM block groups the data from user code, calculate the sums over specific $\eta - \phi$ plane, and transmits data to FEX output fibers. Note that the user code has been developed by the Utokyo group.
Intelligent platform management controller (IPMC) The IPMC supports the hardware management system for ATCA shelves and LArCs, which provides the ability to manage the power, cooling, and interconnect needs of intelligent devices.

Feature Extractor

The improved granularity from the supercells will give rise to better isolation, which leads to the lower energy thresholds preservation. In order to make full use of the improved readout features, the new feature extraction (FEX) modules are performed in the L1Calo system for the purpose of object recognition. Three kinds of FEX modules are installed in the phase-I

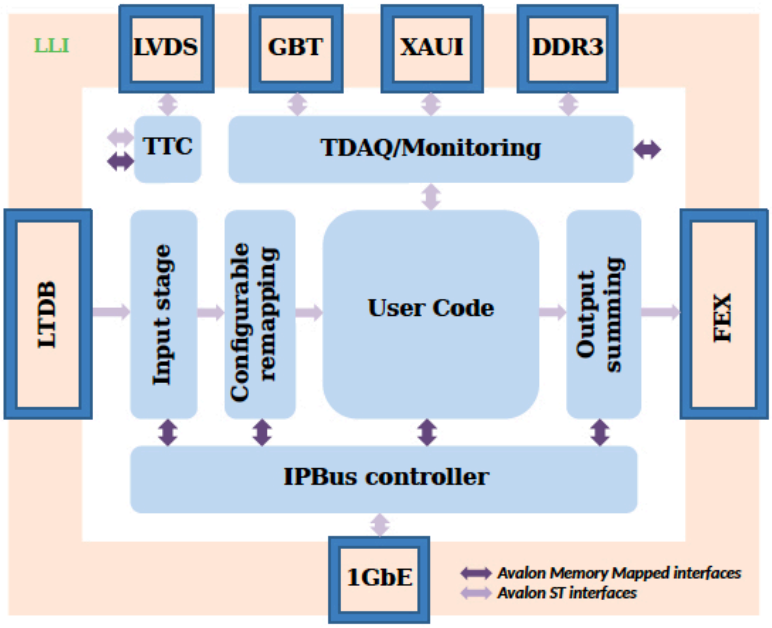

Fig. 3.12 Schematic diagram of LATOME firmware.

upgrade: eFEX for electrons and photons, jFEX for jets and $E_{\mathrm{T}}^{\mathrm{missing}}$, and gFEX for jets that $\Delta R > 1.0$. Specifically, the eFEX subsystem employs new cluster-finding algorithms on the higher granularity data to produce more refined Trigger Objects (TOBs). The jFEX subsystem uses jet-finding algorithms, and gFEX is designed to identify large-area jets using detector data with a granularity of 0.2×0.2 in the $\eta - \phi$ plane. Figure 3.13 shows the trigger efficiency comparison between the electron trigger used in Run-2 and the eFEX with different thresholds using the $Z \rightarrow ee$ Monte Carlo simulation data. Distinct improvement can be seen from the plot. The threshold of 21 GeV is chosen to have the same rate as the Run-2 trigger.

3.2.4 Energy and Timing Reconstruction in Run-3

The reconstruction of energy and timing is done by both the main readout and the digital trigger readout at the LAr calorimeter. Both readout systems use the optimal filtering algorithm for the calculation. The energy computation in the digital trigger readout is performed on both the user code block shown in Figure 3.12 and the offline monitoring data analysis.

Energy reconstruction

As shown in Figure 3.14, the amplitude of the bipolar pulse is proportional to the energy. The proportionality coefficient is derived from the calibration run, and the amplitude of the

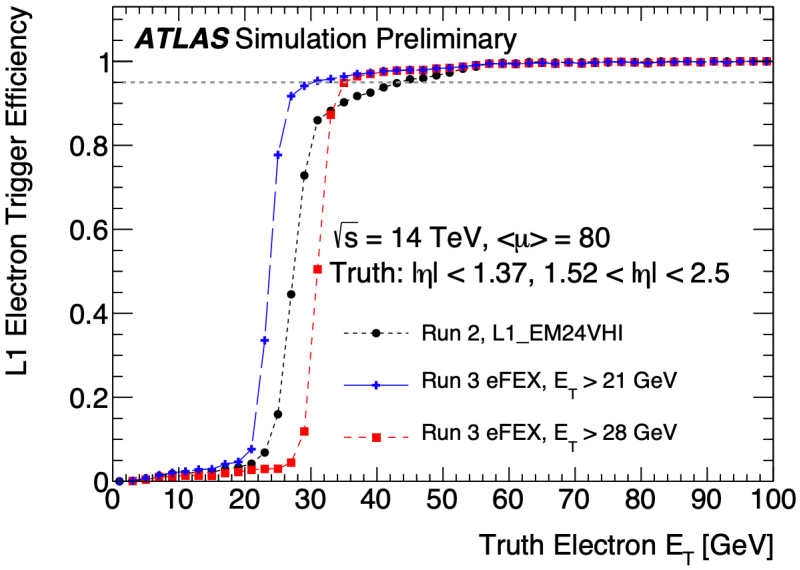

Fig. 3.13 Trigger efficiency comparison between the trigger implemented in Run-2 and Run-3 [26].

sampled signal is obtained from the sample points neighbored the peak. Whereas, if only one sample point is used for the amplitude estimation, electric noise and the pile-up noise may introduce the fluctuation of the reconstructed energy for about 200 MeV. Four sample points are utilized to mitigate such fluctuation, and the energy, therefore, can be calculated by the equation 3.1.

$$E_T = \sum_{i=0}^{3} a_i(S_i - p), \tag{3.1}$$

where a_i is the coefficient for each sample point, S_i is the ADC value of the sample point, and the p represents the pedestal value. Notice that the constraint of minimizing the noise is raised here to derive the coefficient a_i with the method of Lagrange multipliers [27].

Timing reconstruction

The variable τ is introduced to measure the delay of the real signal from the ideal sample timing. The reconstruction of τ is also done by the optimal filtering algorithm with the following equation:

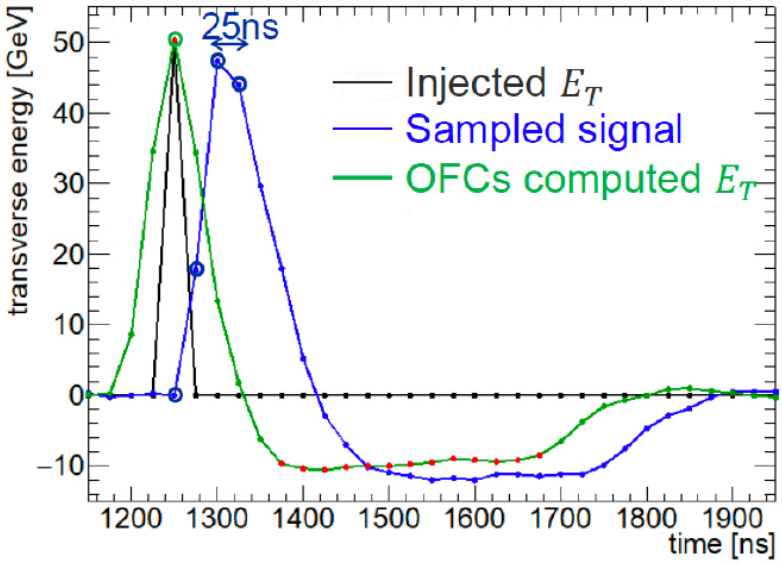

Fig. 3.14 Energy reconstruction of the injected pulse with 50 GeV E_{T} . The interval of samples is 25 ns, which is the same as the LHC bunch clock. The sample points used for energy reconstruction are the ones with the blue circle. The red sample points represent the corresponding reconstruction result, and the one with the green circle passes the τ criteria [27].

$$E_T\tau = \sum_{i=0}^{3} b_i(S_i - p), \tag{3.2}$$

where b_i is the coefficient for each sample point, and is calibrated together with a_i. The reconstructed τ can be derived from Eq. 3.1 and 3.2. The coefficients a_i and b_i are called OFC (optimal filtering coefficients) and details of their calibration are discussed in Chapter 5.

τ criteria

The E_{T} and τ reconstructions are done by both LATOME and offline analysis. And for the reconstructed E_{T} and τ in the LATOME, the computation is done every BC. To choose the correct phase among all the BC, a constrain on the timing is performed within the interval of 25 ns. This is called "τ criteria".

$$\begin{cases} -8\ \mathrm{ns} < \tau < 16\ \mathrm{ns}, & \text{if } E_{\mathrm{T}} \geq 10\ \mathrm{GeV} \\ |\tau| < 8\ \mathrm{ns}, & \text{if } E_{\mathrm{T}} < 10\ \mathrm{GeV} \end{cases} \tag{3.3}$$

The tight cut for low energy is to compress the influence from the pile-up and electronic noise. The outputs of the optimal filter are all set to 0 if the condition is not met, and the only-passed BC is selected by the above condition.

3.3 Installation Status

The installation of the front-end and back-end electronics needs lots of effort. The following main steps have been proceeded to install front-end electronics, which was started in April 2019:

1. Extract boards on the FEC from the detector.
2. Exchange an old baseplane of the FEC with a new one, as well as the LSBs.
3. Reinstall legacy boards to the FEC.
4. Install the two LTDBs.
5. Cable the FEC.
6. Replace LVPS cooling hoses.

The installation status of the front-end electronics in December 2021 is shown in Figure 3.15. LTDBs are all installed.

On the other side, about the installation on the back-end, three ATCA shelves and LArCs are already installed. Figure 3.16 shows all the three ATCA shelves and how the LArC is inserted into the ATCA shelf.

The LAr group, including me, has been proceeding with the commissioning work to test the newly installed electronics. There was a pilot run in October 2021, and data was taken with the new digital trigger system.

This thesis reports my contribution to the commissioning work: a connectivity check and a timing alignment in Chapter 4. In addition, this thesis gives results of the analysis for the data taken by the new readout system in the pilot run in Chapter 5.

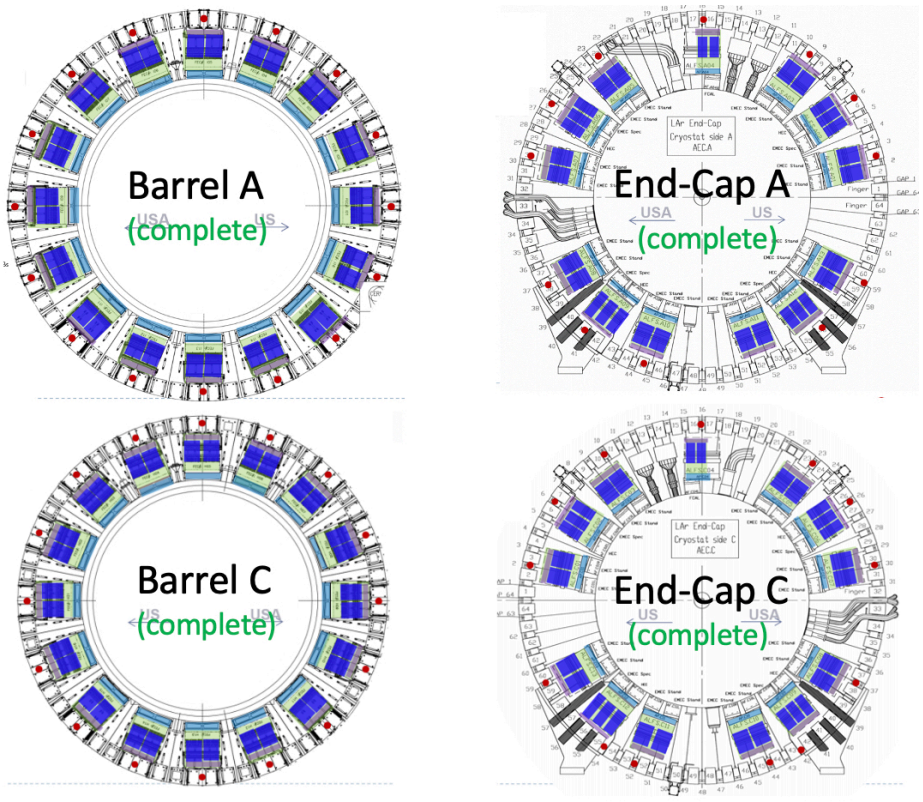

Fig. 3.15 Front-end installation status in December 2021 [28]. Installation of phase-I on- and off-detector electronics are all complete.

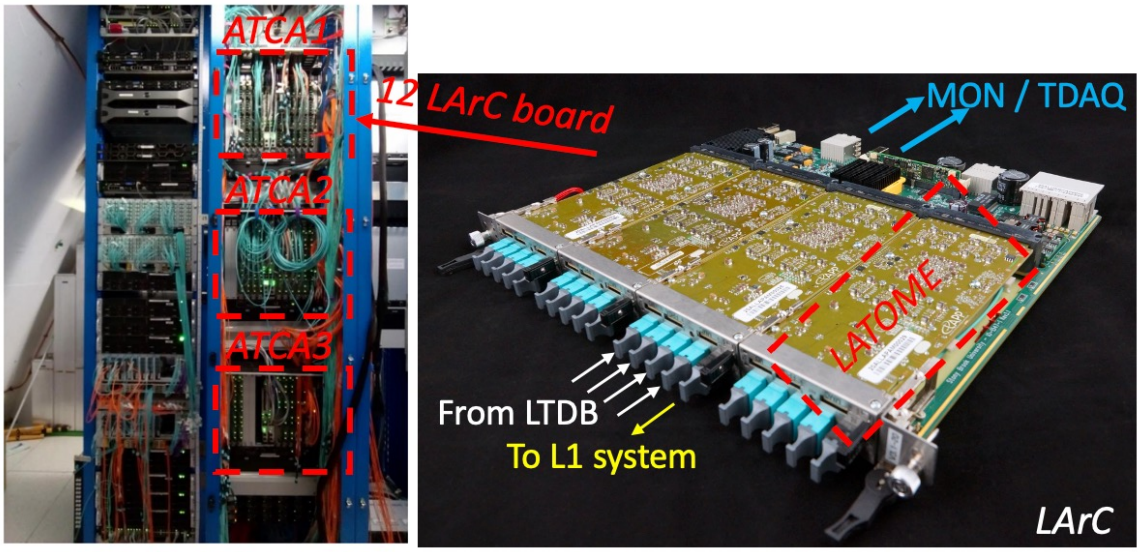

Fig. 3.16 Current status of ATCA shelves. Three ATCA shelves have been installed in the USA-15 counting room (left). A photo of LArC is also shown on the right.

Chapter 4

Connectivity Check and BCID Calibration

The new digital trigger system will be replaced with the legacy one during the LHC Run-3 experiment so that the commissioning work for the digital trigger readout has to be performed as much as possible and as fast as possible. As mentioned in Section 3.2.2, during the LS2 commissioning period, the pulse signal is sent by the calibration board on the detector. The calibration pulse sent by the calibration board is then detected by the LAr cells, and the signal is transmitted to the three kinds of readout paths as shown in Figure 4.1: main readout path, legacy trigger path, new digital trigger path.

For the digital trigger readout, the data path in the front-end is: calibration board (on-detector) $\rightarrow$ FEB (shape analog signal to bipolar pulse) $\rightarrow$ LTDB (digitize the infected bipolar pulse). The data path in back-end is shown in Figure 4.2. The LDPBs receive the input signals from LTDBs and reconstruct the E_{T} and τ parameters on the LATOME FPGA. The information is sent to the trigger system, where the trigger decision of the level-1 is made for each event. Once the level-1 accept (L1A) is issued, data is sent to the Front-End LInk eXchange (FELIX) system and then to software ROD (SWROD), and finally pulled by HLT and added to the ATLAS event. SWROD is a new feature introduced by the phase-I upgrade to replace the combination of the ROD and the ROS. It has already been installed and implemented to record data in the pilot run in October 2021.

In order to make sure that the new complex data processing system can handle over 34k supercells properly, many efforts on the commission of the digital trigger readout are made. The commissioning works to which I have largely contributed during LS2 are listed as follows:

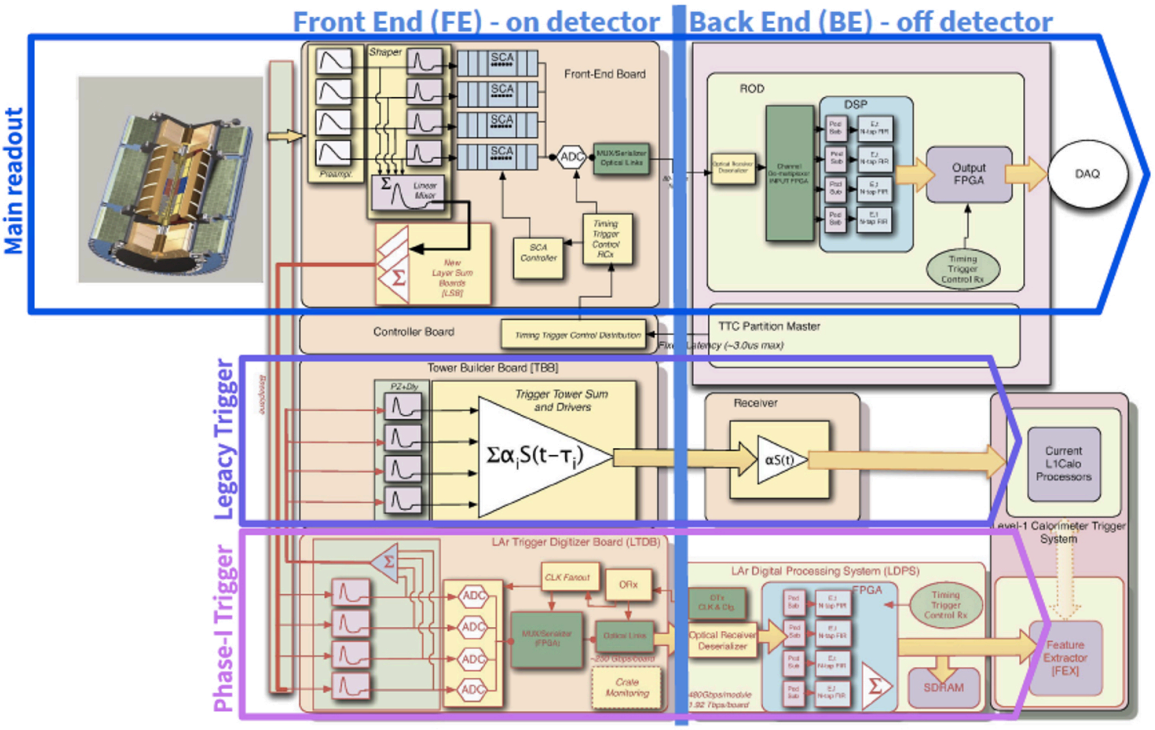

Fig. 4.1 Schematic diagrams of the readout system. Three kinds of paths are prepared. From top to bottom, they are the main readout, legacy trigger tower, and the new digital trigger [22].

- **Shaper SWitch (SSW) scan** The SSW scan is performed to validate the digital trigger readout connections and verify the supercell mapping. It also checks the pulse for each supercell.

- **Pulse-all runs and BCID calibration.** The pulse-all run is a pulse injection mode controlled by the calibration board. All supercells will be pulsed with a certain DAC value, which determines the E_T of the calibration pulse. By utilizing signals from the pulse-all run, the stability of the pulse shape is checked, and several quality factors to the expectation are compared. In this thesis specifically, to align the sampling timing of the pulse, the timing of the pulse (BCID) between the main readout and the digital trigger readout will be compared.

- **Calibration runs** The calibration runs collect data for pedestal, ramp, and delay runs and build a database to be used as reference. With the aligned timing and delay runs, the OFC set with different phases are calculated, and the selection for the best fitted OFC for E_T and τ reconstruction is then made. The ramp runs include the signals with different DAC values, which can be used for the calculation of the least significant

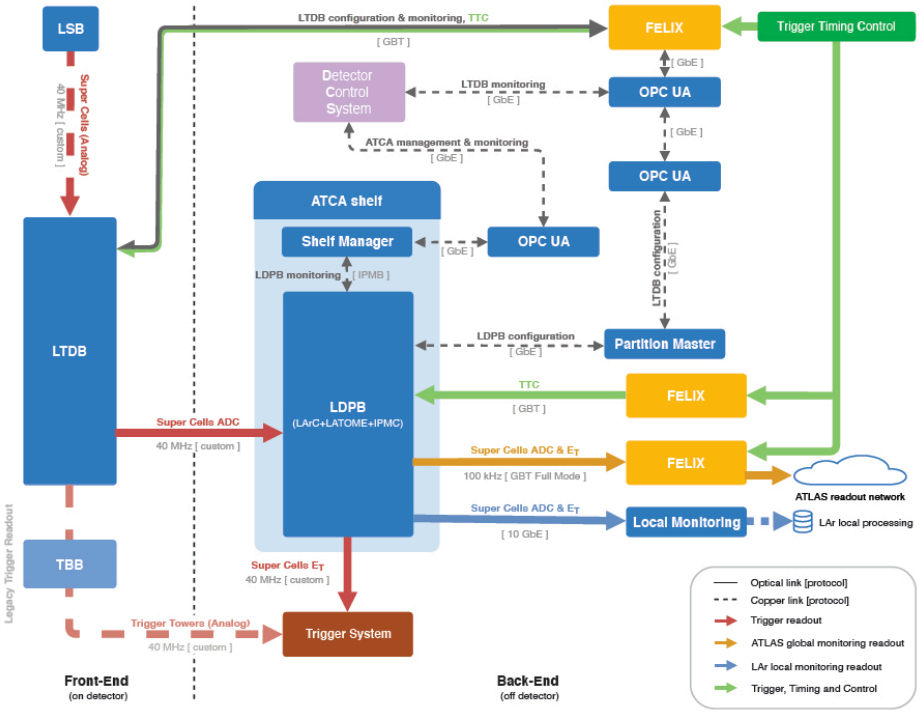

Fig. 4.2 Data flow of the digital trigger readout system in back-end [14].

bit (LSB). The reconstructed E_T and τ can therefore be calculated with the calibrated LSB and OFC.

- **Adjustment with Pilot Run data** LHC pilot run that uses real beam is performed in October 2021. The LAr calorimeter also participated in the operation to test the digital trigger readout, the main readout, and the legacy readout. The analysis of pilot run data and the comparison of the digital trigger readout and the main readout is made in the following chapter.

This chapter mainly introduces the first two steps. OFC calibration with calibration runs and energy reconstruction with Pilot Run data are discussed in Chapter 5.

4.1 Shaper Switch Scan and Connectivity Check

As discussed in Section 3.2.2, many new electronics like baseplanes and LTDBs are installed in LS2. Therefore, it is checked if each readout path is established as expected after the installation of the new front-end and back-end electronics. In order to check the supercell connectivity and internal mapping from LTDB to LATOME, a low-level check on hardware and the shaper switch scan (SSW) are performed. To apply an SSW scan, the calibration

board sends signals to all supercells, and then the shaper chips controlled by the shaper switch determine which supercell to read. Figure 4.3 shows the functionality of the shaper chip in the FEB, and figure 3.3 shows the signal output (bipolar) from the shaper chip. The sampling positions are separated by 25 ns. By reading raw ADC data from the monitoring output of the User Code in LATOME (see figure 3.12), pulse shape is checked. Also, according to the shaper switch configuration files, whether the channels are pulsed with the correct supercells is checked.

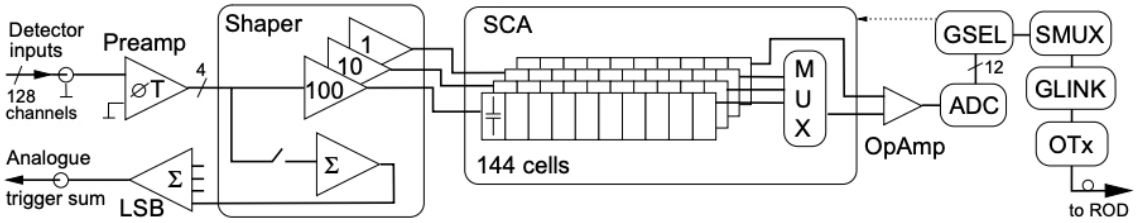

Fig. 4.3 Block diagram of the FEB architecture, the shaper chip is controlled by the shaper switch to form the input signals from LAr Cells [29].

4.1.1 Workflow of Connectivity Check

Specifically, there are mainly two steps to accomplish the whole check procedure. Each step performs its functionality by changing the pattern of enabled supercells. Figure 4.4 shows the schematic view of how the shaper switch works. The framework is done by following procedures.

1. Figure 4.4a shows the first step of the SSW scan. The SSW on the FEB enables all supercells and sends pulse to the LATOMEs on back-end. The raw ADC data that includes all channels are read from the monitoring stream and then used for offline analysis. This pattern of enabled supercells lasts several seconds.

2. Figure 4.4b shows the second step of the SSW scan. After the pulse-all runs, only one supercell is enabled by the SSW. Therefore, by searching for the only pulsed channels from the monitoring stream data, the mapping between individual supercell and channel on LATOME can be specified.

3. After sending pulses to a supercell for 0.5 seconds with the frequency of 40 Hz, the SSW will disable all the supercells for another 0.5 seconds and then enable another supercell that hasn't been pulsed before. Such a pattern lasts until the scan runs overall target supercells.

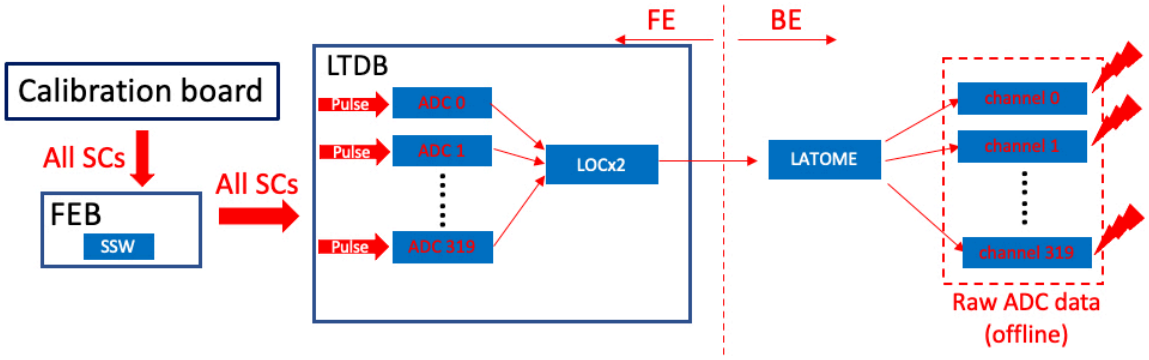

(a) Step 1: Send pulse to all supercells

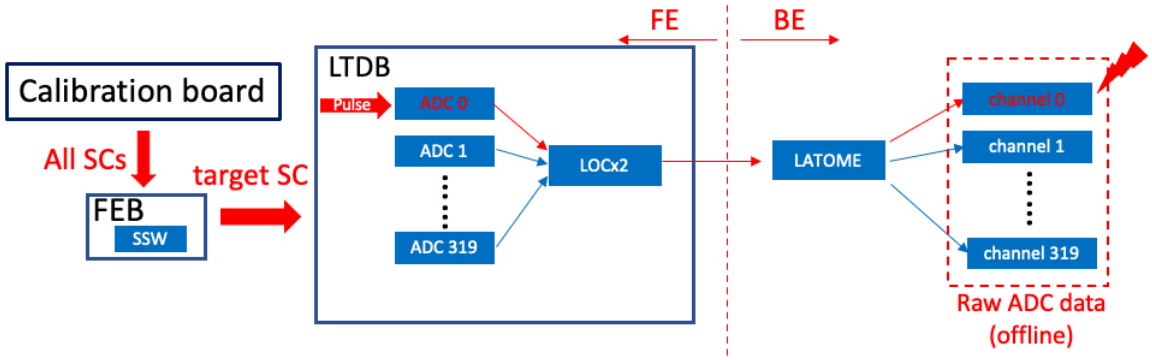

(b) Step 2: Send pulse individually.

Fig. 4.4 Schematic figures of SSW scan workflow.

As for the current configuration, the L1A rate is 40 Hz, which means every second includes about 40 pulsing events. Every SSW scan is performed for supercells on a single HFEC. The plot of pulsed events is shown in Figure 4.5. The marked points mean that the pulse signal of the channel is detected in the corresponding events. In Figure, the first 100 events are the pulse-all pattern, which is described in Figure 4.4b. And the discrete dots after the pulse-all part show how the channels are pulsed with the shifting of SSW. Each LATOME holds up to 320 channels that connect to supercells, respectively.

4.1.2 Pulse Detection Criteria

The calibration pulse is stored in an array with a length of 32, and the ADC values of the samples are proportional to the energy. Figure 4.6a shows the legit pulse, and figure 4.6b shows an example of the deformed pulse. In order to exclude deformed pulses and noise, the following criteria are applied to the barrel and end-cap pulse.

1. **Peak detection** The first criterion is to check the peak. As shown in Figure 4.6a, suppose the peak is at the j^{th} sample, and the height of the pulse is defined as the

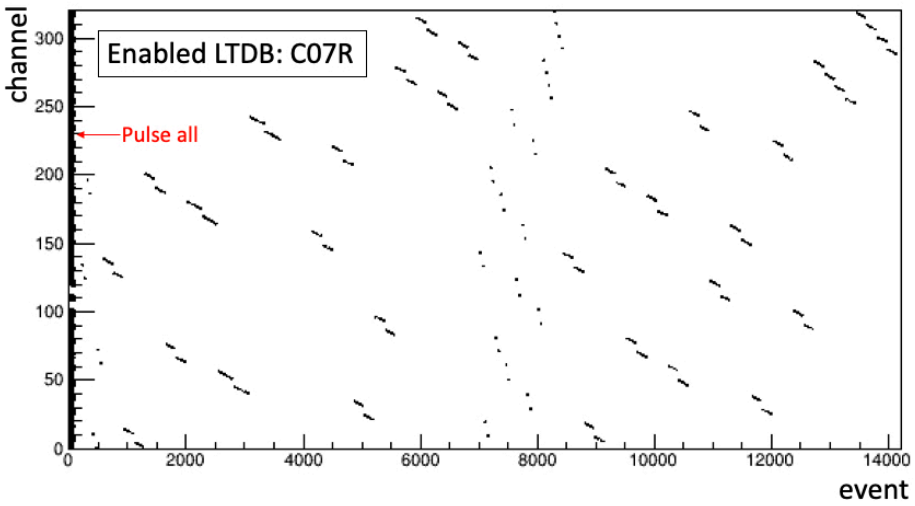

Fig. 4.5 Pulse pattern of the SSW scan for a single LATOME. First is the pulse-all run and then come with the solely pulsed channel. A dot represents for about 20 continuously pulsed events.

difference between the peak sample and the first sample. The threshold of the pulse height is 15 ADC counts. Additional comparison between the $(j-2)^{th}$ sample and the $(j-1)^{th}$ sample, as well as the comparison between the $(j+2)^{th}$ sample and the $(j+1)^{th}$ sample are made in order to require the crest structure.

2. **Undershoot detection** The undershoot structure of the bipolar pulse is also required. Samples behind the trough (red rectangle in Figure 4.6a) are supposed to be less than $(j^{th}\text{sample} + 1^{st}\text{sample})/2$.

3. **Bipolar structure** The bipolar structure is performed to check the rough shape of the pulse. The depth is defined as the difference between the first sample and the nadir sample. For the pulses from supercells on EMB and EMEC, there is no limitation on their depth. Only the nadir of the FCal pulse is required to be 4 ADC counts smaller than the 1^st sample. Also, the crest of the signal needs to appear earlier than the trough. Such requirements meet the assurance of avoiding misjudgment due to bit flipping.

4. **Pedestal level** The final condition requires the pulse are all around the pedestal level, which is calculated by the mean value of the first sample of the first 100 events.

FCal pulse The FCal are specially designed to detect in the high η region. Therefore the pulse shape from FCal is slightly different from the pulse from the barrel and end-cap region. As shown in Figure 4.7, a sharper crest and larger depth are required to detect the FCal pulse.

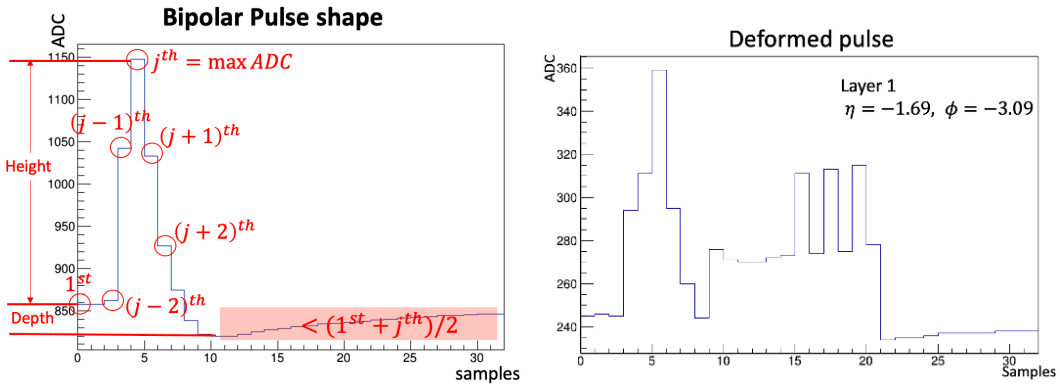

(a) Normal Pulse shape and the terminology. (b) An example of deformed pulse.

Fig. 4.6 Pulse detection algorithm for SSW scan. Pulse from FCal is sightly different.

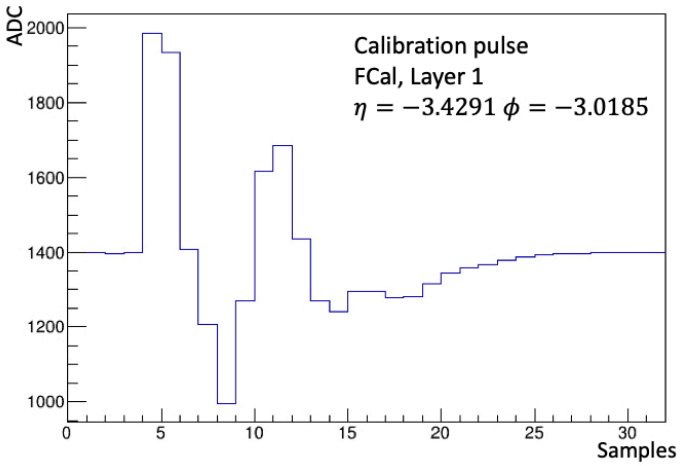

Fig. 4.7 The example of the FCal pulse.

4.1.3 Scan Validation Algorithm

All channels are classified into several statuses due to the corresponding issues to identify whether the channels are pulsed as expected in the SSW scan. Figure 4.8 shows the workflow of the validation algorithm. The blue blocks indicate the different channel statuses. The problems may be caused by different reasons. The analysis is followed by these conditions:

1. Scan Step 1 and Step 2 in Figure 4.4 and search for channels with -1 samples. In case the fiber is not locked, the channels on that fiber will output the negative value ($= -1$). Such channels are called "negative channels". The CLKDES scan needs to be performed to fix such problems.

2. Scan step-1 and step-2 in Figure 4.4 and perform the preselection. The preselection is to exclude the channels that are not pulsed. The only criterion in this procedure is that the pulse height should larger than 15.

3. Scan step-1 and step-2 in Figure 4.4 and perform the exclusion of abnormal channels. The program runs over the whole scan and counts the number of pulsed events for each channel. According to the pattern of pulsing supercells in Figure 4.4b, the pulsed events should not be more than 800 in total for each supercell. Channels that are pulsed too many times are not expected, and therefore such channels are ignored in the following analysis. Otherwise, the search for solely pulsed channels would be difficult. This kind of issue is frequently met in the early SSW scan. However, after several SSW, the system becomes more stable than before, and this issue barely happens again.

4. Scan step-1 in Figure 4.4 and check the pulse shape of all channels. Channels with a reasonable number of pulsed events are checked with the previous 4 criteria. The pulses that do not pass the selection are recognized as those with deformed shapes and will also be excluded from the following analysis. The issue may be caused by the wrong ADC configuration or other hardware problems.

5. Scan step-2 in Figure 4.4 and search the pulsed channel. Referring to the figure 4.4b, in step 2 of the scan, each channel should be only pulsed once within 0.5 s. Therefore if the SSW does not work properly, the target channel may not be pulsed during step 2. The missed channels are categorized as "only pulsed in pulse-all".

6. The crosstalk events are also checked in step-2. The crosstalk events include several different pulsed channels, which are not expected. Thus, the "crosstalk channels" are excluded from the following analysis. This kind of issue rarely occurs since the system becomes more and more stable.

7. After excluding the above problematic channels, the pulsed channels are checked for their pulsing duration. Although the expected pulse duration is 0.5 s, the SSW sometimes delays the switch of the target supercell. In case too much delay is brought to the scan or the SSW doesn't work as expected, this selection mechanism is introduced. The expected number of pulsed events for a good channel is around 20. Therefore if the number of pulsed events for a particular channel is less than 5 or more than 40, the channel will be categorized as a "bad channel".

8. The good channels are finally selected after the above steps. And the pulse order of the good channels is compared with the order in the list of target supercells. With the

comparison between the offline analysis result and the origin configuration file, the list of swapped supercells and ones with correct mapping is therefore obtained.

Figure 4.9 gives a glance at the validation result of the SSW scan for LTDB C12S0. The channel list is sorted by order of target supercells shown by the index. The "SCNAME," "Channelid," and "SC_ONL_ID" column in the list represents the identification of a supercell or channel. The left part of the list indicates the pulse injection order of the target supercells. The right side shows the observed pulsed channel sequence. The hit status means that the observed pulsed channel is what is expected in the target list. The channels with the status "shifted" are the ones that are not pulsed in the expected order. The arrows show how these channels are misordered. What's more, several problematic channels are also observed in the scan, the "negative channel" 1J_M1, 1J_M2, and the "no pulse channel" 2F_M2.

4.1.4 Validation Status and Auto-processing System

The pulse detection criteria are performed to check if the target channels are validated. Hence, the result of the SSW scan, which categorizes the channels into several statuses, indicates the potential issues on the detector, LTDB, and LATOME. The problematic channels can therefore be summarized into two types as follows:

- **Good but swapped channels** The stable and good shape pulse signals are observed from the channels of this type, which means the data acquisition is good as expected on the chain. However, the mapping for the channel may not be correct. As shown in Figure 3.5, the calibration chain may be performed with the wrong channel mapping. In the front-end electronics, the test pulse signal is read out from the motherboards in groups of 8 channels for the barrel. Then the signals are sent to the FEB and then sent to LTDBs and the legacy trigger. The connectivity check of FEB is already done by Run-2. Whereas on the LTDB, the numbering of ADC chips may be mistaken, as well as the optical fiber mapping from the FEB to LTDB and from the ADC channels to the LOCx2. What's more, as the data path on the back-end has shown in Figure 3.10, the mapping of optical fibers that transmit data from the LTDB to LDPS and the pinning of LATOME input are also may not correct. Even inside the cryostats, the swapped cabling of supercells is observed from the SSW scan, which is consistent with the observation in the former report about the swapped channels [30].

- **Problematic channels** The problematic channels are more likely as the by-product of the connectivity scan since the pulse shape detection is applied in the algorithm. They are the channels with a status other than hit and swapped in Figure 4.8. Sometimes

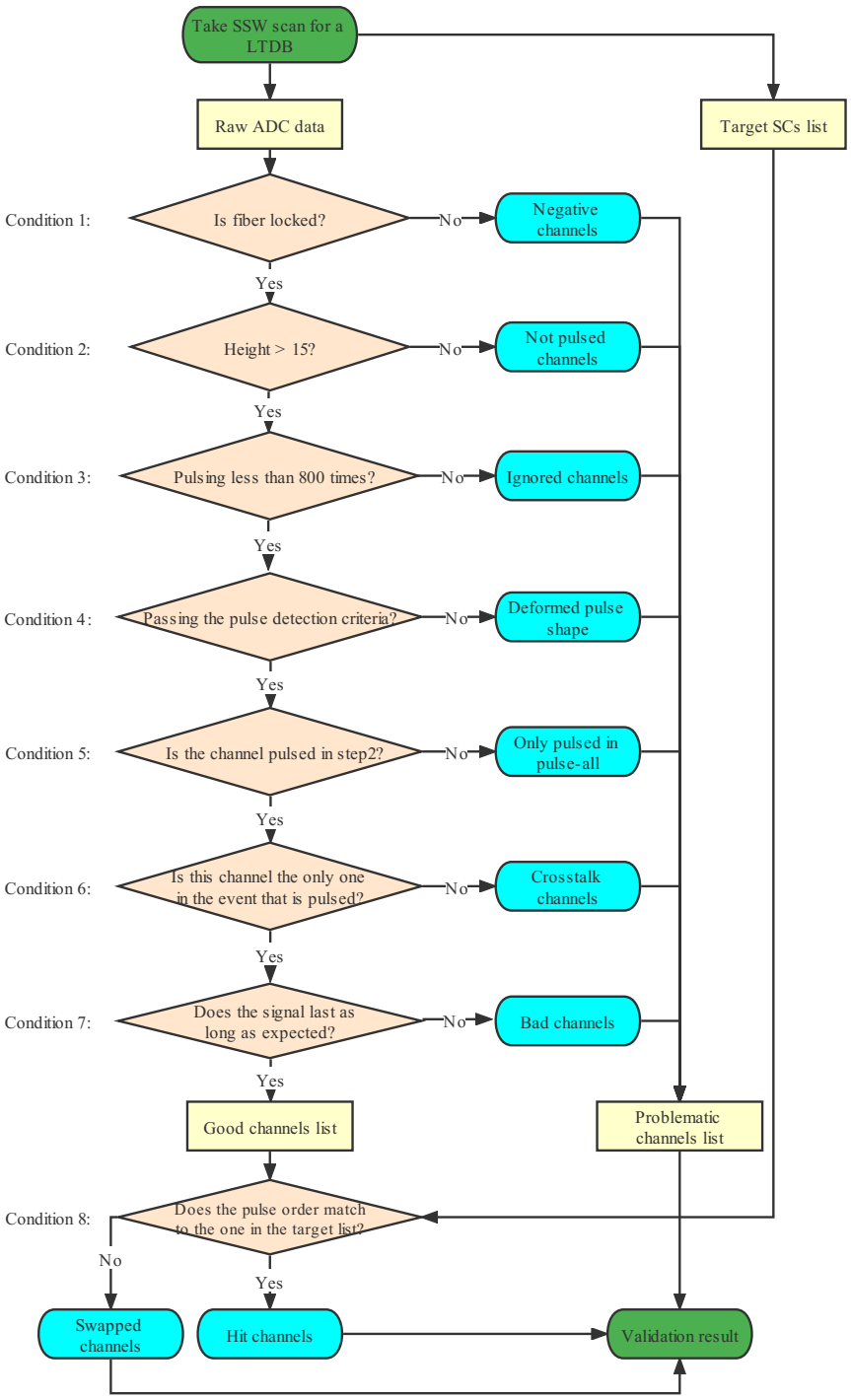

Fig. 4.8 Flow diagram of the pulse validation algorithm. The blue rounded rectangles indicate all possible channels statuses.

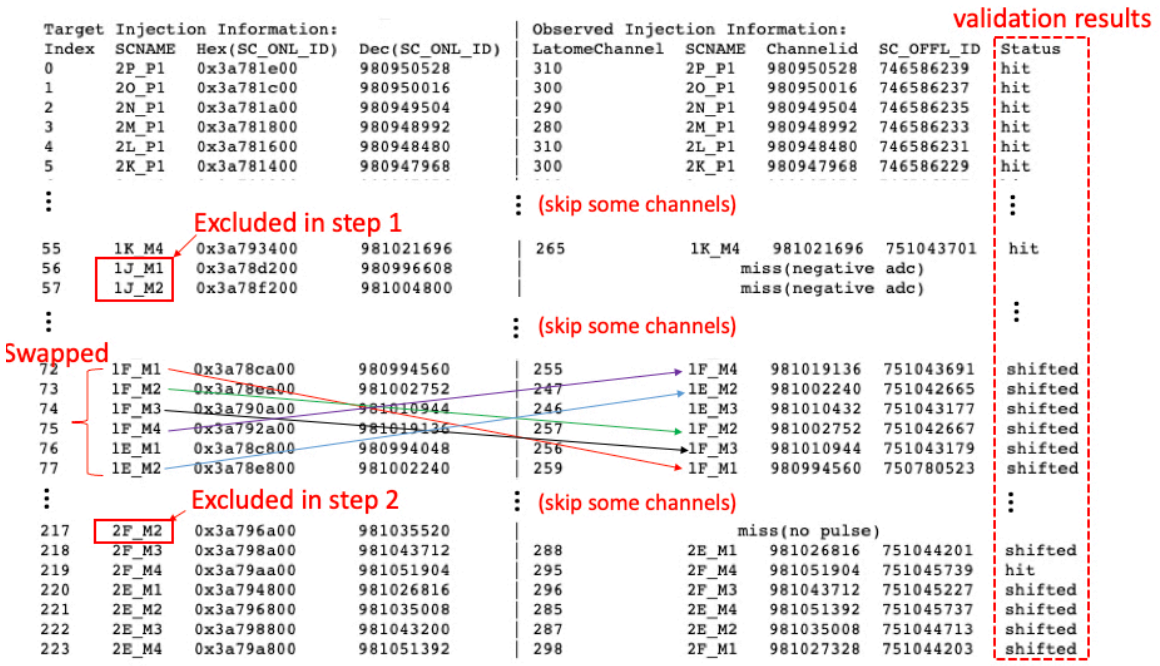

Fig. 4.9 An example of the validation result for a single LTDB. Several different kinds of channel status are observed.

channels with -1 ADC values are observed. They are caused by the unlocked fiber on LOCx2, which is discussed in the optical transmitter part in Section 3.2.2. Most of them can be fixed by the LOCx2 scan. And channels with deformed pulse shapes are the ones having the wrong ADC configuration of the ADC chips on the LTDB. Most of them can be fixed by the full ADC calibration.

The validation for all LTDBs and LATOMEs can be pretty heavy since the calibration run and SSW scan are taken frequently. Therefore an online validation tool has been developed. Figure 4.10 shows the interface of the tool. With this tool, the LAr calorimeter developers can easily take calibration runs and SSW scans for any LTDB. And then analyze the data automatically.

The SSW scans for all LTDBs are done at least once until 29/12/2021, and many problematic channels are reported. Figure 4.11 shows the validation status on 16/09/2021 and 29/12/2021. Supercells in the regions with different colors are indicated by:

- Blue region – Validated Channels. They are classified into the hit channels in the above algorithm.

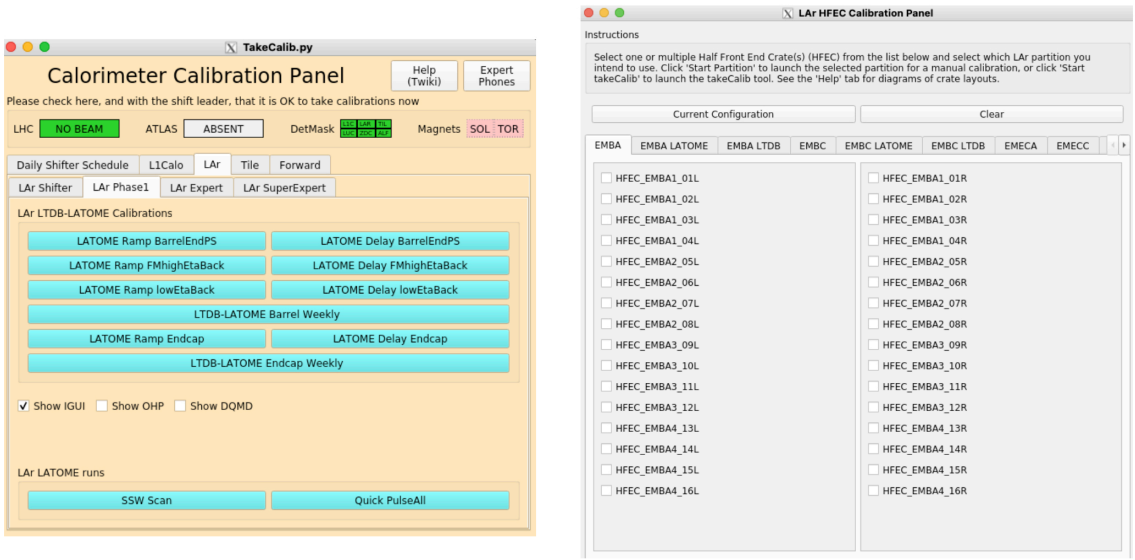

Fig. 4.10 Online validation tools.

- Green region – Channels swapped at somewhere. The issue could occur at both the front-end and back-end, even in the detector. For now, all found swapped channels have been fixed.

- Yellow region – Problematic channels. For example, deformed pulse, as shown in Figure 4.6b, is mainly caused by the incorrect ADC configuration. And sometimes, samples of certain channels are set to -1, which usually indicates a fiber link issue.

As shown in Figure 4.11a, several swapped supercells are observed from the SSW scan on September 16th. The mapping for these supercells needs to be updated and fixed. And as shown in Figure 4.11b, all swapped channels and many problematic ones are already fixed in December 2021. Most problematic channels are caused by the unlocked fibers and the incorrect ADC configuration. Actually, the fibers need to be locked again every time after the accidental power cut of the system. Such an accident may change the system latency sightly, and the CLKDES scan should be applied to fix the issue. The unlocked fibers bring the data acquisition problem, and the raw ADC data will be set to -1 in this case. These channels are marked as the negative channels in the data analysis. Table 4.1 summarizes all the swapped channels spotted by the SSW scan during the commissioning and their status on 29/12/2021. According to the table, all swapped channels are fixed. 42 problematic channels in all are left to be fixed, and 23 out of the 42 channels are listed. The vast majority of these channels have the problem of setting the wrong ADC configuration. The naming rules of LTDBs can be found in Section 3.2.2.

Table 4.1 Problematic channels found by the connectivity scan. All swapped channels and part of problematic channels are listed. The third column gives the number of swapped and problematic channels that were found since the start of the commissioning. The last column gives the number of remaining swapped and problematic channels on 29/12/2021. All swapped channels are fixed, and 23 out of 42 problematic channels are listed here.

LTDB type	LTDB	# of Swapped/Problematic channels	# of unfixed channels
EMBA	I04L	2 / 1	0 / 1
EMBA	I10R	2 / 0	0 / 0
EMBA	I12R	2 / 0	0 / 0
EMBC	H05R	262 / 20	0 / 0
EMBC	H06R	278 / 12	0 / 0
EMBC	H07L	286 / 4	0 / 0
EMECA	A13R	6 / 0	0 / 0
EMECC	C03R	0 / 2	0 / 2
EMECC	C05R	0 / 1	0 / 1
EMECC	C07L	312 / 0	0 / 0
EMECC	C07R	0 / 20	0 / 13
EMECC	C08L	0 / 1	0 / 1
EMECC	C08R	16 / 0	0 / 0
EMECC	C13R	16 / 0	0 / 0
EMECA	A02S0	6 / 2	0 / 2
EMECA	A06S0	6 / 0	0 / 0
EMECA	A09S0	6 / 0	0 / 0
EMECA	A12S0	6 / 1	0 / 1
EMECC	C02S0	6 / 0	0 / 0
EMECC	C12S0	30 / 17	0 / 1
EMECA	A02S1	2 / 0	0 / 0
EMECA	A06S1	2 / 0	0 / 0
EMECA	A09S1	2 / 0	0 / 0
EMECA	A12S1	2 / 0	0 / 0
EMECC	C02S1	8 / 0	0 / 0
EMECC	C06S1	6 / 0	0 / 0
EMECC	C12S1	24 / 0	0 / 0
HECA	A02H	6 / 1	0 / 1
HECA	A06H	6 / 0	0 / 0
HECA	A09H	6 / 8	0 / 0
HECA	A12H	6 / 0	0 / 0
HECC	C02H	6 / 0	0 / 0
HECC	C12H	24 / 0	0 / 0
FCALA	A04F0	6 / 0	0 / 0
Total	34	1348 / 90	0 / 23

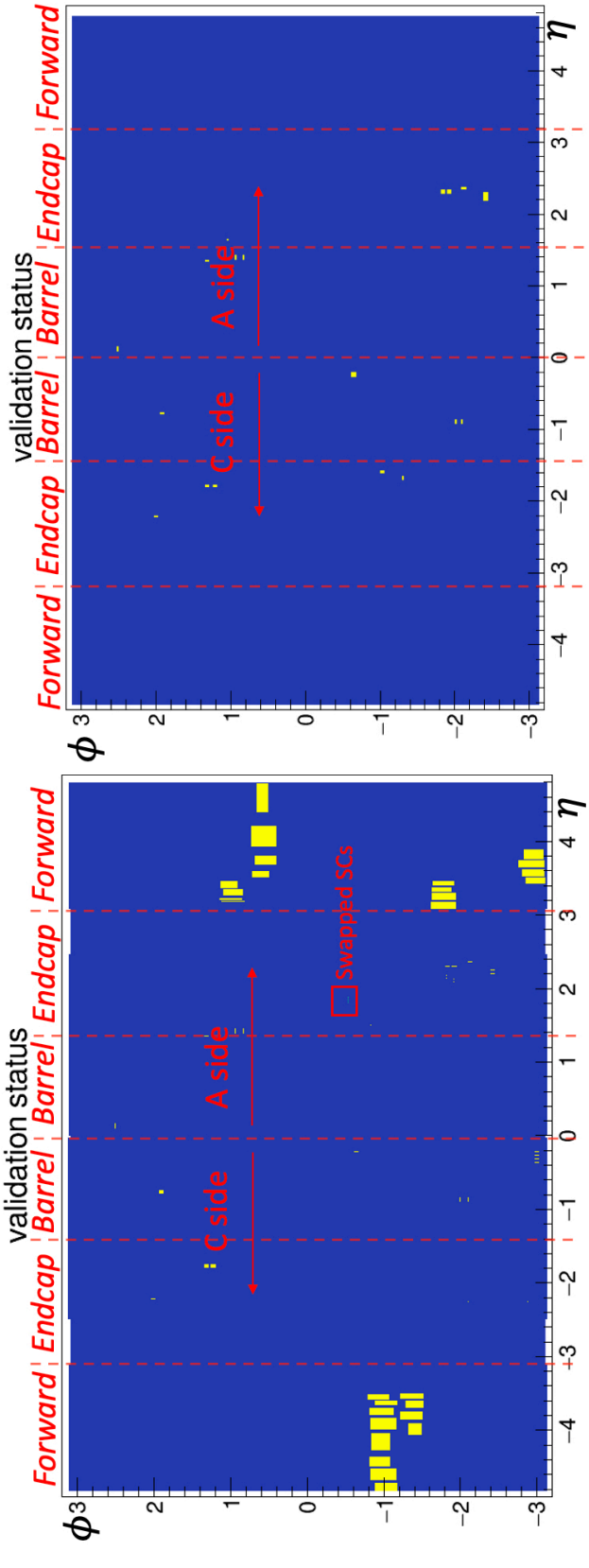

(a) Status on 16/09/2021.

(b) Status on 29/12/2021.

Fig. 4.11 LTDB validation status on 16/09/2021 and 29/12/2021. Supercells in the blue region are all validated. The yellow region represents the problematic supercells, and swapped supercells are shown in green. Swapped supercells in Figure 4.11a and problematic channels on FCal are fixed in Figure 4.11b.

4.2 BCID Calibration

The bipolar pulse signals are sampled with the frequency of 40 MHz, which is the same as the LHC BC frequency. Therefore the phase of the pulse is usually illustrated by the BCID, and the phase shift means the variation of BCID value. Such a feature requires that the sampling phase of the digital trigger readout should coincide with the sampling phase of the main readout. Otherwise, phase shifts greater than 25 ns can affect the computation of reconstructed E_{T} and τ. Figure 3.14 shows how the sampling points are chosen for the E_{T} computation. In order to have the proper coefficients used for the optimal filter algorithm, the calibration runs are taken to calibrate the values, which is discussed in Chapter 5. However, the pulse sampling timing must be stabilized before a calibration run can be performed. For this reason, the BCID calibration was performed immediately after the connectivity check was completed.

Practically, the BCID of the digital trigger readout is adjusted according to the BCID of the main readout. A change in BCID brings along a change in the latency of the system. The latency of the system, which is the time it takes for data to go from one point to another, is determined by how the system is designed. Run-3 does not change the circuit of the main readout from Run-2. Hence, the latency of the main readout has been fixed in Run-2 and will be used for Run-3. By this feature, the BCID of the digital trigger readout is calibrated with reference to the main readout.

4.2.1 Timing Alignment by Calibrating the Peak Position

The BCID in LATOME should be the same as the one in the main readout to align the timing between the digital pulse in the main readout and the digital trigger readout. As shown in Figure 3.14, the peak sampling of the signal matches the third point used for the E_{T} reconstruction. Therefore, the BCID of the peak sampling is a good reference point for the calibration. The shift of the pulse between the digital trigger and main readouts can then be calculated by the following expression.

$$\mathrm{Offset} = \mathrm{PeakBCID}_{LATOME} - \mathrm{BCID}_{main} - 2 \tag{4.1}$$

Here, the $\mathrm{PeakBCID}_{LATOME}$ is the BCID of the peak sampling point in the digital trigger readout (LATOME), for example, the third sampling point with a blue circle in Figure 3.14. The BCID_{main} is the BCID determined in the main readout, which corresponds to the timing of the signal injection, that is, the first sampling point with a blue circle in Figure 3.14.

Therefore, if the sampling phase is aligned between the digital trigger and the main readouts, the "Offset" should be 0. Practically, it is difficult to align all channels to 0 offsets because one fiber reads up to 8 channels so that the BCID can only be adjusted fiber by fiber. Hence the BCID calibration is done by taking the mean shift of the supercells on each fiber.

Figure 4.12 shows how the BCID calibration for each fiber is performed with an example supercell. The detailed procedure is given by the following clauses.

1. Take calibration pulse with the pulse-all run and check pulse shape with the digital trigger readout.

2. Get the peak position for each supercell. The peak BCID of the example pulse in Figure 4.12 is 46.

3. Calculate the offset for each supercell by Eq. 4.1, where the BCID of the main readout is stored in the calibration data. The offset of the example pulse in Figure 4.12 is 0 since the BCID of the main readout is 44. Average the offsets of the supercells for each fiber.

4. Updated the configuration values, which are for the system latency. The new value is the old one plus the averaged offset computed in step 3.

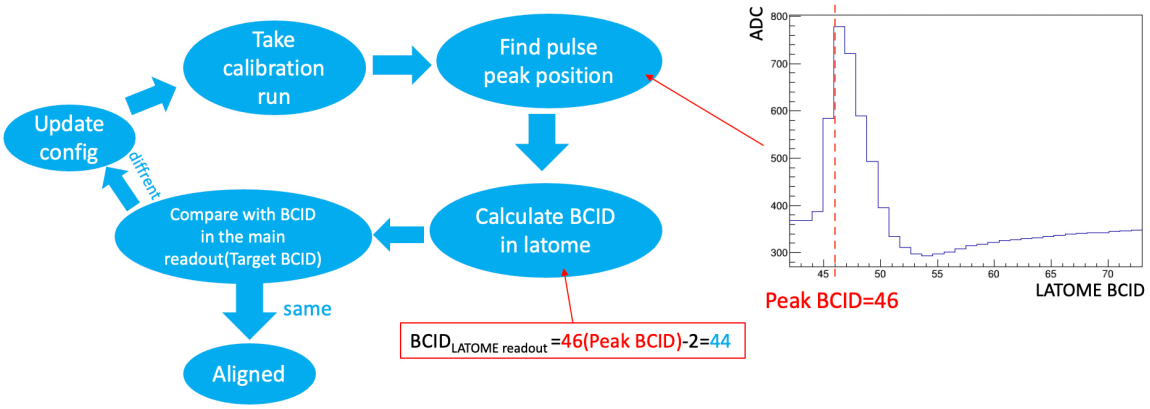

Fig. 4.12 Workflow of BCID calibration. The peak BCID in LATOME should be 2 less than the BCID in the main readout. A given example on the right side shows that the peak BCID of LATOME readout is 46. Therefore, BCID of the main readout should be 44.

Basically, this procedure determines all the BCID calibration values. However, sometimes the supercells are not pulsed for some reason, just the same as what we discussed in Section 4.1.4. In this case, the fiber is calibrated by referring to its neighbor fibers.

4.2.2 Instability of the Calibration Value

Besides the problematic channels, a part of good channels has issues in the BCID calibration mentioned above. The offsets of supercells in some fibers vary from time to time. This fluctuation is due to noise and the low sampling frequency.

As a matter of fact, the fluctuation of the peak position is observed on many fibers because two or more sampling points have similar ADC values around the peak position, as shown in Figure 4.13. These 8 supercells are on the same fiber, and the peak position of these supercells can be easily changed due to the noise. This kind of instability brings difficulty to the BCID calibration.

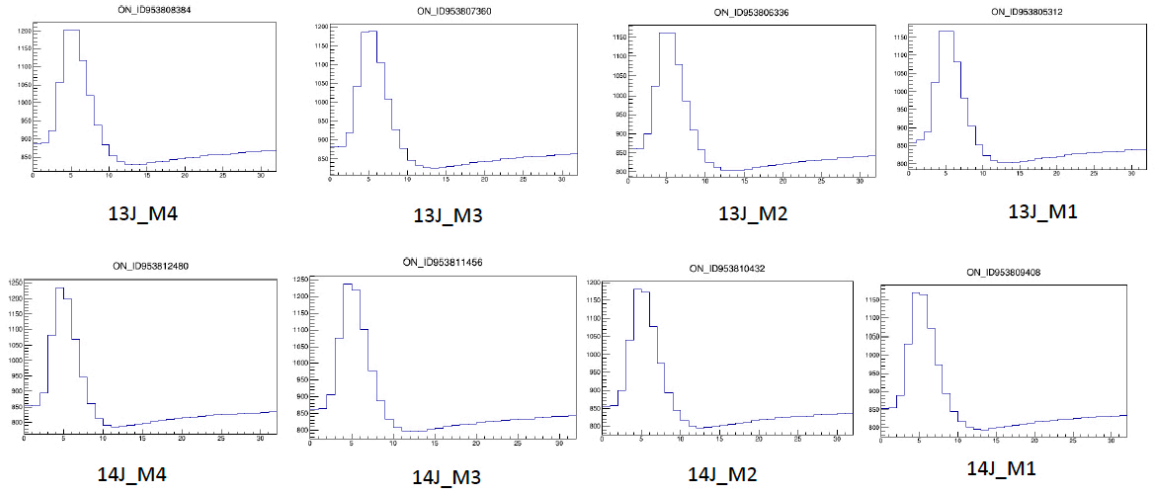

Fig. 4.13 Pulses with similar peak sampling points around the peak position. Letter "M" in the names of the supercells indicates that the supercells are from the middle layer.

Figure 4.14 shows the calibration result of two similar runs taken on the same day. As shown in Figure 4.14a, the offsets obtained from the two runs are filled with different colors. Fibers with bad links or the ADC configuration problems are not included. Regardless of a few outliers ($|\text{offset} > 2|$), most of fibers are already aligned ($\text{offset} = 0$), but several hundred fibers are still shifted by $\pm$ 1 BC ($\pm$25 ns). Figure 4.14b shows the difference of the offsets between the two runs, which is supposed to be 0. However, the calibrated BCID varies from run to run. In fact, 57 fibers have different BCID calibration values using the calibration method in Section 4.2.1. Therefore the optimization of the algorithm is needed to stabilize the calibration result.

Figure 4.15 shows how the RMS of the offset is distributed. Since there are non-zero RMS values, it indicates that supercells on the same fibers have different offsets. Over 100 fibers have an RMS of 0.5 and the mean offset of $\pm$0.5, which means the offsets of the supercells on those fibers are half 0 half $\pm$1, for example, offsets of supercells are like "0, 0,

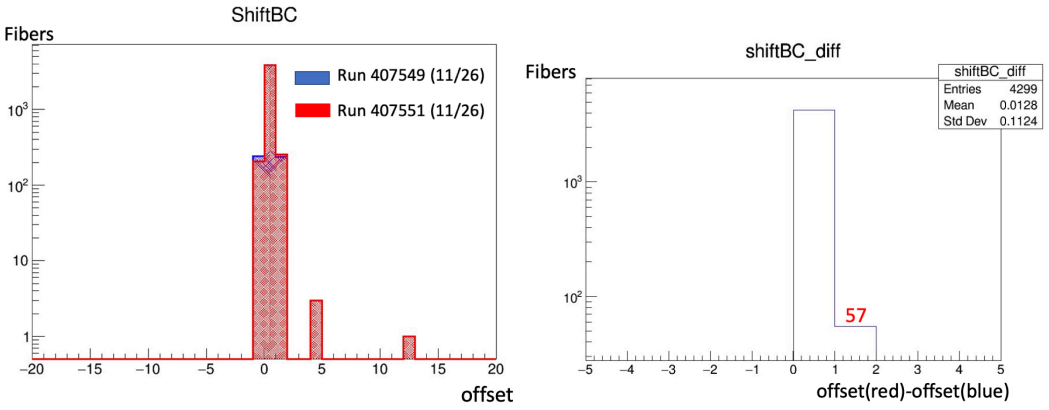

(a) Offsets from two runs. (b) Difference of the offsets between two runs.

Fig. 4.14 Comparison of two runs with the same BCID setting. The outliers in the left figure belong to one LATOME that possesses with deformed calibration pulse. The number of non-zero offset difference in the right figure is 57.

0, 0, 1, 1, 1, 1". As long as the peak position of some supercells varies due to the noise, the offset for that fiber also changes.

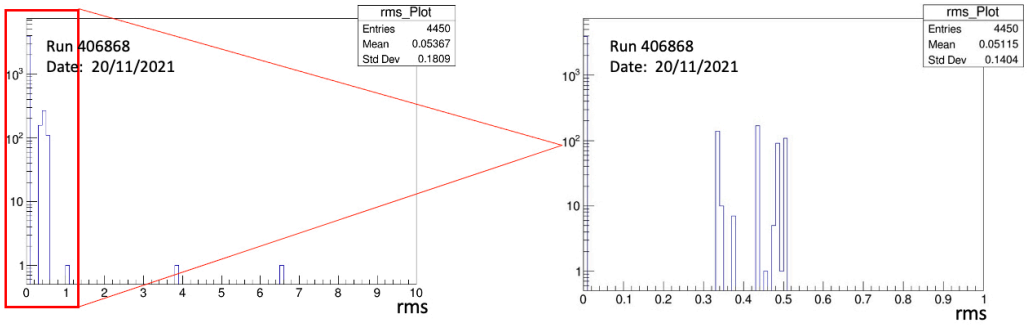

Fig. 4.15 RMS distribution of the supercells of the offsets of the supercells on the same fiber.

4.2.3 Optimization for Mitigating the Fluctuation

In order to make the result stable, the following optimizations are made.

1. For fibers with mean offset = ± 0.5 and RMS = 0.5, the signal delay is set to 0 instead of ± 25 ns. The former version takes the round of the mean offset so that the error of the operation is larger than 1 BC, which is not acceptable for the calibration.

2. Introduce the method of averaging samples in order to decrease the random error.

3. As shown in Figure 4.13. In case the difference between the peak sample and the one next to the peak is not large enough, the sample phase may change run by run due to the noise fluctuation. Therefore the former sample is chosen as the peak sample while the difference is less than height/10. Picking the former sample follows the instruction of minimizing the LATOME firmware latency.

Other optimization methods were attempted but not adopted. For example, the peak sample is given larger weights in many ways to enlarge the difference between peak and sub-peak. But no distinct improvement is observed with these methods.

The result of BCID calibration for the two runs after the above optimizations is shown in Figure 4.16. The two runs were taken on December 17th with the same latency configuration. As the application of the 3rd optimization, the number of the fibers shifted by -1 increases. However, the number of fibers with different calibration values is reduced from 57 to 1.

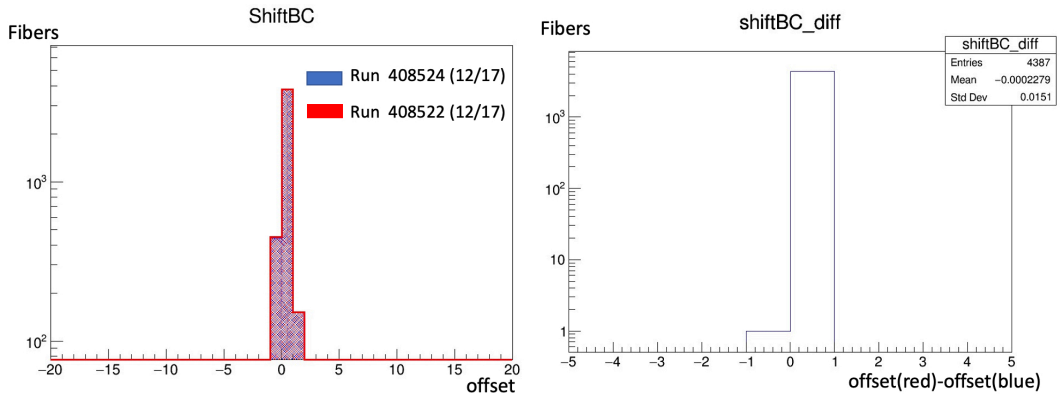

(a) Offsets from two runs. (b) Difference of the offsets between two runs.

Fig. 4.16 Comparison of two runs with the same latency after the optimization. These two runs are more stable, and the problematic LATOME with the outliers in Figure 4.14 is fixed. As a result, only one fiber is remained to have a different offset in the two runs.

After applying these optimizations, a new run with the stabilized calibrated BCID was taken on December 29th. The result is shown in Figure 4.17. 4457 out of 4458 fibers are involved in the figures except for one fiber on the LATOME named with EMECC_8, which has the link issue. The remaining fibers on the LATOMEs are grounded as the spared ones. The offsets are stabilized at 0, but several fibers have different BCID. This is because the ADC value difference of the peak and sub-peak sample is fluctuating around height/10, which is acceptable since the peak sampling point is stable within the difference of height/10.

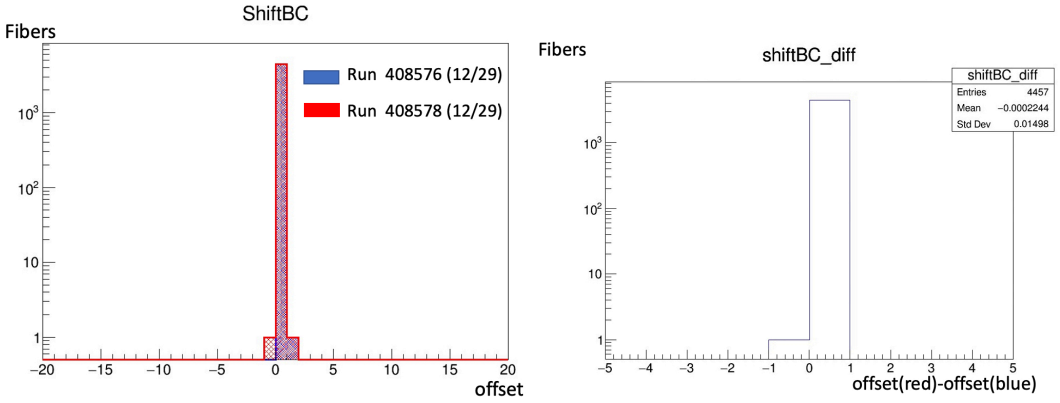

(a) Offsets from two runs. (b) Difference of the offsets between two runs.

Fig. 4.17 Comparison of two runs with the updated BCID. BCID for all fibers is now calibrated. One fiber has the different BCID calibration values in the runs.

Chapter 5

Calibration Run and Analysis for the LHC Pilot Run Data

5.1 Test Pulse System and OFC Calibration

5.1.1 Optimal Filtering Coefficient

While the connectivity check and BCID calibration are performed, the efforts on calibrating the optimal filtering coefficient (OFC) are also made in parallel. OFCs given by the Eq 3.1 and 3.2 can be written as the following expressions [27]:

$$\begin{aligned} a_i &= F_{\mathrm{DAC}\to\mathrm{MeV}} \cdot F_{\mathrm{ADC}\to\mathrm{DAC}} \sin\theta \times \tilde{a}_i, \\ b_i &= F_{\mathrm{BC}\to\mathrm{ns}} \cdot F_{\mathrm{DAC}\to\mathrm{MeV}} \cdot F_{\mathrm{ADC}\to\mathrm{DAC}} \sin\theta \times \tilde{b}_i, \end{aligned} \tag{5.1}$$

where $F_{\mathrm{DAC}\to\mathrm{MeV}} = F_{\mathrm{DAC}\to\mu\mathrm{A}} \cdot F_{\mu\mathrm{A}\to\mathrm{MeV}}$ is a conversion factor that converts DAC value to the energy, whose value is determined by the two terms on the right side. Here DAC is the discrete value set by the calibration board and is used for adjusting the input pulse height. $F_{\mathrm{DAC}\to\mu\mathrm{A}}$ is defined from the calibration board, and $F_{\mu\mathrm{A}\to\mathrm{MeV}}$ is a factor that converts the current send to the detector to the equivalent energy for the real EM shower. The conversion factors for each supercell are derived from the test beam system [31]. $F_{\mathrm{ADC}\to\mathrm{DAC}}$ represents a scaling factor of DAC to ADC and is calibrated by the test pulse system. $F_{\mathrm{BC}\to\mathrm{ns}}$ is given by the time interval of BC, which is 25 ns for the LHC BC. $\sin\theta$ is the conversion factor from energy to the transverse energy. $\tilde{a}_i$ and $\tilde{b}_i$ are the non-dimensional OFC used for the peak ADC estimation and calibrated by the test pulse system.

Notice that in the user code block of the LATOME firmware shown in Figure 3.12, the E_{T} candidate is stored in the buffer with 18 bits, where 1 bit is for the sign and 17 bits are for the value. Therefore to cover the range of $|E_T| < 1.6$ TeV, the least significant bit (LSB) is set to 12.5 MeV [32].

5.1.2 Calibration Run

There are two kinds of runs types for the LAr calorimeter. One is the physics run, which receives the signals of the EM shower from the collisions and then sends them to the FEC. Another is the calibration run, whose signals are from the calibration boards on the FEC. There is one calibration board on each HFEC.

The calibration board changes the signal amplitude, pulse timing, and target supercell as run parameters for different kinds of runs [31]. The amplitude of the signal is controlled by the 16 bit DAC values. It provides the voltage between 0 and 1 V by the step of 15.26 μV. The input current is therefore generated from the DAC voltage through a voltage to current converter, and the current is distributed to the readout channel on the detector motherboard. The conversion factor of the amplitude of the current is calculated by the following equation:

$$F_{\mathrm{DAC}\to\mu\mathrm{A}} = \frac{76.296\ \mu\mathrm{V}}{R_{\mathrm{inj}}},$$

where R_{inj} is the injection resistor with the range from 0.5 to 3 kΩ.

Each board is equipped with delay chips to set the delay for the pulse injection timing, which varies from 0 to 24.95 ns by steps of 1.04 ns and has 128 calibration lines to pulse between 8 and 32 channels depending on the layer per line [33].

By utilizing these features of the calibration board, three kinds of calibration runs are performed in the test pulse system: the pedestal run, ramp run, and delay run.

- **Pedestal run** Pedestal run is taken for obtaining the pedestal level of the supercells. During the pedestal run, no pulse signal is sent to the supercells. The pedestal, noise, and the autocorrelation of noise are obtained [27].

- **Delay run** Delay run changes the timing of the injection pulse. Each cell is pulsed N times (usually $N = 100$) with a certain DAC value at the delay between the calibration pulser and the data acquisition system. It divides 1 BC (25 ns) into 24 phases, which means the delay step is 1.04 ns. Hence, unlike the pulse sampled with 25 ns, the delayed pulses compose a smooth pulse shape to derive the non-dimensional OFC $\tilde{a}_i$

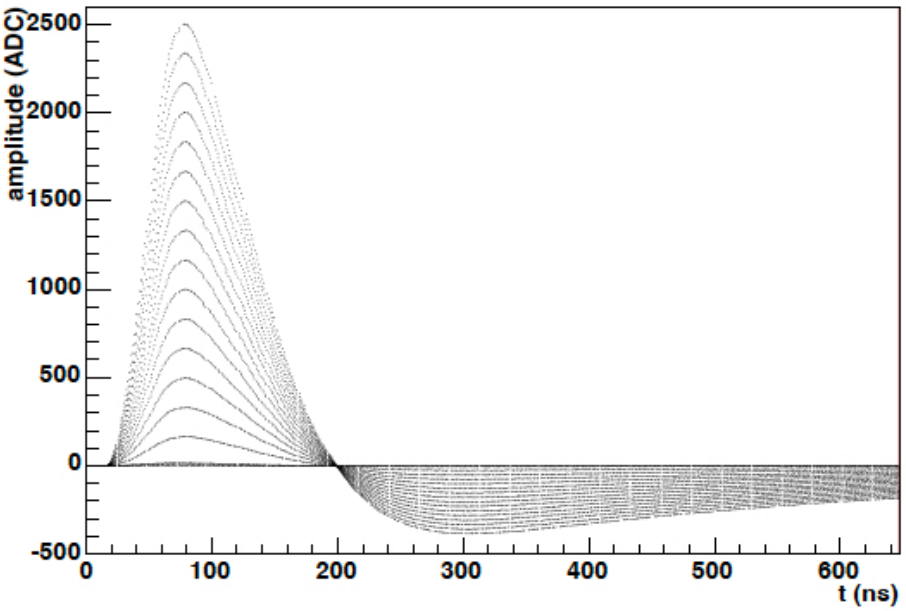

Fig. 5.1 Delay pulses with DAC values from 0 to 1500 for a supercell in the 2nd layer [31].

and $\tilde{b}_i$ with the pedestal run. Figure 5.1 shows the pulse shape after overlapping the pulse from the delay run.

- **Ramp run** Similar to the delay run, the ramp run is pulsed about 100 times with a set of given DAC values, and the delay set in the ramp run is fixed to 0. With the non-dimensional OFC $\tilde{a}_i$ and $\tilde{b}_i$ derived from the delay run, the peak ADC value is computed, and the curve of $\mathrm{ADC}_{\mathrm{peak}}$ to DAC is obtained. The values below the saturation level are used for the extraction of factor $F_{\mathrm{ADC}\to\mathrm{DAC}}$.

5.1.3 OFC calibration

In Section 5.1.2, $F_{\mathrm{ADC}\to\mathrm{DAC}}$ in Eq. 5.1 is obtained from the calibration runs, as well as the non-dimensional OFC $\tilde{a}_i$ and $\tilde{b}_i$. Thus, E_{T} can be calculated from Eq. 5.1 since $F_{\mathrm{DAC}\to\mathrm{MeV}}$ is already determined from the test beam. Figure 5.2 shows the distribution of E_{T} /ADC for different η and ϕ for supercells layer by layer, and each point represents one supercell. This E_{T} /ADC corresponds to the LSB for each supercell.

Figure 5.3 shows the distribution of non-dimensional OFC $\tilde{a}_1$, $\tilde{a}_2$, $\tilde{a}_3$, $\tilde{a}_4$ and $\tilde{b}_1$, $\tilde{b}_2$, $\tilde{b}_3$, $\tilde{b}_4$ for the main readout, that is, for LAr cells. Due to the 18 bits constraint, the absolute value of non-dimensional OFC are set to less than 70. The OFC of LAr cells is derived from the calibration run for the main readout. The dashed lines indicate the range of OFCs, and

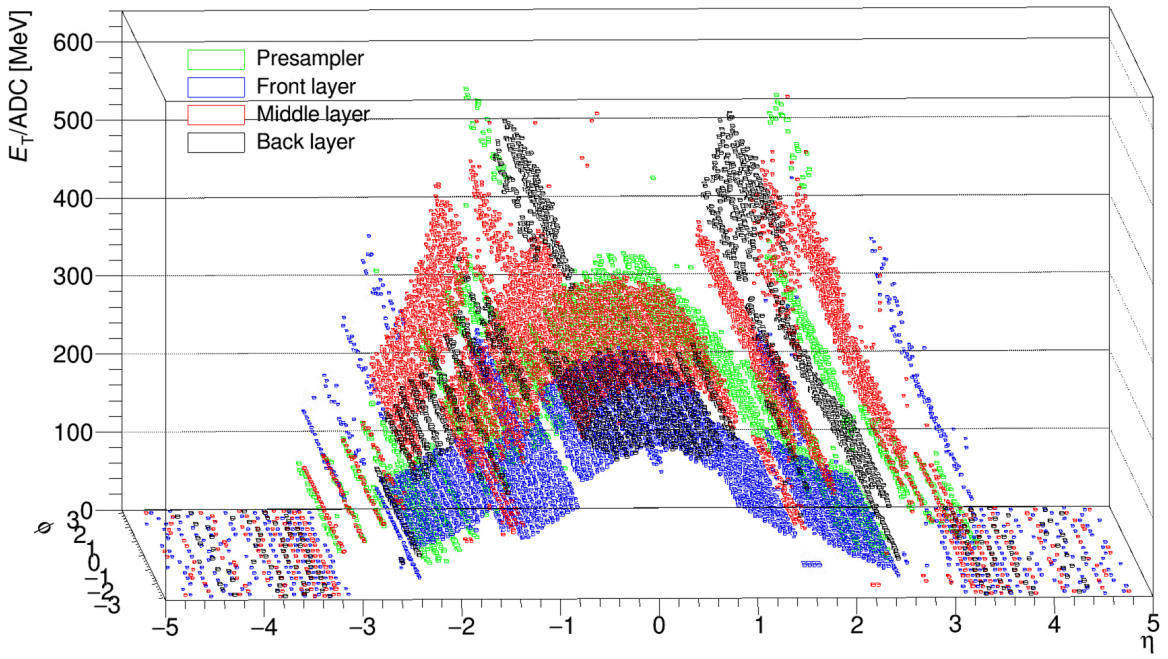

Fig. 5.2 E_T / ADC [MeV] distribution of supercells in all regions except for FCal. The values are uniformly distributed in the ϕ direction and vary in the η direction.

none of which exceed the limitation of 70. The non-dimensional OFCs for the supercells are calibrated in the same way.

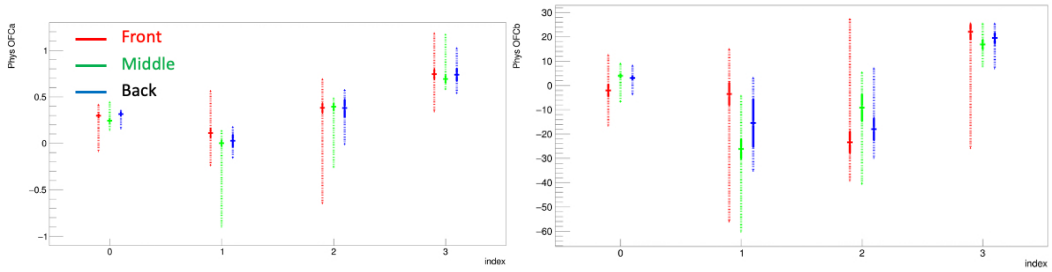

(a) OFC $\tilde{a}_i$ (b) OFC $\tilde{b}_i$

Fig. 5.3 Distribution of non-dimensional OFC $\tilde{a}_i$ and $\tilde{b}_i$ of LAr cells, where the vertical axis represents the index of i. Dashed line shows the range of the OFCs, and the solid line shows the mean value attached with the error bar [34].

5.2 Data Analysis with LHC Pilot Run Data

5.2.1 LHC Pilot Run

The first pilot beams towards Run-3 were circulated in the LHC in October 2021. During the pilot run, the ATLAS LAr calorimeter was fully powered. The LAr digital trigger readout participates in the data-taking. The corresponding energy reconstruction is also performed to provide triggers for splashes and collisions with the L1Calo.

Beam 1 that goes from A to C side is triggered on the C side, and beam 2 that goes from C to A side is triggered on the A side. The first interesting event from the beam splash is shown in Figure 5.4. The particle interactions in the EM and hadronic calorimeters and muon detectors are displayed. This event is recorded from beam 2 at 15:52 on October 19 th (CEST). ALTAS recorded additional splashes later that evening, and by the requests from the experiments, another two rounds of splashes were recorded. After the beam splashes were performed, collisions with stable beams ran for about 40 hours with the center-of-mass of 900 GeV.

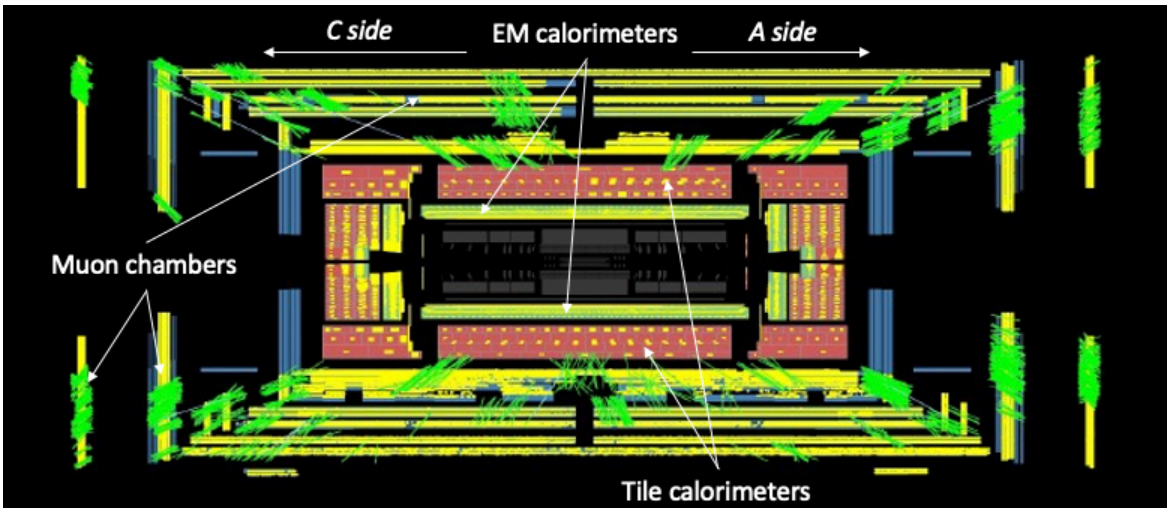

Fig. 5.4 Cut-away view of the first interesting event from the LHC beam splash test. This event is recorded at 15:52 on 19/10/2021 (CEST) from run 404473, beam2 [35].

Table 5.1 shows the information for the several runs taken in the pilot run and used for analysis. The latency between the digital trigger readout and the main readout is not well aligned since the calibration pulse latency is different from the physics pulse latency. The adjustment for this timing difference is not applied for both readout paths at the beginning of the pilot run. Therefore the last several runs of splash and collision events are used for the analysis. At the beginning of each collision run, the pixel detector needs to be calibrated

Table 5.1 Run information for the data used for analysis. Run 405604 is the last collision run.

Run number	Run type	Start time (CEST)	Stop time (CEST)	Hit / Active SCs
405396	Collision	28/10/2021 22:33	29/10/2021 06:34	15233 / 34019
405495	Splash	29/10/2021 18:30	29/10/2021 22:24	33970 / 34011
405604	Collision	31/10/2021 18:23	01/11/2021 06:02	11926 / 32771

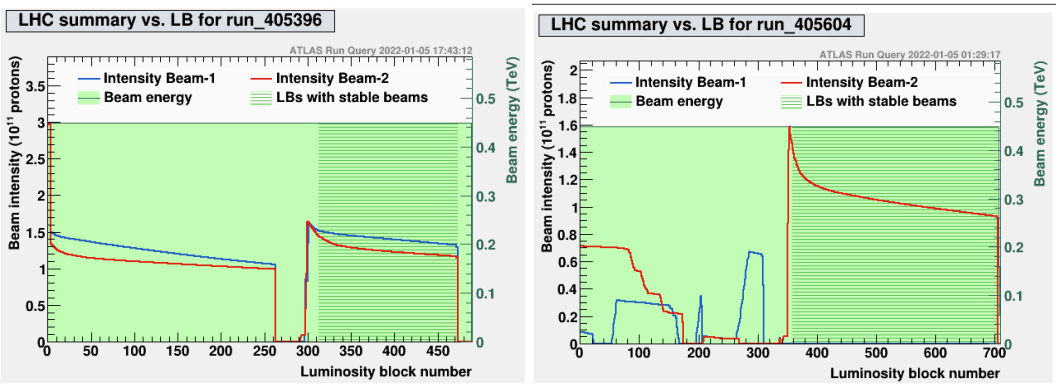

(a) Run 405396 (b) Run 405604

Fig. 5.5 Beam intensity summary for the collision run. Data in the LBs with stable beams (shaded area) are used for physics analysis. As shown in Figure 5.5b, the intensity of beam 1 in the shaded area is stabilized at 0 [36].

first, and due to the limitation of data transfer rate at high L1A, only about 10 samples of each channel are taken for the digital trigger readout using SWROD instead of the total 32 samples. After the calibration is done, the SWROD starts to take with the full data recording. In the last column of Table 5.1, the numbers of hit and active supercells are given. The active supercells are the ones without the link issue. Among all active supercells, hit supercells are the ones that receive pulse signals. The peak detection criterion in Section 4.1.2 with the height of 10 is applied to search the hit supercells. From the numbers of hit supercells, it can be known that there are more hit supercells in the run 405396. When the height threshold is raised from 10 to 20, the number of the hit supercells in the collision runs drops by a factor of 1/3. However, the ones in the splash run barely drop. Therefore, it can be expected that the collision data will include more noise than that in the splash data.

Figure 5.5 shows the status of beam1 and beam2 during the two collision runs. The beam energy is stabilized at 450 GeV. The luminosity block (LB) is a unit of the data taken with specified time intervals, typically about 1 minute, for several analysis purposes. Obviously, the intensity of beam1 dropped to nearly 0 during the stable beam flag was raised in the run 405604.

5.2.2 Peak Sample and BCID Delay

The position of the peak sample is investigated to check the BCID delay of the signals between the SWROD and the main readout, which can be computed by the Eq. 4.1. 1 BC offset corresponds to 25 ns BCID delay. The algorithm used for searching the valid pulse is also similar to the one applied in the SSW scan and BCID calibration (see Section 4.1.2) except that the part of the collision events is not recorded with the full 32 samples. Therefore, only the criterion of peak detection with the height threshold of 20 ADC is applied for the pilot run data.

In order to mitigate the impact of noise and check the active supercells, the pedestal level and RMS for each channel are computed with the luminosity blocks from 360 to 379 in the collision run 405604. RMS is calculated by the following equation,

$$\sigma_{\text{supercell}} = \sqrt{\frac{\sum_i (S_i - \mu_{\text{ped}})^2}{n_{\text{events}}}} \tag{5.2}$$

where the index i is summed over all the events, and $\sum_i = n_{\text{events}}$. S_i represents the ADC value, μ_{ped} is the mean pedestal ADC value for the supercell. Figure 5.6 shows the distribution of pedestals and RMS for all active supercells in the run. The number of active supercells is listed in Table 5.1. The uniformity of the statistics for the channels is observed in the figure. And the RMS for most channels are close to 0 except for the presampler. Especially, channels on EMB show good statistics and uniformed performance, which is attributed to the excellent calibration works.

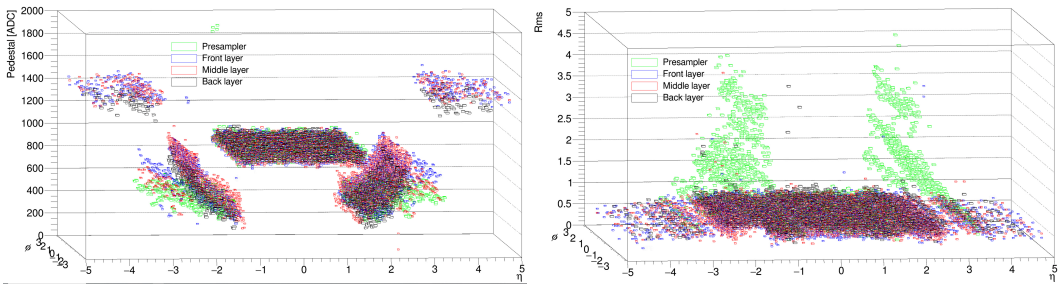

(a) Pedestal distribution (b) RMS distribution

Fig. 5.6 Pedestal and RMS value of all supercells are computed by the LBs from 360 to 379 in run 405604. Both statistics are evenly distributed in the ϕ range as expected.

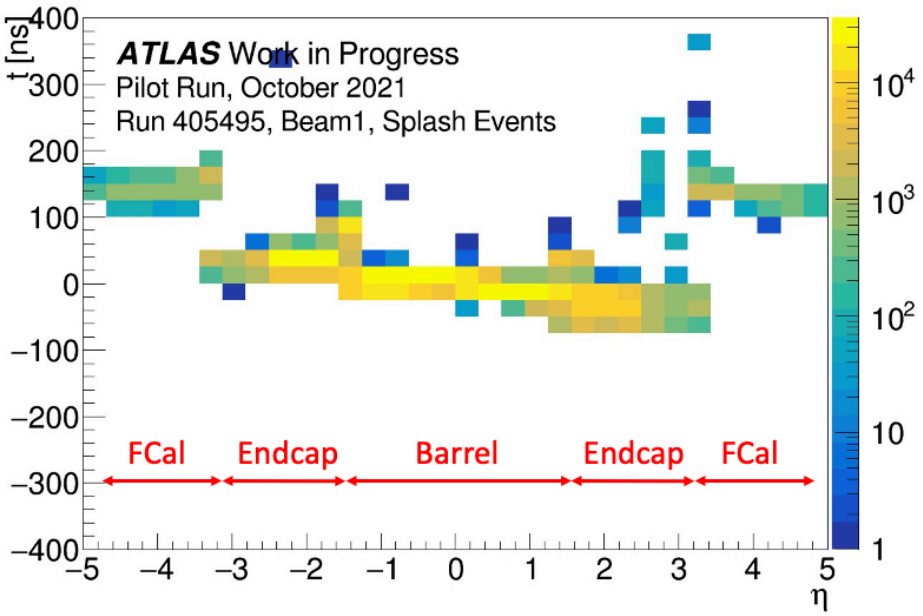

Fig. 5.7 BCID delay between SWROD and main readout with the splash data (run 405495). FCal is not calibrated yet at the time.

Splashes

The BCID calibration is not fully done during the pilot run, and only part of the EMB region is calibrated within the ± 1 BC for the splash run. Therefore the offset between the digital trigger readout and the main readout could be significant.

Figure 5.7 shows the BCID delay between the SWROD readout and the main readout from beam 1. The data sample is from run 405495, the beam splash events, whose information can be found at table 5.1. It can be seen that the offset from the FCal signal is quite large, which is consistent with what is observed in Figure 5.7. The BCID delay of most channels in EMB is adjusted based on the previous run. Therefore, most of them are around 0, which is also expected. Figure 5.8a shows the physics pulse from EMB in the run. Compared with the calibration pulse in Figure 4.6a, it can be seen that the undershoot of the calibration pulse and the physics pulse are different. The pulse from FCal is also shown in Figure 5.8b.

Collisions

Due to the limited time, the BCID in the digital trigger readout is not well-adjusted for the data-taking in collision events. In addition, the collision run is operated with low energy and low luminosity. Therefore, the barrel region rarely captures the signal events, and the same analysis for splash data is hard to perform on the collision data.

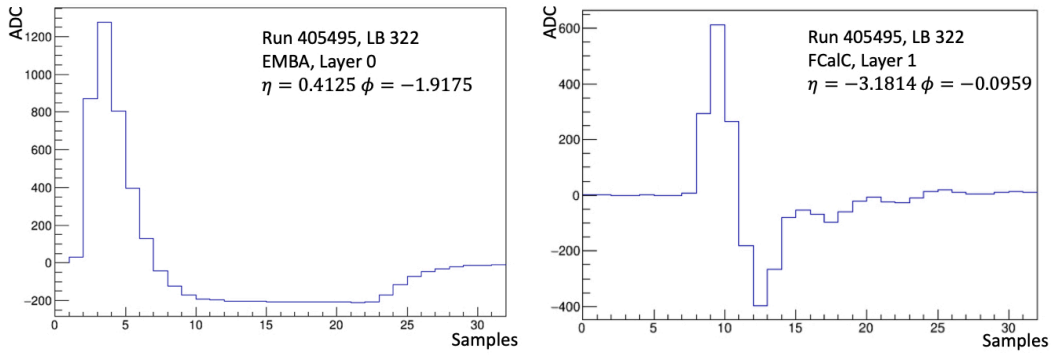

(a) EMB physics pulse (b) FCal physics pulse

Fig. 5.8 Physics pulse in the splash data. Both are read from LB 322 (run 405495), which belongs to the splashes from beam 1.

In the collision runs, over 200 LBs are recorded with 11 samples for each channel, and the rest of LBs are recorded with full 32 samples. Thus, the pulse detection method in Section 4.1.2 cannot be completely applied to the collision data. And due to the low beam energy, most events will be excluded with the tight cut. As a result, only the peak detection with a height of 20 is performed to mitigate the noise influence.

The result of BCID delay between SWROD and main readout is shown in Figure 5.9. Two collision runs are analyzed. Due to the low height cut, low luminosity, and low beam energy, the noise level is much higher than that in the splash events. Both runs indicate that most channels are not aligned yet, and their BCID delay is around -50 ns. The BCID calibration performed after the pilot run should fix this issue.

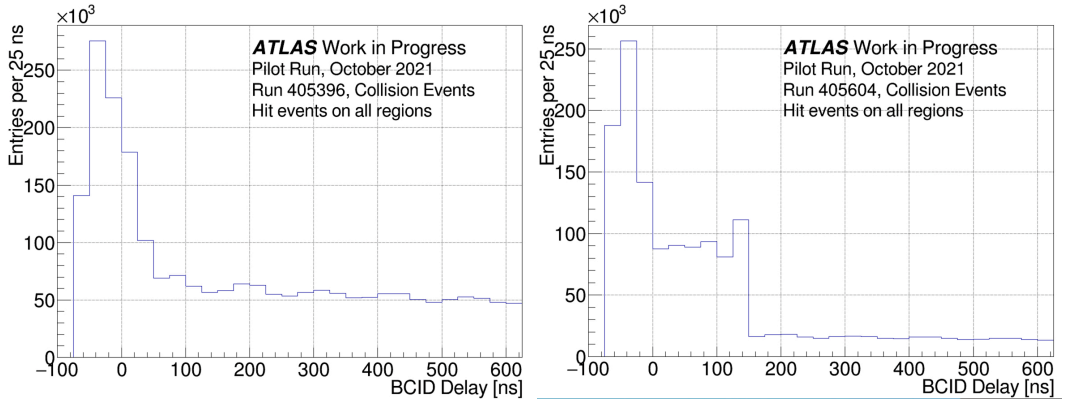

(a) Run 405396 (b) Run 405604

Fig. 5.9 BCID delay between SWROD and main readout with the collision data .

5.2.3 Energy and Timing Reconstruction.

It is essential to have the correct E_{T} computation in the digital trigger readout. Therefore the energy is also computed offline with the pilot run data. The OFC is already calibrated by the calibration run. However, the analysis results of BCID delay in Section 5.2.2 show that most channels are not aligned in the digital trigger readout, which means that the OFCs cannot be applied to a fixed BCID as it was in Figure 3.14. Therefore, the selection for the proper BCID should be performed to get the correct reconstructed E_{T} value. As shown in Figure 5.10, the selection is made by finding the BCID that matches the maximum reconstructed E_{T} with the minimum $|\tau|$. With this method, the energy is computed offline and selected by the τ criteria discussed in Section 3.2.4. The comparison of E_{T} between the selected events from the SWROD and the main readout is then made. Notice that only the comparison result of EMB and EMEC is given. As shown in Figure 5.7, the calibration for FCal is not done during the pilot run. In addition, the OFCs used for the E_{T} computation are calibrated with the calibration pulse.

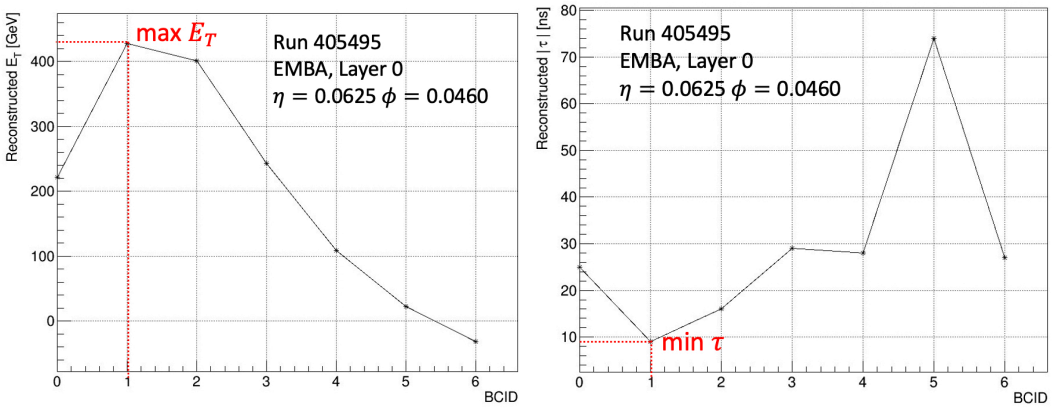

(a) E_T selection (b) τ selection

Fig. 5.10 Reconstructed E_{T} and τ at different BCID using the calibrated OFC. The supercell is from EMBA, and the injected pulse is from run 405495, the beam splash event. The BCID that matches the maximum E_{T} with the minimum $|\tau|$ is selected.

Splashes

The distribution of the computed E_{T} is shown in Figure 5.11. The data is from the SWROD readout, and the E_{T} is computed supercell by supercell. τ criteria are applied to exclude the noise. It can be seen that beam 1 was triggered on the C side, and beam 2 was triggered on the A side. Figure 5.11a and Figure 5.11b each includes 20 events.

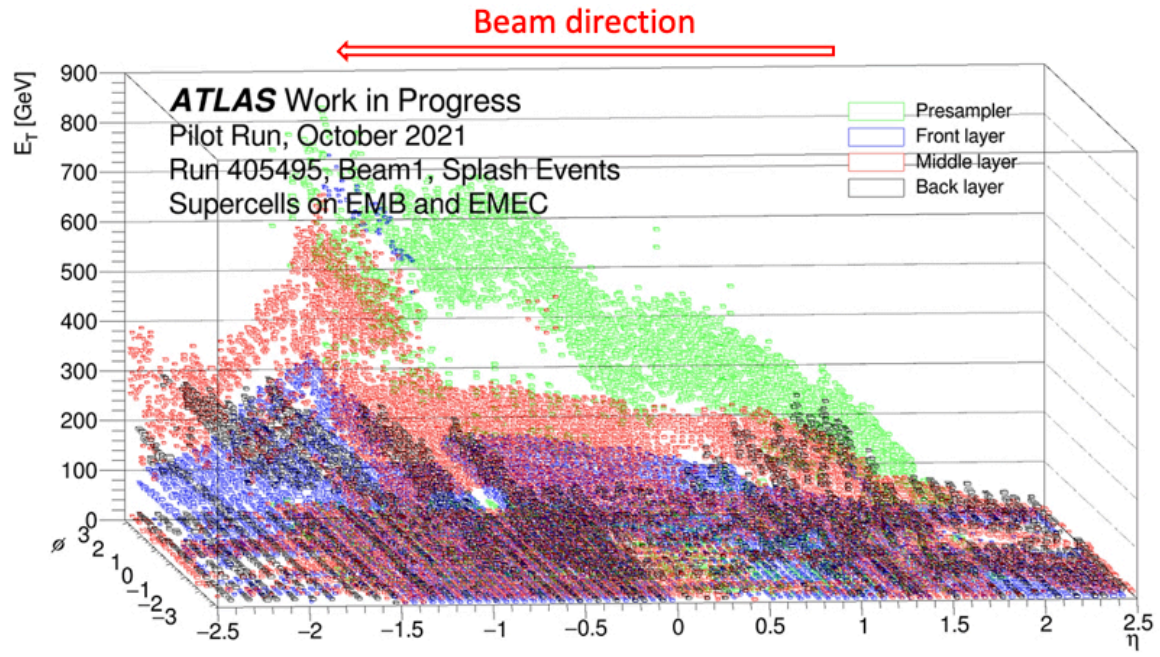

(a) beam 1

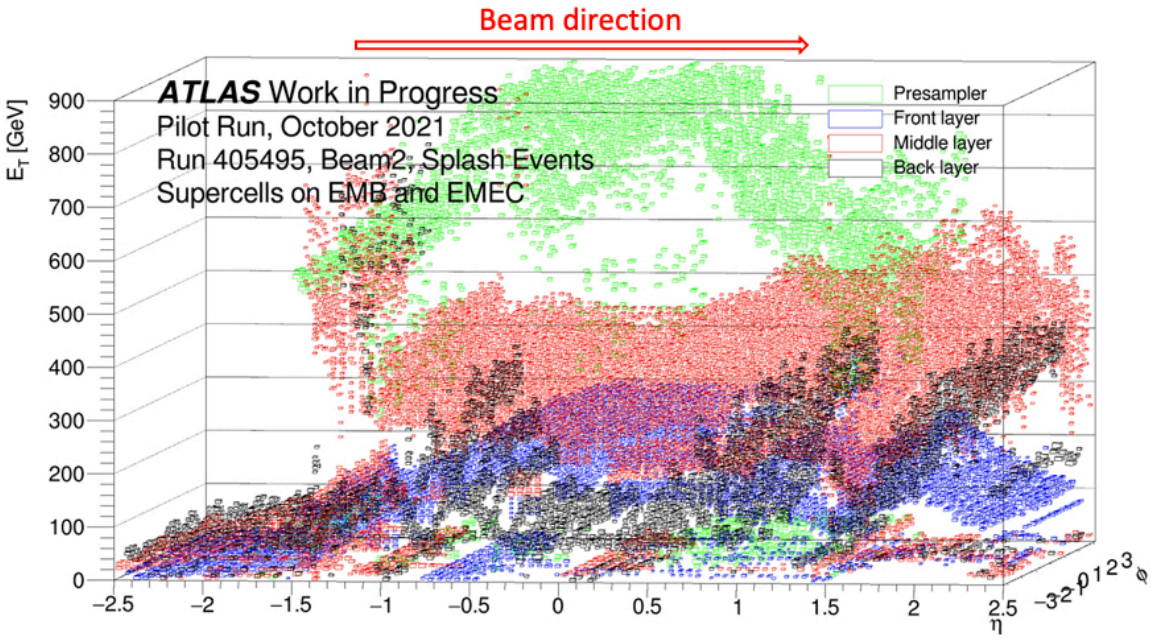

(b) beam 2

Fig. 5.11 Reconstructed energy distribution using splash data (run 405495). Beam direction is shown in the figures. Beam 1 is triggered on the C side, and beam 2 is triggered on the A side. Each figure includes 20 Events.

With the computed E_T from the SWROD, the energy comparison between SWROD and main readout using splash data is shown in Figure 5.12. Because the BCID calibration for the digital trigger system was not yet finished at the time, some SCs with larger BCID offsets also got deviations in the E_T computation. Despite that, both figures show the good consistency of computed E_T value between SWROD and main readout.

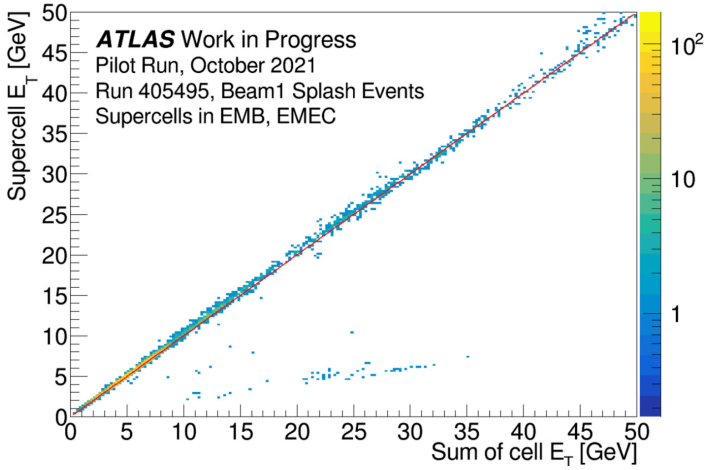

(a) beam 1

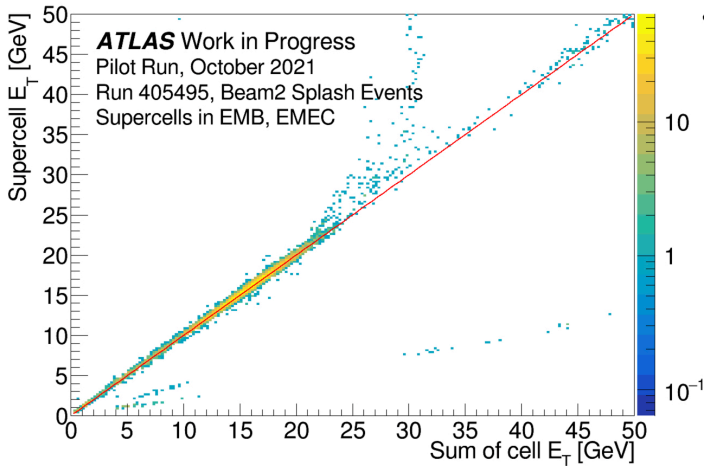

(b) beam 2

Fig. 5.12 Energy comparison between SWROD and main readout for run 405495. Figure 5.12a shows the data from beam 1. Figure 5.12b shows the data from beam 2. The red solid line is the $y = x$ line drawn as a reference.

Collisions

Run 405604 is used for energy computation. Also, since it was the last run, the LATOME output switched from E_T to E_T ID. E_T ID records the E_T computed in the user code for

supercells passing the τ criteria. The distribution of the reconstructed energy read by SWROD is shown in Figure 5.13. All LBs recorded by the SWROD are utilized, and the energy obtained is very low as expected. Moreover, it can be seen from the figure that E_{T} is evenly distributed in η and ϕ direction.

The comparison result is shown in Figure 5.14. Most events are at low energy and low occupancy. However, the E_{T} computed from the digital trigger readout is overall sightly larger than the E_{T} computed from the main readout. One possible reason is that the configuration used by the digital trigger system was adjusted according to the splash run. Therefore, although the computed E_{T} from splash run is consistent between digital trigger readout and main readout, the E_{T} calculation result of collision run may have some deviation.

To summarize, the collision data is not good enough to check the system's performance. However, by looking at the splash data, the good connectivity of the supercells can be confirmed, which means that the SSW scan in Section 4.1 does achieve the significant work. Moreover, by comparing the analysis results in the two readouts, it turns out that with the adjusted BCID obtained in Section 4.2 and the calibrated OFCs, the signal timing and energy computation can be finely tuned with the ones in the main readout. These conclusions give a promise that the digital trigger readout system can achieve the expected performance.

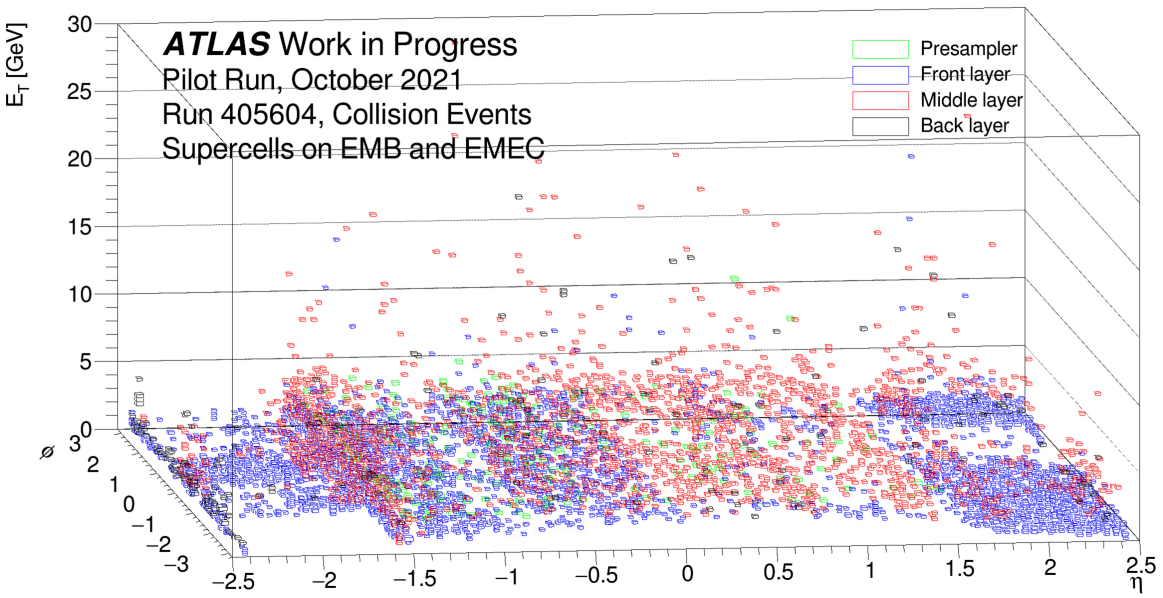

Fig. 5.13 Computed E_{T} using collision data (run 405604). The energy is much less than that in the splash events.

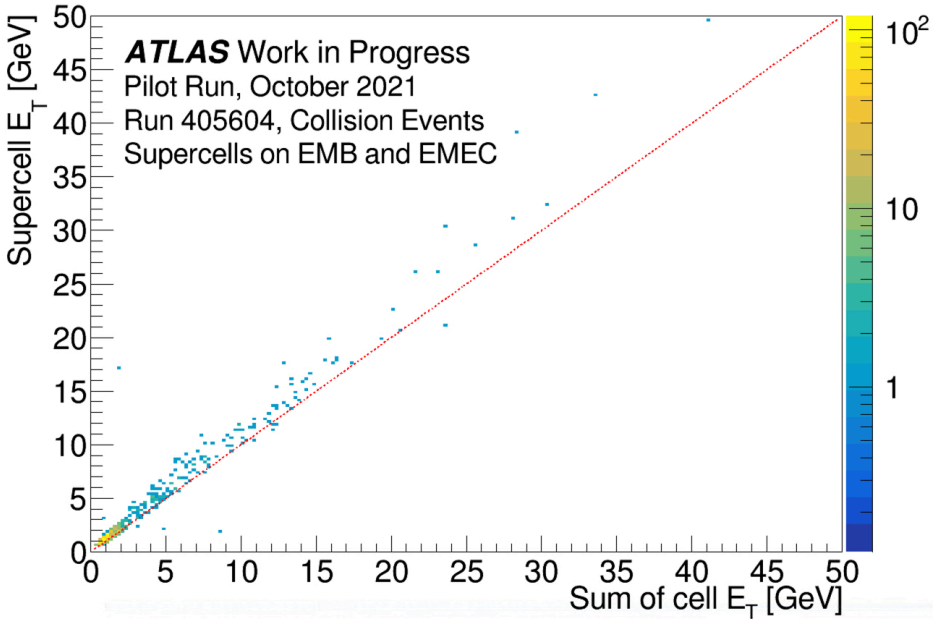

Fig. 5.14 E_{T} comparison between SWROD and main readout with collision data (run 405604). The red solid line is the $y = x$ line drawn as a reference.

Chapter 6

Conclusion and Outlook

6.1 Conclusion

The study checked the connectivity of the new digital trigger readout system of the LAr calorimeter during the LHC-ATLAS phase-I upgrade by using the SSW scan and adjusting the system latency to make the system have the stable sampling timing. This study also evaluated the digital trigger readout system with the data from the pilot run in October 2021.

In order to meet the requirement of ATLAS for the L1 trigger with the higher efficiency in Run-3, a new digital trigger readout system was developed for the LAr readout system that provides object recognition information for the trigger system. The new digital trigger readout system applies over 34000 supercells with 10 times higher granularity than the old readout cells and uses optical fibers to transmit the digitized data from the front-end to the back-end. The supercells with multi-layer structure cover the region of $|\eta| < 4.9$. The signals read out from the supercells are digitized by the LTDB at the front-end and transmitted to the back-end via optical fibers, where they are calculated by the LATOME board equipped with a high-speed FPGA for energy and timing reconstruction. The computation result is then sent to FEX for object recognition through optical fibers. The commissioning works done in the thesis are based on the validation of the new system.

Connectivity check is the first work to be done. This work is to check whether the supercells are connected correctly from the detector to the back-end. Without good connectivity, all the other commissioning works cannot be performed. In this thesis, the connectivity check of all 34048 supercells was done by the SSW scan, and a large number of swapped supercells were found and corrected. In addition to the connectivity problems, the SSW scan also checked pulse shape and pulse pattern to reveal problems such as bad link, bad ADC configuration, and bad calibration line. By the end of 2021, 99.9% of the supercells have been validated to be used for the L1Calo trigger system, and only 42 supercells are left to be

fixed. As a result, a few places turned out to be different from the design, but we were able to confirm that they did not affect the trigger performance.

Immediately after the connectivity test comes the fixed system latency, which represents the time it takes for data to travel from one point to another. For a stable system, its latency should be well-tuned and fixed. For the ALTAS experiment, the system latency can be changed by adjusting the BCID, and since the main readout system does not change in Run-3 compared to Run-2, it is used as a reference for adjusting the new digital trigger readout system. In this study, the pulse-all run is taken to check the BCID of over 4000 fibers on the LATOMEs. By developing the algorithm, the digital trigger system with a stable BCID is updated. With the stabilized and calibrated sampling phase, the calibration runs give the calibrated factors of $F_{\mathrm{ADC}\rightarrow\mathrm{MeV}}$ and non-dimensional OFCs for each supercell, which are used for the E_{T} and timing computation in the digital trigger readout.

In this research, not only the calibration data but also the LHC pilot run data are used. The data taken with the LHC pilot run in October 2021 are utilized for the full-powered new digital trigger readout test. In the pilot run, the detector achieves the purpose of taking both beam splash and collision data at the center-of-mass of 900 GeV. Thus, the timing investigation and energy computation are performed with offline analysis in the thesis. The offline analysis framework uses the raw ADC data read from the digital trigger readout and main readout to make the comparison of BCID and reconstructed E_{T} between them. Both results show that with the adjusted BCID and calibrated OFCs, the digital trigger readout can be adjusted to achieve the expected performance. This adjustment is actively proceeding towards the full operation of the digital trigger readout system in Run-3.

In summary, the connection check and BCID calibration for all supercells have been completed. Although individual supercells still need to be fine-tuned before Run-3, in general, the LAr phase-I upgrade has been successfully completed.

6.2 Outlook on Works towards Run-3

The debugging for the current problematic channels should be soon finished. On the other hand, although the BCID calibration is stable for most fibers, the fluctuation of ADC from several supercells may change the position of the peak sample. Thus, further checks for the stable sampling phase after the BCID calibration are required. At the same time, the analysis for the new OFC set computed with the latest sampling phase needs to be done. As for the pilot run data, analysis for all the runs is not finished yet. A good run list for the collision data is awaited to be summarized.

Besides all the plans above, the improvement on the LATOME firmware is also on the schedule. The current firmware applied on the LATOME in the pilot run and calibration run is not the version with full functionality activated. The optimization for the timing consumption of user code block may be accomplished by introducing the application of High-Level Synthesis (HLS).

During the first 6 months after the Run-3 operation started, the new digital trigger system will still be tested to be stable enough for the data acquisition, and the works mentioned above should be done before the complete handover of the legacy readout system to the digital trigger readout system.

References

[1] G. Aad et al. Observation of a new particle in the search for the standard model higgs boson with the atlas detector at the lhc. *Physics Letters B*, 716(1):1–29, 2012.

[2] Standard model of elementary particles, Sep 2019. Accessed 20 Dec 2021, https://en.wikipedia.org/wiki/File:Standard_Model_of_Elementary_Particles.svg#filelinks.

[3] Gordon L Kane. *The supersymmetric world: The beginnings of the theory*. World Scientific, 2000.

[4] P A Zyla et al. Review of Particle Physics. *Progress of Theoretical and Experimental Physics*, 2020(8), 08 2020. 083C01.

[5] Werner Herr and B Muratori. Concept of luminosity. 2006.

[6] Philippe Mouche. Overall view of the LHC. Vue d'ensemble du LHC. Jun 2014. General Photo.

[7] Luminosity determination in pp collisions at $\sqrt{s} = 13$ TeV using the ATLAS detector at the LHC. Technical report, CERN, Geneva, Jun 2019.

[8] G Aad et al. The ATLAS Experiment at the CERN Large Hadron Collider. *JINST*, 3:S08003. 437 p, 2008. Also published by CERN Geneva in 2010.

[9] Fabian Kuger. Signal formation processes in micromegas detectors and quality control for large size detector construction for the atlas new small wheel, 2017.

[10] Georges Aad et al. Alignment of the ATLAS Inner Detector in Run-2. *Eur. Phys. J. C*, 80:1194. 41 p, Jul 2020.

[11] A Vogel. ATLAS Transition Radiation Tracker (TRT): Straw Tube Gaseous Detectors at High Rates. Technical report, CERN, Geneva, Apr 2013.

[12] Morad Aaboud et al. Performance of the ATLAS Transition Radiation Tracker in Run 1 of the LHC: tracker properties. *JINST*, 12:P05002. 45 p, Feb 2017.

[13] *ATLAS liquid-argon calorimeter: Technical Design Report*. Technical design report. ATLAS. CERN, Geneva, 1996.

[14] ATLAS LAr Collaboration. The Phase-I Trigger Readout Electronics Upgrade of the ATLAS Liquid Argon Calorimeters. Technical report, CERN, Geneva, Nov 2020.

[15] *ATLAS muon spectrometer: Technical Design Report*. Technical design report. ATLAS. CERN, Geneva, 1997.

[16] ATLAS Outreach. ATLAS Fact Sheet : To raise awareness of the ATLAS detector and collaboration on the LHC. 2010.

[17] R. Schwienhorst. The Phase-1 upgrade of the ATLAS first level calorimeter trigger. *JINST*, 11(01):C01018, 2016.

[18] William Panduro Vazquez. The atlas data acquisition system: from run 1 to run 2. *Nuclear and Particle Physics Proceedings*, 273-275:939–944, 2016. 37th International Conference on High Energy Physics (ICHEP).

[19] Project schedule, 2021. Accessed 20 Nov 2021, https://project-hl-lhc-industry.web.cern.ch/content/project-schedule.

[20] G. Aad et al. Drift time measurement in the atlas liquid argon electromagnetic calorimeter using cosmic muons. *The European Physical Journal C*, 70(3):755–785, Oct 2010.

[21] Joao Pequenao. Event Cross Section in a computer generated image of the ATLAS detector. Mar 2008.

[22] M (CERN) Aleksa et al. ATLAS Liquid Argon Calorimeter Phase-I Upgrade: Technical Design Report. Technical report, Sep 2013.

[23] Georges Aad et al. Optical Fibers Cabling of the LAr Calorimeter Trigger Path for the ATLAS Phase One Upgrade. Technical report, CERN, Geneva, Nov 2017.

[24] L. Xiao et al. LOCx2, a low-latency, low-overhead, 2 $\times$ 5.12-gbps transmitter ASIC for the ATLAS liquid argon calorimeter trigger upgrade. *Journal of Instrumentation*, 11(02):C02013–C02013, feb 2016.

[25] X. Zhao et al. Mid-board miniature dual channel optical transmitter MTx and transceiver MTRx. *Journal of Instrumentation*, 11(03):C03054–C03054, mar 2016.

[26] Benjamin Taylor Carlson, Tae Min Hong, Chiao-ying Lin, Sophio Pataraia, and James Andrew Kendrick. Performance studies of the ATLAS L1Calorimeter trigger upgrade for run 3. Technical report, CERN, Geneva, Mar 2018.

[27] Gen Tateno. Calibration and performance evaluation of the liquid argon calorimeter trigger readout in the phase-i upgrade of the lhc-atlas experiment. Master's thesis, University of Tokyo, 2019.

[28] Overview of the Front-End interventions. Accessed 20 Nov 2021, https://cernbox.cern.ch/index.php/s/bp8vQ4KoSmhEsiD#office, Nov 2021.

[29] N J Buchanan et al. ATLAS liquid argon calorimeter front end electronics. *JINST*, 3:P09003, 2008.

[30] Renat Ishmukhametov and Julien Labbé. Crosstalk measurements in the electromagnetic calorimeter during atlas final installation. Technical report, Note ATL-COM-LARG-2008-012, CERN, Geneva, 2008.

[31] Martin Aleksa et al. ATLAS Combined Testbeam: Computation and Validation of the Electronic Calibration Constants for the Electromagnetic Calorimeter. Technical report, CERN, Geneva, Apr 2006.

[32] Reiyo Oishi. Firmware development and validation for the liquid argon calorimeter trigger readout system at the lhc-atlas run3 experiment. Master's thesis, University of Tokyo, 2019.

[33] WE Cleland. Cabling of the atlas liquid argon receiver system. Technical report, ATL-AL-EN-0042 https://edms. cern. ch/document/347182, 2003.

[34] OFC and calibration data for special crate, 06 2021. Accessed 05 Jan 2022 [CERN indico, protected] https://indico.cern.ch/event/1048772/contributions/4415104/attachments/2268807/3852679/LAr_week_tingyu_210622.pdf.

[35] Atlas prepares for run 3 as protons are back in the lhc, Dec 2021. [online] https://ep-news.web.cern.ch/content/atlas-prepares-run-3-protons-are-back-lhc.

[36] LHC beam energy and intensities during run 405604, Jan 2022. Accessed 05 Jan 2022, https://atlas-runquery.cern.ch/data/arq_220105/arq_220105002856qitr/popupContent_beampos_405604.html, https://atlas-runquery.cern.ch/data/arq_220105/arq_220105164250eiee/popupContent_beampos_405396.html.